8324889

Kim, Beom-Soo

OPTIMIZATION OF WAVERIDER CONFIGURATIONS GENERATED FROM NON-AXISYMMETRIC FLOWS PAST A NEARLY CIRCULAR CONE

The University of Oklahoma PH.D. 1983

University Microfilms International 300 N. Zeeb Road, Ann Arbor, MI 48106

PLEASE NOTE:

In all cases this material has been filmed in the best possible way from the available copy. Problems encountered with this document have been identified here with a check mark __√__.

1. Glossy photographs or pages _____
2. Colored illustrations, paper or print _____
3. Photographs with dark background _____
4. Illustrations are poor copy _____
5. Pages with black marks, not original copy _____
6. Print shows through as there is text on both sides of page _____
7. Indistinct, broken or small print on several pages __√__
8. Print exceeds margin requirements _____
9. Tightly bound copy with print lost in spine _____
10. Computer printout pages with indistinct print _____
11. Page(s) __________ lacking when material received, and not available from school or author.
12. Page(s) __________ seem to be missing in numbering only as text follows.
13. Two pages numbered __________. Text follows.
14. Curling and wrinkled pages _____
15. Other ____

THE UNIVERSITY OF OKLAHOMA

GRADUATE COLLEGE

OPTIMIZATION OF WAVERIDER CONFIGURATIONS GENERATED FROM NON-AXISYMMETRIC FLOWS PAST A NEARLY CIRCULAR CONE

A DISSERTATION

SUBMITTED TO THE GRADUATE FACULTY

in partial fulfillment of the requirements for the

degree of

DOCTOR OF PHILOSOPHY

By

BEOM-SOO KIM

Norman, Oklahoma

1983

OPTIMIZATION OF WAVERIDER CONFIGURATIONS

GENERATED FROM NON-AXISYMMETRIC FLOWS

PAST A NEARLY CIRCULAR CONE

A DISSERTATION

APPROVED FOR THE SCHOOL OF AEROSPACE, MECHANICAL

AND NUCLEAR ENGINEERING

By

M. Rasmussen

G Emanuel

Martin C Jischke

ACKNOWLEDGEMENT

I would like to express my deep appreciation and gratitude to my advisors, Dr. Maurice L. Rasmussen and Dr. Martin C. Jischke who gave me guidance and consistent encouragement through all my graduate work.

I also appreciate Dr. George Emanuel, Dr. John E. Francis and Dr. Stanley B. Eliason for their good teaching and for reading this text.

My appreciation also goes to Dr. Donald C. Daniel who supported this project through Contract F08635-80-K-0340.

Thanks to all my colleagues who discussed many topics with me and spent meaningful time together at the University of Oklahoma.

To my wife and parents, I express my love for their concern and support during my study.

ABSTRACT

The optimum configurations of cone-derived waveriders having maximum lift-to-drag ratios subject to a suitable constraint, such as fixed lift, are investigated. Analytic results from inviscid hypersonic small-distrubance theory for non-axisymmetric conical flow past a nearly circular cone are used, and results are valid for all values of $K_\delta = M_\infty \delta$, where δ is the semivertex angle of the basic circular cone. The special case of the configurations generated from axisymmetric conical flow is compared extensively with other configurations to give insight on the effects of the pertinent parameters. The inviscid analysis accounts for wave drag only, but the effect of viscous drag is discussed. The results are analytic in nature and particularly suitable for studying the various trade-offs that are involved in missile design. Comparison of the results with other types of lifting-bodies suggest that properly selected waveriders are among the best producers of large lift-to-drag ratios.

TABLE OF CONTENTS

TABLE OF CONTENTS (cont)

LIST OF FIGURES

LIST OF FIGURES (cont)

LIST OF FIGURES (cont)

Figure | Page

LIST OF SYMBOLS

$A(R)$, $B(R)$, $C(R)$	Coefficient functions of quadratic equation or cubic equation
a, b, c	Expressions in Eq. (6.14)
A_b	Base area of waverider
C_p	Pressure coefficient
C_f	Friction coefficient
D	Drag
D_f	Viscous drag
D_w	Wave drag
$\hat{e}_r$, $\hat{e}_\theta$, $\hat{e}_\phi$	Unit vectors in spherical polar coordinates
$\hat{e}_x$, $\hat{e}_y$, $\hat{e}_z$	Unit vectors in Cartesian coordinates
E_n	Dimensionless parameter ($= \varepsilon_n/\delta$)
f_n	Function in Eq. (2.19)
F_n	Dimensionless form of f_n
F_ℓ, $F_{\ell 1}$, $F_{\ell 2}$,	Integral associated with lift
F_d, F_{d1}, F_{d2},	Integral associated with drag
F_g	Integral associated with constraint
G	Constraint functional
g_n	Ratio between perturbations of shock and body
H	Optimizing functional with constraint

I_ℓ	Integral associated with lift
I_d	Integral associated with drag
I_g	Integral associated with constraint
K_δ	Hypersonic similarity parameter ($= M_\infty \delta$)
L	Lift
ℓ	Length of basic cone
M_∞	Freestream Mach number
$\hat{n}$	Normal unit vector
p	Pressure
P	Dimensionless pressure
q	Dynamic pressure ($= \rho_\infty V_\infty^2/2$)
$R(\phi)$	Trailing edge function
r, θ, ϕ	Spherical polar coordinates
S_b	Shock layer base area
S_c	Compression stream surface
S_p	Projected planform area of waverider
S_{fs}	Freestream surface
S_s	Shock surface
S_w	Wetted area of waverider
T	Temperature
$\vec{V}$	Velocity vector
V_∞	Freestream velocity

u, v, w	Components of velocity in spherical polar coordinates
U, V, W,	Dimensionless velocity components
V	Volume of waverider
x, y, z	Cartesian coordinate system
β	Basic shock semivertex angle
γ	Ratio of specific heat
δ	Basic cone semivertex angle
$\tilde{\delta}$	Variational operator
ε_n	Small perturbation parameter
ϕ	Azimuthal angle, measured from x-z plane
ϕ_ℓ	Dihedral angle of waverider, $R(\phi_\ell) = \sigma$
$\phi_{\ell c}$	Critical dihedral angle
$\phi_{\ell o}$	Optimum dihedral angle
ϕ_δ	Azimuthal angle at body satisfying $R(\phi_\delta) = 1$
λ	Lagrange multiplier
$\bar{\lambda}$	λ/δ
ρ	Density
ξ	θ/δ
σ	β/δ
ψ	Function in Eq. (4.31b)
$\Phi(\xi)$	Trailing-edge function
θ	Polar angle, measured from z axis

LIST OF SYMBOLS (cont)

Subscript

o	zeroth-order solutions
n	first-order solution of case n
s	at shock
δ	at body

Superscript

*	idealized cone case
-	dimensionless form

SECTION I

INTRODUCTION

Recent progress in technology has made flight at hypersonic speeds possible. As a consequence, the identification of high-lift configurations with low drag and good control effectiveness in this speed range has attracted considerable attention. Lifting bodies having non-circular cross-section are of current interest as a means for obtaining high-performance missile characteristics.

The use of digital computers greatly facilitates the calculation of general three dimensional hypersonic flows, but the complexity and expense of these calculations do not lend themselves to parametric studies or the basic understanding desirable for missile design considerations. Thus, special configurations from which the flow fields are simple and well known become particularly suitable for delineating various trade-offs that are involved in missile design.

Waverider configurations are derived from the general principle that any streamline of an inviscid flow can be viewed as part of a solid boundary of the flow. A general discussion of waverider configurations of this kind is given by Küchemann [1]. The variety of exact waverider configurations available now is, therefore, limited by the number of exact flow field solutions from which the streamlines can be determined.

The simplest flow field of them all is a flow past a two-dimensional wedge and has been used by Nonweiler [2] to describe the flow past caret-shaped waveriders and many experimental investigations of the caret waverider are now available [3].

The next simple exact flow field solution is the flow past a circular cone with zero angle of attack. This conical flow field is well known and documented [4]. Jones [5] has used the circular-cone solution to describe the flow past a near-delta planform wing with an underbody which is a portion of a circular cone. Maikapar [6] has used the circular cone solution to produce a star shaped waverider by using the intersection of circular shocks, and more general waveriders has been generated by Baron [7] using Maikapar's method.

The exact solutions of more complex flow fields, such as a flow field past an inclined cone [8], an elliptic cone [9], and a conical body with nearly circular cross-section [10] have been developed recently and have been used to generate waveriders [11].

While such results are very useful, there are infinite number of possibilities for such waverider configurations. The problem of missile design is concerned with possible optimized configurations. Most previous works dealing with optimization of configurations in hypersonic flow have assumed the surface pressure to be given by Newtonian theory. Pertinent examples are those of Lusty and Miele [12] and Huang [13]. They have found that optimum shape for high lift-to-drag ratio is a conical body which has diamond shaped cross-section. At best, these works are applicable strictly to the limit when $K_\delta = M_\infty \delta$ tends to infinity, where δ is a pertinent flow-direction angle.

Further, the flow field structure and shock shape are not accounted for as part of the analysis.

Hypersonic small disturbance theory [14] has been used by Cole and Zien [15] to produce optimum waverider configurations from the flow field past a power-law body. However, the work was done by using digital computer and the results were good when $K_\delta = \infty$ only. Hypersonic small disturbance theory results were also used by Kim et al. [16] to produce optimum waverider configurations from the flow field past a circular cone with zero incidence. The work was analytic and the results were valid for all K_δ values.

So far none of waverider configurations has been optimized from a non-axisymmetric flow field analytically. This paper is a generalization of the work of Kim et al. [16] and discusses optimization of waverider configurations derived from nearly axisymmetric conical flow fields. The specific problem is to maximize the lift-to-drag ratio of waveriders when lift is fixed, however, such factors as cone angle, Mach number, body volume, base area and planform area of waveriders also can be used as constraints with the analysis.

The analysis is akin to that of Cole and Zien [15]. It lies within the framework of hypersonic small disturbance theory, and the results are valid for arbitrary values of the similarity parameter K_δ. The results for the special case in which the waverider configurations generated from the circular cone flow have been compared extensively with the idealized waverider and other results to give insight of the effect of the concerned parameters.

SECTION II

FORMULATION

2.1 General Results

Consider a waverider configuration in a Cartesian coordinate system x, y and z as shown in Fig. 2.1, with the free stream velocity $\vec{V}_\infty$ pointing in the z direction. We assume that the waverider configuration is comprised of three surfaces:

1) A compression stream surface, which is the bottom surface of the waverider and the surface, is generated by a sheet of streamlines which originate from a known flow field. The shock wave due to the compression stream surface is, therefore, the portion of the original shock wave of the known flow field. The intersection between the original shock surface and the compression stream surface becomes the leading edge of the compression stream surface.

2) A free stream surface is the upper surface of the waverider. The surface is parallel to the free stream velocity $\vec{V}_\infty$ and intersects the compression stream surface on the shock surface. The intersection line becomes the leading edge of both the free stream surface and the compression stream surface.

3) A base plane surface, which is perpendicular to the free

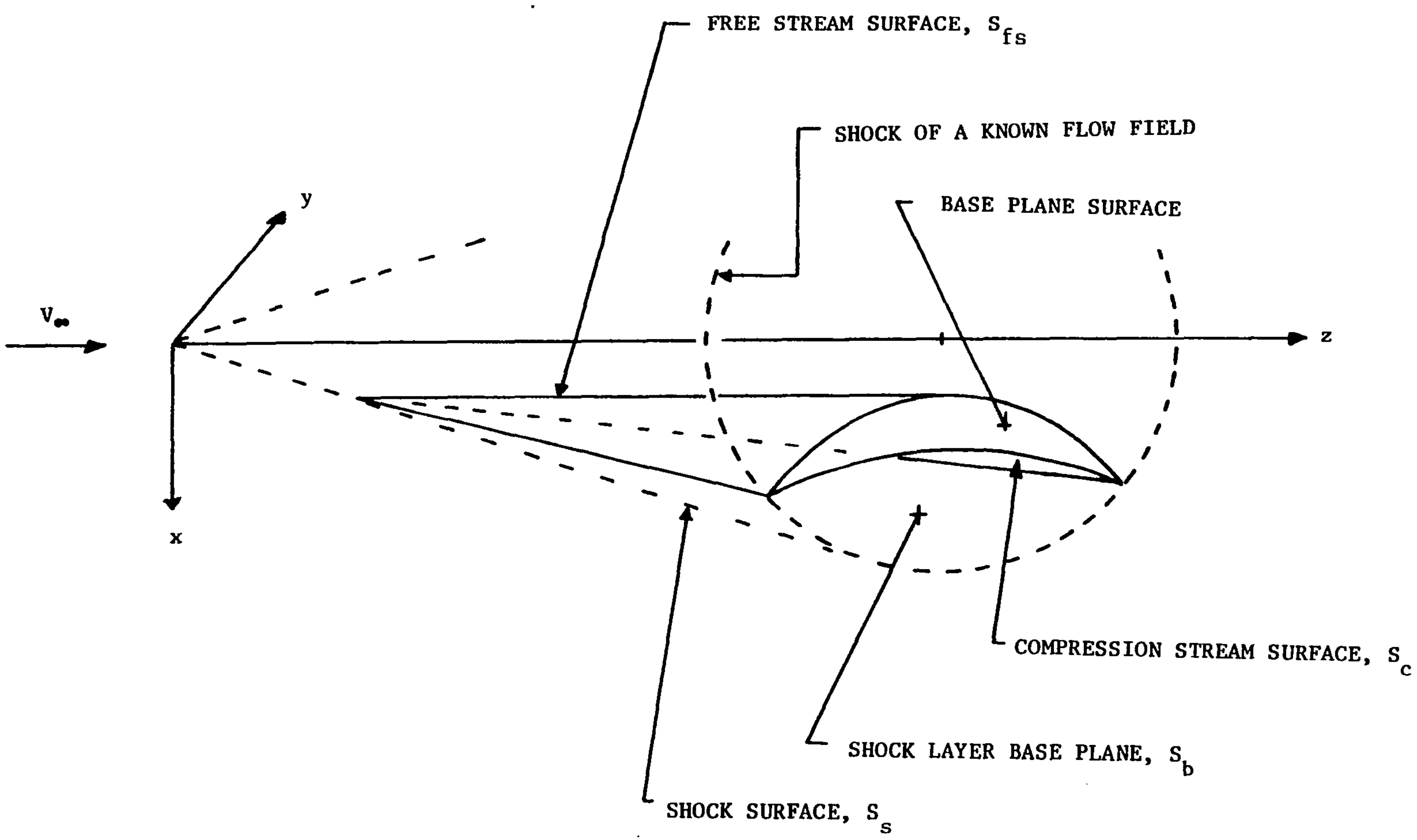

Fig. 2.1 A Waverider Configuration in Cartesian Coordinate System.

stream at $z = \ell$, is the rear surface of the waverider. The base plane surface pressure is assumed equal to the free stream pressure which is tantamount to omitting the base drag in the ensuing analysis.

In the region bounded by the shock surface and the compression stream surface, the original known flow field will remain unchanged. Therefore, the forces acting on a waverider in steady supersonic flow can be determined by means of the integral equations of inviscid gas-dynamics and the known flow field solutions. Let the shock layer region of the waverider be enclosed by a combination of three surfaces:

1) A surface S_s embracing the upstream side of the shock surface,
2) the compression stream surface of the waverider, S_c and,
3) a shock layer base plane, S_b, perpendicular to the free stream at $z = \ell$ and which intersects the shock surface S_s and the compression stream surface S_c.

Then the application of the laws of conservation of mass and momentum to the fluid inside this control volume surrounded by the three surfaces gives the following equations.

$$\iint_S \rho\vec{V} \cdot \hat{n}\, ds = 0 \quad , \tag{2.1}$$

$$\iint_S (\rho\vec{V}\vec{V}\cdot\hat{n} + p\hat{n})ds = 0 \quad , \tag{2.2}$$

where $S = S_s + S_c + S_b$, $\vec{V}$ is the fluid velocity, p the pressure, ρ the density, and $\hat{n}$ the normal unit vector directed outward. Since we have

$$\iint_S p_\infty\, \hat{n}\, ds = 0 \quad ,$$

we can also write the momentum equation, Eq. (2.2), as

$$\iint_S \{\rho\vec{V}\vec{V}\cdot\hat{n} + (p-p_\infty)\hat{n}\}\, ds = 0 \quad . \tag{2.3}$$

By noting that

$$\text{on } S_b \;;\quad \hat{n} = \hat{e}_z$$

$$\text{on } S_c \;;\quad \vec{V}\cdot\hat{n} = 0,\ \hat{n} = \hat{n}_c$$

$$\text{on } S_s \;;\quad \vec{V} = \vec{V}_\infty\ ,\quad p = p_\infty,\ \rho = \rho_\infty,\ \hat{n} = \hat{n}_s$$

we can write the Eqs. (2.1) and (2.3) as

$$\iint_{S_s} \rho_\infty\vec{V}_\infty\cdot\hat{n}_s ds + \iint_{S_b} \rho\vec{V}\cdot\hat{e}_z ds = 0 \quad , \tag{2.4}$$

$$\iint_{S_c}(p-p_\infty)\hat{n}_c ds + \iint_{S_b}\{\rho\vec{V}\vec{V}\cdot\hat{e}_z + (p-p_\infty)\hat{e}_z\}ds$$
$$+ \iint_{S_s} \rho_\infty\vec{V}_\infty\vec{V}_\infty\cdot\hat{n}_s ds = 0 \quad . \tag{2.5}$$

By means of Eq. (2.4), Eq. (2.5) can be rewritten

$$\iint_{S_c}(p-p_\infty)\hat{n}_c ds = - \iint_{S_b}\{\rho(\vec{V}-\vec{V}_\infty)(\vec{V}\cdot\hat{e}_z) + (p-p_\infty)\hat{e}_z\}ds \tag{2.6}$$

The left hand side of Eq. (2.6) is the force acting on the waverider stemming from the excess pressure on the compression stream surface. We assume that the flow is symmetric about the x-z plane such that the side force in the y direction vanishes. The force can thus be resolved into a lift component in the negative x direction and a drag component in the z direction as

$$\begin{aligned} L &\equiv - \hat{e}_x \cdot \iint_{S_c}(p-p_\infty)\hat{n}_c\, ds \\ &= \iint_{S_b} \rho(\vec{V}\cdot\hat{e}_x)(\vec{V}\cdot\hat{e}_z)ds \quad , \end{aligned} \tag{2.7}$$

$$D \equiv - \hat{e}_z \cdot \iint_{S_c}(p-p_\infty)\hat{n}_c\, ds$$

$$= \iint_{S_b} \{\rho(\vec{V}\cdot\hat{e}_z - V_\infty))(\vec{V}\cdot\hat{e}_z) + (p-p_\infty)\} ds \qquad (2.8)$$

2.2 Non-Axisymmetric Flow Field

Let us consider the case that the compression stream surface is generated from a flow of a conical body, its cross-section slightly deviating from a circle. Such body and corresponding shock can be expressed in spherical polar coordinate system as shown in Fig. 2.2,

$$\theta_b = \delta + \varepsilon_n \cos n\phi \qquad (2.9)$$

$$\theta_s = \beta + \varepsilon_n g_n \cos n\phi \qquad (2.10)$$

where ε_n = small perturbation parameter,

δ = semi-vertex angle of the basic circular cone,

β = semi-vertex angle of the circular shock,

g_n = ratio between perturbation of the shock and perturbation of the body.

When n = 0, Eq. (2.9) and Eq. (2.10) represents another circular cone, the n = 1 case represents an inclined cone, and the n = 2 case is an elliptic-cone case.

The flow variables are expanded in powers of ε_n as

$$\begin{aligned} \vec{V} &= u\,\hat{e}_r + v\,\hat{e}_\theta + w\,\hat{e}_\phi \\ &= (u_o(\theta) + \varepsilon_n\, u_n(\theta)\cos n\phi)\,\hat{e}_r \\ &\quad + (v_o(\theta) + \varepsilon_n v_n(\theta)\cos n\phi)\,\hat{e}_\theta \\ &\quad + (\varepsilon_n w_n(\theta)\,\sin n\phi)\hat{e}_\phi + O(\varepsilon_n{}^2) \\ p &= p_o(\theta) + \varepsilon_n p_n \cos n\phi + O(\varepsilon_n{}^2) \\ \rho &\cong \rho_o(\theta) \end{aligned} \qquad (2.11)$$

where u_o, v_o, and p_o are the components of the velocity in spherical

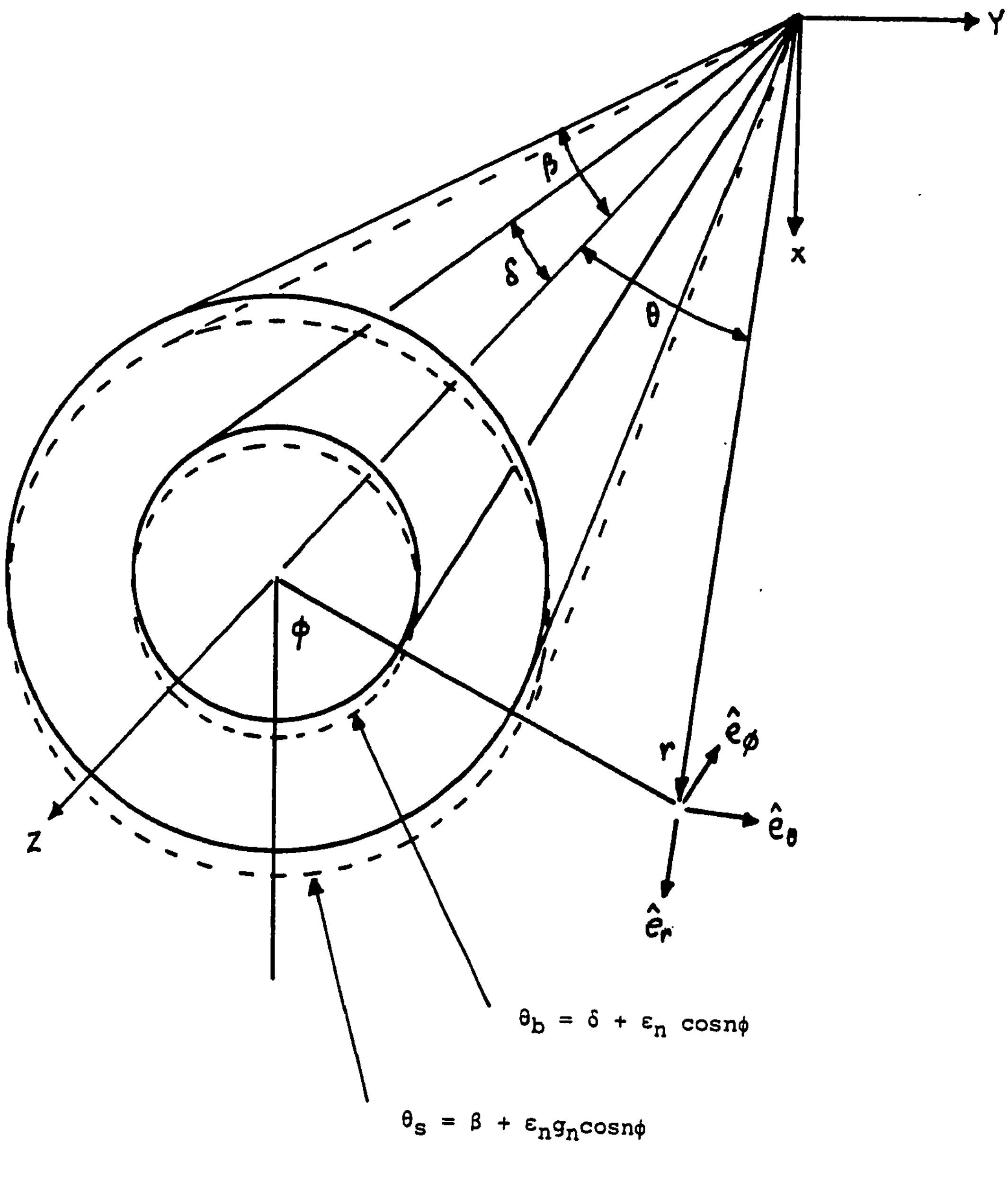

Fig. 2.2 A Non-Axisymmetric Body and Shock in Spherical Polar Coordinate System.

polar coordinates and the pressure of the zeroth order solution which is the solution of a circular cone flow. The subscript n indicates the first-order solutions of case n. The analytic approximate solutions for the first order are available from the papers [8,9,10] and are shown good agreement with experiments when ε_n is small. Those solutions are given in Appendix A in this paper.

The shock layer base area S_b also can be divided into two areas in similar manner as

$$S_b = S_{bo} + S_{bn} \tag{2.12}$$

Where S_{bo} is the shock layer base area between the trailing edge of the compression stream surface and the circular shock $\theta_s = \beta$ in the base plane, the area S_{bn} which is much smaller than S_{bo} is the area surrounded by the circular shock $\theta_s = \beta$ and non-circular shock $\theta_s = \beta + \varepsilon_n g_n \cos n\phi$ and the trailing edge of the compression stream surface as shown in Fig. 2.3.

Substituting Eq. (2.11) and (2.12) into Eq. (2.7) and (2.8) and by using the relations between unit vectors

$$\begin{aligned}
\hat{e}_r &= \hat{e}_x \sin\theta\cos\phi + \hat{e}_y \sin\theta \sin\phi + \hat{e}_z \cos\theta \quad , \\
\hat{e}_\theta &= \hat{e}_x \cos\theta\cos\phi + \hat{e}_y \cos\theta \sin\phi - \hat{e}_z \sin\theta \quad , \\
\hat{e}_\phi &= -\hat{e}_x \sin\phi + \hat{e}_y \cos\phi \quad ,
\end{aligned} \tag{2.13}$$

We can get

$$\begin{aligned}
L = &\iint_{S_{bo}+S_{bn}} \rho_o \cos\phi (u_o \sin\theta + v_o \cos\theta)(u_o \cos\theta - v_o \sin\theta)\, ds \\
&+ \varepsilon_n \iint_{S_{bo}} [\rho_o\{(u_n \sin\theta + v_n \cos\theta)\cos n\phi \cos\phi - w_n \sin n\phi \sin\phi\} \\
&\cdot (u_o \cos\theta - v_o \sin\theta)
\end{aligned} \tag{2.14}$$

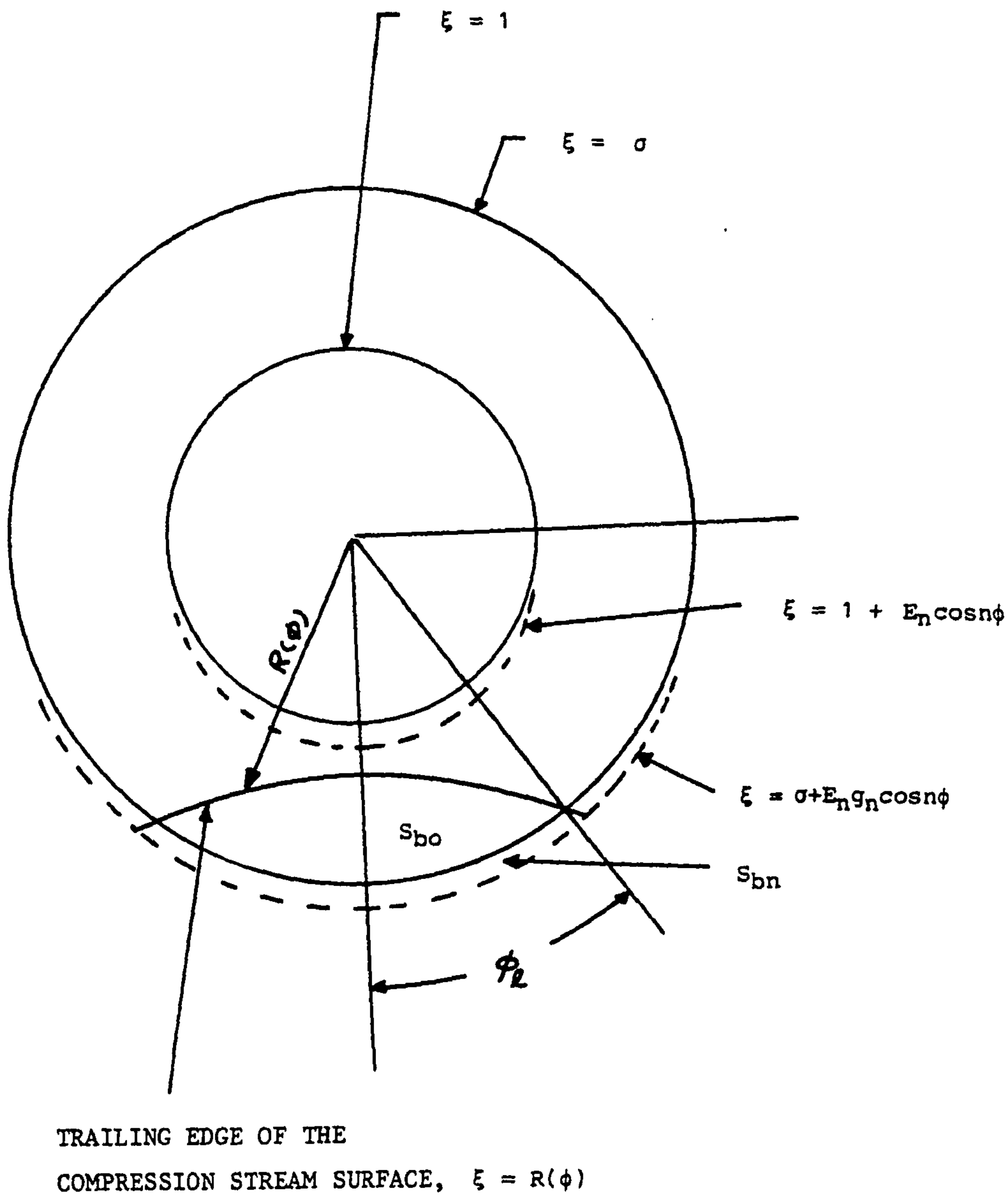

Fig. 2.3 The End View of Trailing Edge of a Compression Stream Surface ($\xi = \theta/\delta$, $E_n = \epsilon_n/\delta$).

$$+ (u_o\sin\theta + v_o\cos\theta)(u_n\cos\theta - v_n\sin\theta)\cos n\phi\cos\phi]\, ds$$

$$+ O(\varepsilon_n^2)$$

$$D = -\iint_{S_{bo}+S_{bn}} \{(p_o - p_\infty) + \rho_o(u_o\cos\theta - v_o\sin\theta - V_\infty)(u_o\cos\theta - v_o\sin\theta)\} ds$$

$$- \varepsilon_n \iint_{S_{bo}} \{p_n + 2\rho_o(u_o\cos\theta - v_o\sin\theta)(u_n\cos\theta - v_n\sin\theta) \tag{2.15}$$

$$- \rho_o V_\infty(u_n\cos\theta - v_n\sin\theta)\} \cos n\phi \, ds$$

$$+ O(\varepsilon_n^2)$$

2.3 Approximate Solutions for Hypersonic Flow

Consider the flow field past a slender body at very high speed such that $\delta \to 0$ and $M_\infty \to \infty$ but the combination $K_\delta = M_\infty \delta$ remains finite. In this hypersonic flow the basic circular cone flow can be approximated by

$$\frac{u_o}{V_\infty} \cong 1 - \frac{\delta^2}{2}\left\{\frac{\theta^2}{\delta^2} + \ln\left(\frac{\beta^2}{\theta^2}\right)\right\}$$

$$\frac{v_o}{V_\infty} \cong -\theta\left(1 - \frac{\delta^2}{\theta^2}\right)$$

$$\frac{p_o}{p_\infty} \cong 1 - \frac{\gamma}{2} K_\delta^2\left[1 + \frac{\rho_o(\beta)}{\rho_\infty}\left(1 - \frac{\delta^2}{\theta^2} + \ln\frac{\beta^2}{\theta^2}\right)\right]$$

$$\frac{T_o}{T_\infty} \cong 1 - \frac{\gamma-1}{2} K_\delta^2\left(2 - \frac{\delta^2}{\theta^2} + \ln\frac{\beta^2}{\theta^2}\right)$$

$$\frac{\rho_o}{\rho_\infty} \cong \frac{\rho_o(\beta)}{\rho_\infty}\left[1 + \frac{K_\delta^2}{2(T_o/T_\infty)}\left(\frac{\delta^2}{\beta^2} - \frac{\delta^2}{\theta^2} + \ln\frac{\beta^2}{\theta^2}\right)\right] \tag{2.16}$$

where $$\frac{\rho_o(\beta)}{\rho_\infty} = \frac{\sigma^2}{\sigma^2 - 1}$$

and $$\sigma \equiv \frac{\beta}{\delta} = \left(\frac{\gamma+1}{2} + \frac{1}{K_\delta^2}\right)^{1/2}$$

The approximate first order solutions u_n, v_n, w_n and p_n are given in Appendix A. The density term inside the lift and drag integrals can be approximated as $\rho_o \cong \rho_o(\beta)$ since the hypersonic approximate solutions are obtained by using the constant-density approximation which leads to very accurate results. Substituting the hypersonic approximate zeroth order and first order solutions into Eq. (2.14) and Eq. (2.15) and using $\sin\theta \cong \theta$, $\cos\theta \cong 1 - \frac{\theta^2}{2}$ and $ds \cong \ell^2\theta d\theta d\phi$, we can get to the lowest order in θ as

$$L = \ell^2\rho_o(\beta)\iint_{S_{bo}+S_{bn}} V_\infty{}^2\delta^2\cos\phi d\theta d\phi$$
$$+ \varepsilon_n\ell^2\rho_o(\beta)\iint_{S_{bo}} V_\infty(v_n\cos n\phi\cos\phi - w_n\sin n\phi\sin\phi)\theta d\theta d\phi \qquad (2.17)$$

and

$$D = \ell^2\rho_o(\beta)\iint_{S_{bo}+S_{bn}} \left\{\delta^2V_\infty\left(1+\ell n\frac{\beta}{\theta}\right) - (p_o-p_\infty)/\rho_o(\beta)\right\}\theta d\theta d\phi$$
$$+ \varepsilon_n\ell^2\rho_o(\beta)\iint_{S_{bo}} \{V_\infty(v_n\theta-u_n) - p_n/\rho_o(\beta)\} \cos n\phi\theta d\theta d\phi \qquad (2.18)$$

The first order pressure term in Eq. (2.18) can be replaced by velocity terms by using p_n solution in Appendix A

$$p_n = -\rho_o(u_ou_n + v_ov_n + f_n) \quad , \qquad (2.19)$$

where $f_n = \beta V_\infty{}^2 g_n(1-\rho_\infty/\rho_o(\beta))^2$. The result is

$$V_\infty(v_n\theta-u_n) - p_n/\rho_o(\beta) = \frac{\delta^2}{6} v_n + f_n \quad . \qquad (2.20)$$

It is useful to write Eq. (2.17) and Eq. (2.18) in dimensionless form by using following new variables

$$\xi = \theta/\delta \quad , \quad E_n = \varepsilon_n/\delta \quad ,$$
$$U_n = u_n/(\delta V_\infty) \quad , \quad V_n = v_n/V_\infty \quad ,$$
$$W_n = w_n/V_\infty \quad , \quad F_n = f_n/(\delta V_\infty{}^2) \quad ,$$
$$C_{po} = 2(p_o-p_\infty)/(\rho_\infty V_\infty{}^2) \quad . \qquad (2.21)$$

Using Eq. (2.20) and Eq. (2.21), the lift and drag can be rewritten as

$$\frac{L}{2q\ell^2} = \frac{\delta^3\sigma^2}{\sigma^2-1} \iint_{S_{bo}+S_{bn}} \cos\phi \; d\xi d\phi$$

$$+ \frac{E_n\delta^3\sigma^2}{\sigma^2-1} \iint_{S_{bo}} [V_n(\xi)\cos n\phi\cos\phi - W_n(\xi)\sin n\phi\sin\phi]\xi d\xi d\phi \quad (2.22)$$

$$\frac{D}{2q\ell^2} = \frac{\delta^4\sigma^2}{\sigma^2-1} \iint_{S_{bo}+S_{bn}} \frac{\sigma^2+\xi^2}{2\xi\sigma^2} d\xi d\phi$$

$$+ \frac{E_n\delta^4\sigma^2}{\sigma^2-1} \iint_{S_{bo}} [V_n(\xi) + \xi \; F_n]\cos n\phi d\xi d\phi \quad (2.23)$$

where $\quad q = \frac{1}{2} \rho_\infty V_\infty{}^2$

and $\quad \frac{C_{po}(\theta)}{\delta^2} = 1 + \frac{\rho_o(\beta)}{\rho_\infty} \left(1 - \frac{\delta^2}{\theta^2} + \ell n \frac{\beta^2}{\delta^2}\right) ,$

$$\frac{\rho_o(\beta)}{\rho_\infty} = \frac{\sigma^2}{\sigma^2-1}$$

are used.

2.4 Trailing Edge Function

Let the trailing edge of the compression stream surface be denoted by $\xi = R(\phi)$ in the shock layer base plane where $R(\phi)$ is arbitrary function of ϕ only. We assume that the compression stream surface intersects the circular shock at $\phi = \phi_\ell$, say $\sigma = R(\phi_\ell)$, as shown in Fig. 2.3. Since we have assumed that the waverider configuration is symmetric about x-z plane, the surface integrals over the shock layer base area can be written in terms of $R(\phi)$ as

$$\iint_{S_{bo}} = 2 \int_{o}^{\phi_\ell} \int_{R(\phi)}^{\sigma} \quad , \quad (2.24)$$

$$\iint_{S_{bn}} = 2 \int_{o}^{\phi_\ell} \int_{\sigma}^{\sigma+E_n g_n \cos n\phi} \quad . \quad (2.25)$$

Finally the lift and drag become

$$L = 4q\ell^2\ \delta^3 \frac{\sigma^2}{\sigma^2-1} \int_0^{\phi_\ell} [\{\sigma-R(\phi)\}\ \cos\phi$$

$$+ E_n \int_{R(\phi)}^{\sigma} \xi\{V_n(\xi)\cos n\phi\cos\phi - W_n(\xi)\sin n\phi\sin\phi\}d\xi$$

$$+ E_n g_n \cos n\phi\cos\phi]\ d\phi \tag{2.26}$$

$$D = 4q\ell^2\ \delta^4 \frac{\sigma^2}{\sigma^2-1} \int_0^{\phi_\ell} [\{\frac{\sigma^2-R^2(\phi)}{4\sigma^2} - \frac{1}{2}\ \ell n\ \frac{R(\phi)}{\sigma}\}$$

$$+ E_n \int_{R(\phi)}^{\sigma} \{V_n(\xi) + \xi\ F_n\}\ \cos n\phi\ d\xi$$

$$+ \frac{E_n g_n}{\sigma} \cos n\phi]\ d\phi \quad . \tag{2.27}$$

Therefore, whenever we know the free stream condition q, slenderness factor δ, length ℓ and dihedral angle ϕ_ℓ, and the trailing edge function $R(\phi)$ of the waverider configuration, we can determine the geometry and aerodynamic forces of the waverider completely.

SECTION III

THE OPTIMIZATION PROBLEM

3.1 Maximum Lift-to-Drag Ratio

It has been shown that a waverider can be constructed from a known flow field by specifying the trailing edge function $R(\phi)$ which in turn completely determines the aerodynamic properties such as lift and drag. A practical question naturally arises as to the feasibility of obtaining in a specific flow field, a particular waverider which has optimum aerodynamic properties.

There are several variational problems pertaining to optimum shapes of waveriders according to what property of a waverider is specified. One of the properties is the lift-to-drag ratio. The L/D ratio is one of the most important factors related to the range and fuel efficiency of a waverider. Therefore, the variational problem of maximizing the the L/D ratio subject to an appropriate constraint condition such as fixed lift, drag, volume, or project planform area of the waverider, seems to be the most interesting and useful from a practical point of view.

3.2 Variational Problem

Let lift and drag and constraint functionals be in the form

$$L = 4q\ell^2\delta^3 \frac{\sigma^2}{\sigma^2-1} \int_0^{\phi_\ell} F_\ell(R(\phi),\phi;\ \sigma,\ E_n)\ d\phi \quad ,$$

$$D = 4q\ell^2\delta^4 \frac{\sigma^2}{\sigma^2-1} \int_0^{\phi_\ell} F_d(R(\phi),\phi;\ \sigma,\ E_n)\ d\phi \quad ,$$

$$G = g(q,\ell,\delta,\sigma) \int_0^{\phi_\ell} F_g(R(\phi),R'(\phi),\phi;\ \sigma,\ E_n)\ d\phi \quad , \tag{3.1}$$

where G is a constraint functional and $R'(\phi)$ denotes the first derivative of $R(\phi)$ with respect to ϕ. Notice that the lift and drag functionals do not have the first derivative of the trailing edge function $R(\phi)$. If other parameters are all fixed, the variational problem is to determine the function $R(\phi)$, the associated value of dihedral angle ϕ_ℓ, and the thickness ratio δ which serve the purpose.

Following the standard calculus of variational scheme, we form the functional

$$H = L/D + \lambda G \tag{3.2}$$

where λ is a Language multiplier and L, D, and G are given in Eq. (3.1). In order to get the solution, the following variational operation must be satisfied:

$$\bar{\delta} H = 0 \tag{3.3}$$

which leads to

$$\frac{1}{\delta I_d}\left[\bar{\delta} I_\ell - \frac{I_\ell}{I_d} + \lambda\delta g I_d\ \bar{\delta} I_g\right] = 0 \tag{3.4}$$

where

$$I_\ell = \int_0^{\phi_\ell} F_\ell(R,\phi;\sigma,E_n)\ d\phi \quad ,$$

$$I_d = \int_0^{\phi_\ell} F_d[R,\phi;\sigma,E_n)\ d\phi \quad ,$$

$$I_g = \int_0^{\phi_\ell} F_g[R,R',\phi;\sigma,E_n)\ d\phi \qquad ,$$

and $\bar{\delta}$ is variational operator.

Since F_ℓ and F_d do not depend on $R'(\phi)$, the vanishing of the terms in brackets leads to the Euler-Lagrange equation

$$\frac{\partial F_\ell}{\partial R} - \frac{I_\ell}{I_d}\frac{\partial F_d}{\partial R} + \delta\lambda g\ I_d\left(\frac{\partial F_g}{\partial R} - \frac{d}{d\phi}\frac{\partial F_g}{\partial R'}\right) = 0 \qquad (3.5)$$

The associated transversality condition for the variable end point at $\phi = \phi_\ell$ is [17]

$$\left[F_\ell - \frac{I_\ell}{I_d}F_d + \delta\lambda g I_d\left(F_g - R'\frac{\partial F_g}{\partial R'}\right)\right]_{\phi=\phi_\ell} = 0 \qquad (3.6)$$

In addition to Eq. (3.5) and Eq. (3.6), we impose additional requirements for $R(\phi)$ as follows:

a) The trailing edge function $R(\phi)$ is symmetric with respect to $\phi = 0$ as we assumed earlier.

b) The azimuthal dimension of the surface is within the region $0 \leq \phi \leq \frac{\pi}{2}$.

c) The trailing edge curve lies in the shock layer, $1 \leq R(\phi) \leq \sigma$ for $0 \leq \phi \leq \phi_\ell$.

The cases where $R(\phi) < 1$ are not permissible since a shock layer stream surface can not lie inside the surface of the basic body itself.

It thus transpires that there are two classes of solutions: one in which the condition $1 < R(\phi) \leq \sigma$ is valid for all ϕ in $0 \leq \phi \leq \phi_\ell$; and in which $1 \leq R(\phi) \leq \sigma$ in the range $\phi_\delta \leq \phi \leq \phi_\ell$, where $R(\phi_\delta) = 1$, and the remaining part of compression stream surface is the basic body itself $R(\phi) = 1$. The latter is referred to as class A and the former as class B as shown in Fig. 3.1.

At this stage, the waverider configuration is said to be semi-optimized. In addition, we wish to vary δ, hence we have the usual method of differential calculus as

$$\frac{\partial H}{\partial \delta} = 0 \quad . \tag{3.7}$$

After the final imposition of this condition, the waverider configuration is said to be fully optimized.

3.3 Lift-Fixed Constraint

For the special case of constraint condition, lift-fixed, we set G = L and hence

$$g = 4q\ell^2 \, \delta^3 \frac{\sigma^2}{\sigma^2-1}$$

and $F_g = F_\ell$. The Lagrange equation of Eq. (3.5) becomes

$$\frac{\partial}{\partial R} (F_d + \lambda^* F_\ell) = 0 \tag{3.8}$$

where
$$\lambda^* = - \frac{1 + \delta\lambda g I_d}{I_\ell / I_d}$$

and the transversality condition of Eq. (3.6) becomes

$$[F_d + \lambda^* F_\ell]_{\phi=\phi_\ell} = 0 \quad . \tag{3.9}$$

The other condition, Eq. (3.7) becomes

$$\frac{\partial}{\partial \delta} [D + \lambda^* L] = 0 \quad . \tag{3.10}$$

For this case, the variational problem also can be interpreted as finding the minimum drag configuration for a fixed amount of lift since Eq. (3.8), (3.9), and (3.10) can be obtained by setting new functional as H = D + λ^*L. In the following sections, we will determine the function R(ϕ) which minimizes the drag with a fixed lift for each value of n.

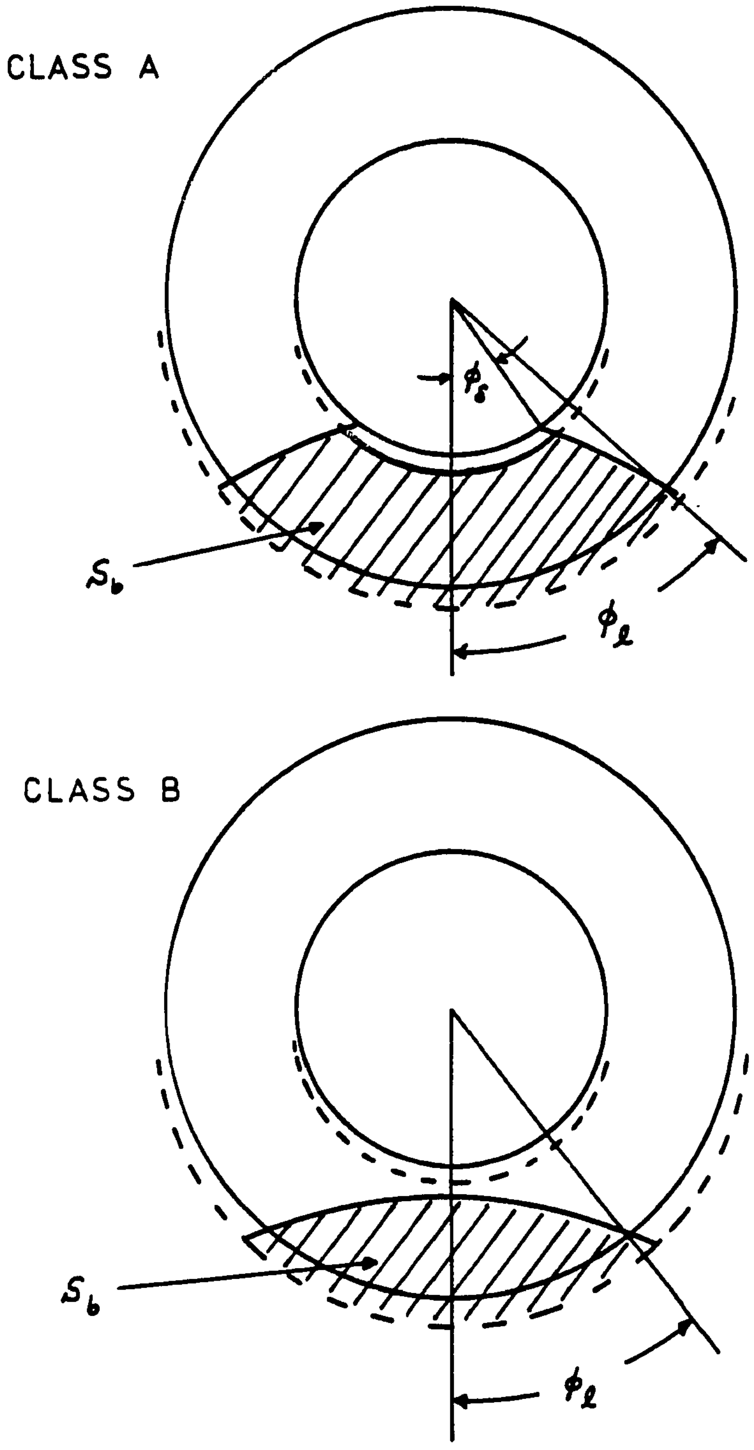

Fig. 3.1 The Trailing Edge of the Compression Stream Surface of Class-A and Class-B Configurations.

SECTION IV

WAVERIDER CONFIGURATIONS OF $E_n = 0$ CASE

4.1 Semi-Optimized Configurations

Let us consider the problem of optimization that determines the function $R(\phi)$ which minimize drag with a fixed lift when $E_n = 0$. This is the case that the waverider configuration is generated from the axisymmetric flow past a circular cone. After setting $E_n = 0$ in Eq. (2.26) and (2.27), the lift and drag are written as

$$L = 4q\ell^2\delta^3 \frac{\sigma^3}{\sigma^2-1} \int_0^{\phi_\ell} \left(1 - \frac{R(\phi)}{\sigma}\right) \cos\phi \, d\phi \quad , \tag{4.1a}$$

$$D = q\ell^2\delta^4 \frac{\sigma^2}{\sigma^2-1} \int_0^{\phi_\ell} \left[\frac{\sigma^2-R^2(\phi)}{\sigma^2} - \ln \frac{R^2(\phi)}{\sigma^2} \right] d\phi \quad , \tag{4.1b}$$

where q and ℓ are assumed fixed.

Taking variations of the functional

$$H = D + \lambda L \tag{4.2}$$

where λ is a Lagrange multiplier, we can get the Euler-Lagrange equation

$$R^2(\phi) + \frac{2\lambda\sigma^2}{\delta} \cos\phi R(\phi) + \sigma^2 = 0 \tag{4.3}$$

and the transversality condition as

$$\left[\frac{\sigma^2-R^2}{\sigma^2} - \ln \frac{R^2}{\sigma^2} + \frac{4\sigma\lambda}{\delta} \left(1 - \frac{R}{\sigma}\right)\right]_{\phi=\phi_\ell} = 0 \quad . \tag{4.4}$$

Enforcing the boundary condition $R(\phi_\ell) = \sigma$, we can get

$$\lambda = -\frac{\delta}{\sigma\cos\phi_\ell} \tag{4.5}$$

from Eq. (4.3), and Eq. (4.4) is automatically satisfied. By substituting Eq. (4.5) into Eq. (4.3), we get

$$R^2 - 2\sigma\frac{\cos\phi}{\cos\phi_\ell}R + \sigma^2 = 0 \tag{4.6}$$

which is algebraic equation to be solved easily and the solution is

$$R(\phi) = \frac{\sigma}{\cos\phi_\ell}\left[\cos\phi \pm (\cos^2\phi - \cos^2\phi_\ell)^{1/2}\right] \quad , \tag{4.7}$$

For $\phi = 0$, $R(\phi)$ becomes

$$R(0) = \frac{\sigma}{\cos\phi_\ell}(1 \pm \sin\phi_\ell) \quad . \tag{4.8}$$

If the plus sign is used, we get $R(0) > \sigma$., which is improper with the real waverider which is $1 < R(\phi) < \sigma$. Then using the minus sign only, we finally get

$$R(\phi) = \frac{\sigma}{\cos\phi_\ell}\left[\cos\phi - (\cos^2\phi - \cos^2\phi_\ell)^{1/2}\right] \quad . \tag{4.9}$$

The critical value of ϕ_ℓ, denoted by $\phi_{\ell c}$, occurs when $R(0) = 1$. The value of $\phi_{\ell c}$ can be determined from Eq. (4.9) to be

$$\sin\phi_{\ell c} = \frac{\sigma^2-1}{\sigma^2+1} \quad . \tag{4.10}$$

and plotted in Fig. 4.1 as a function of k_δ. When ϕ_ℓ is greater than $\phi_{\ell c}$, the function $R(\phi)$ in Eq. (4.9) cannot satisfy the condition $1 < R(\phi) < \sigma$ for all values of ϕ in the range $0 < \phi < \phi_\ell$. The cases where $R(\phi) < 1$ are not permissible since a shock layer stream surface cannot lie inside the surface of the original cone itself. Therefore, when $\phi_\ell > \phi_{\ell c}$, we have class A waverider instead of class B waverider and the optimum function $R(\phi)$ has to be obtained by the following approach.

Suppose the trailing edge of the compression stream surface consists of two curves

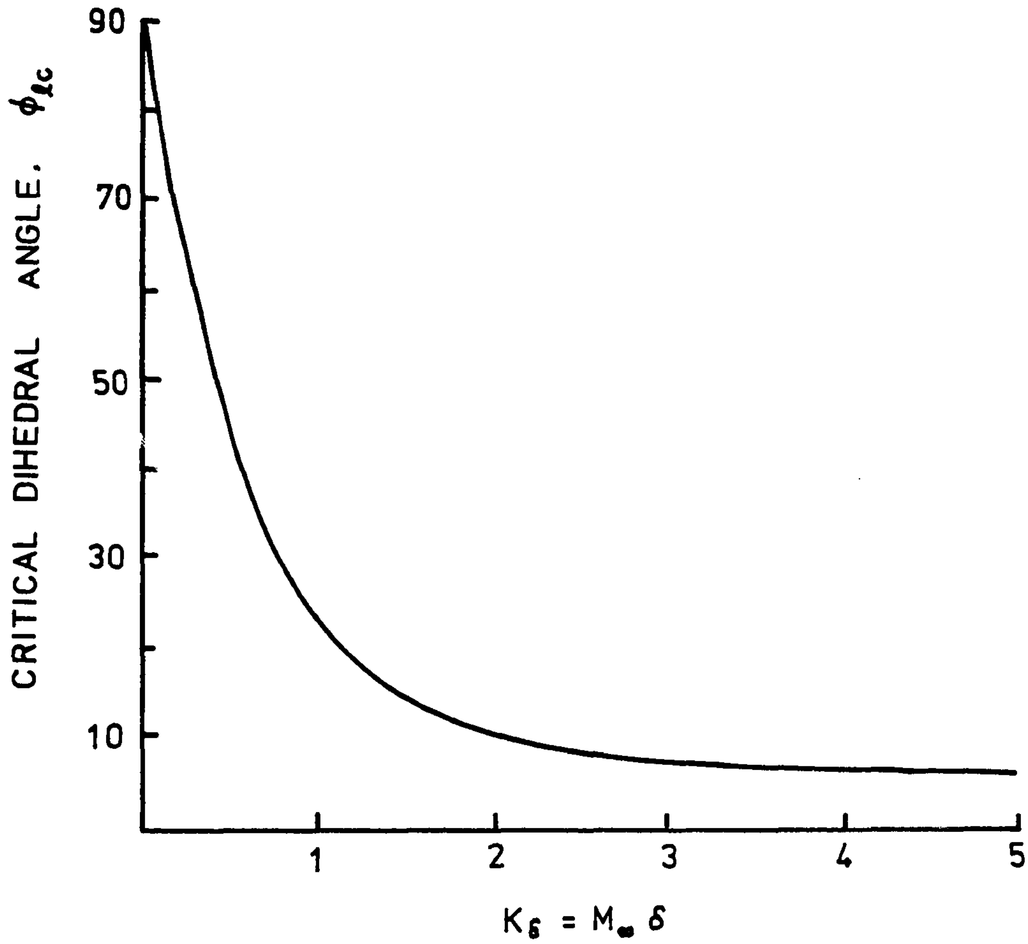

Fig. 4.1 A Critical Dihedral Angle for Semi-Optimized Waverider (γ = 1.4).

$$\begin{cases} \xi = 1 & \text{for} \quad 0 < \phi < \phi_\delta \\ \xi = R(\phi) & \text{for} \quad \phi_\delta < \phi < \phi_\ell \end{cases} \tag{4.11}$$

where ϕ_δ satisfies $R(\phi_\delta) = 1$. Then the lift and drag functionals are

$$L = 4q\ell^2\delta^3 \frac{\sigma^3}{\sigma^2-1} \left[\int_0^{\phi_\delta}\left(1 - \frac{1}{\sigma}\right) \cos\phi \, d\phi + \int_{\phi_\delta}^{\phi_\ell}\left(1 - \frac{R}{\sigma}\right) \cos\phi d\phi\right] \tag{4.12a}$$

$$D = q\ell^2\delta^4 \frac{\sigma^2}{\sigma^2-1} \left[\int_0^{\phi_\delta}\left(\frac{\sigma^2-1}{\sigma^2} + \ell n\sigma^2\right) d\phi + \int_{\phi_\delta}^{\phi_\ell}\left(\frac{\sigma^2-R^2}{\sigma^2} - \ell n \frac{R^2}{\sigma^2}\right) d\phi\right] . \tag{4.12b}$$

By taking variations of the functional $H = D + \lambda L$ we can get the same Euler-Lagrange equation as in Eq. (4.3) and transversality conditions are

$$\left[\frac{\sigma^2-R^2}{\sigma^2} - \ell n \frac{R^2}{\sigma^2} + \frac{4\sigma\lambda}{\delta} \left(1 - \frac{R}{\sigma}\right)\right]_{\phi=\phi_\ell} = 0 \tag{4.13}$$

and

$$\left[\frac{\sigma^2-1}{\sigma^2} + \ell n\sigma^2 + \ell n \frac{R^2}{\sigma^2} + \frac{4\sigma\lambda}{\delta} \left(\frac{R}{\sigma} - \frac{1}{\sigma}\right)\right]_{\phi=\phi_\delta} = 0 \tag{4.14}$$

Both Eq. (4.13) and Eq. (4.14) are automatically satisfied since $R(\phi_\ell) = \sigma$ and $R(\phi_\delta) = 1$. The solution for $R(\phi)$ is again

$$R(\phi) = \begin{cases} 1 \quad \text{for} \quad 0 < \phi < \phi_\delta \\ \dfrac{\sigma}{\cos\phi_\ell} \left[\cos\phi - (\cos^2\phi - \cos^2\phi_\ell)^{1/2}\right] \text{ for } \phi_\delta < \phi < \phi_\ell \end{cases} \tag{4.15}$$

where $\phi_\ell > \phi_{\ell c}$. The value ϕ_δ can be determined from the condition $R(\phi_\delta) = 1$ and the result is

$$\cos\phi_\delta = \frac{\cos\phi_\ell}{\cos\phi_{\ell c}} \quad \text{for } \phi_\ell > \phi_{\ell c} \tag{4.16}$$

The solutions for $R(\phi)$, Eq. (4.9) for class B and Eq. (4.15) for class A, are called semi-optimized solutions because we only apply the condition $\delta H = 0$ but not $\partial H/\partial\delta = 0$.

4.2 Geometry of the Semi-Optimized Configurations

4.2.1 Free Stream Surfaces and Compression Stream Surfaces

Whenever the trailing edge of the compression stream surface is obtained, we can construct the corresponding compression stream surface and the free stream surface by using the streamline equations of a flow past a circular cone. The streamlines in the shock-layer are described by

$$\vec{V} \times d\vec{s} = 0 \tag{4.17}$$

where $\vec{V}$ is velocity and $d\vec{s}$ is infinitesimal segment of the streamline. Eq. (4.17) can be rewritten in spherical polar coordinate system as

$$\frac{dr}{u_o} = \frac{r d\theta}{v_o} \quad \text{and} \quad \phi = \text{constant} \tag{4.18}$$

where u_o and v_o are two velocity components of the flow field past a circular cone. By using approximations for u_o and v_o in Eq. (2.16), we can get one family of arbitrary stream surface as

$$r \left(\frac{\theta^2-\delta^2}{\beta^2-\delta^2}\right)^{1/2} = r_s(\phi) \tag{4.19}$$

where $r_s(\phi)$ is an arbitrary function of ϕ. It is useful to interprete $r_s(\phi)$ as an arbitrary line drawn on the shock surface, and thus Eq. (4.19) describes the shock layer stream surface starting on the line $r = r_s(\phi)$ on the shock.

The function $r_s(\phi)$ can also be determined in terms of the trailing edge function $R(\phi)$. By setting

$$\theta = R(\phi)\delta \tag{4.20}$$

and

$$r = \ell \sec(R(\phi)\delta) \cong \ell$$

in Eq. (4.19), we obtain

$$r_s(\phi) = \ell\left(\frac{R^2(\phi)-1}{\sigma^2-1}\right)^{1/2} \quad . \tag{4.21}$$

Thus when $R(\phi)$ is specified as Eq. (4.9) and Eq. (4.15), the intersection of the compression stream surface with the shock is determined, along the complete compression stream surface itself from Eq. (4.19).

An arbitrary cylindrical surface parallel to the free-stream can be expressed as $r \sin\theta = f(\phi)$ where $f(\phi)$ is an arbitrary function of ϕ. Thus for small angle of θ, the free stream surface, which is upper surface of the waverider parallel to the freestream, intersecting the shock at $r_s(\phi)$ is given by

$$r\theta = r_s(\phi)\beta \tag{4.22a}$$

or

$$r\,\frac{\theta}{\beta} = \ell\left(\frac{R^2(\phi)-1}{\sigma^2-1}\right)^{1/2} \quad . \tag{4.22b}$$

Correspondingly, the trailing edge of the free stream surface in the base plane is obtained as

$$R_{fs}(\phi) \equiv \frac{\theta_{fs}(\phi)}{\delta} = \sigma\left(\frac{R^2(\phi)-1}{\sigma^2-1}\right)^{1/2} \tag{4.23}$$

by setting $r = \ell$ and $\theta = \theta_{fs}$ in Eq. (4.22). Thus when $R(\phi)$ is specified, the complete shape of the waverider can be determined as well as lift and drag.

In Fig. 4.2, examples of the trailing edge curves of both free stream surface and compression stream surfaces of the semi-optimized waverider configuration are shown for $K_\delta = 0.5$, 1.0, and 5.0. For each K_δ, there are shown class A shapes having pointed noses since stream-

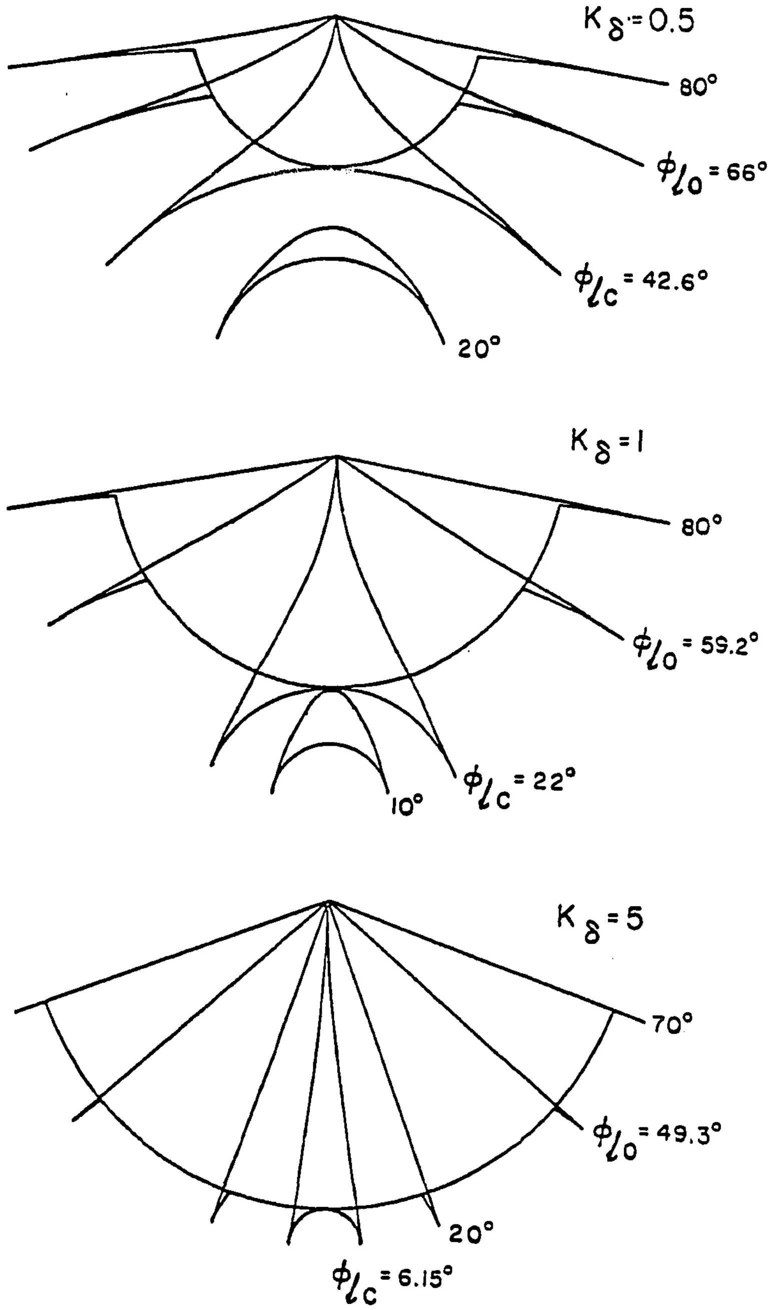

Fig. 4.2 Semi-Optimized Waverider Base Shapes K_δ=0.5, 1.0 and 5.0.

lines on the surface of the circular cone originate at the vertex. The class B has round noses with sharp lips since streamlines in the shock layer originate at some point on the shock surface.

Fig. 4.3 shows the end views, top views and side views of the waveriders for $K_\delta = 1.0$. The free stream surfaces are determined by means of Eq. (4.22). The class B shapes are not conical since the cross-sections are not similar as z varies. The winglets on the class A waveriders are not conical, although the cone segment of the compression stream surface for $0 < \phi < \phi_\delta$ of course is conical since it is part of the original conical cone body.

4.2.2 Non-Optimized Configurations

Along with the semi-optimized configurations, we consider non-optimized configurations for later use for comparison. The first example is waveriders with flat top surface as shown in Fig. 4.4. It has a flat free stream surface and its leading edge is a parabolic curve on the shock. Since the trailing edge of the free stream surface is a straight line in the base plane, the equation of the trailing edge of the free stream surface is

$$R_{fs} = \frac{\sigma\cos\phi_\ell}{\cos\phi} \tag{4.24}$$

and by using Eq. (4.23), the trailing edge of the compression stream surface of the flat top waverider is represented by

$$R(\phi) = \left[(\sigma^2-1)\frac{\cos^2\phi_\ell}{\cos^2\phi} + 1\right]^{1/2} \quad . \tag{4.25}$$

Notice that the original cone body does not become a part of the compression stream surface except for $\phi_\ell = 90°$ since $R(\phi)$ is always greater

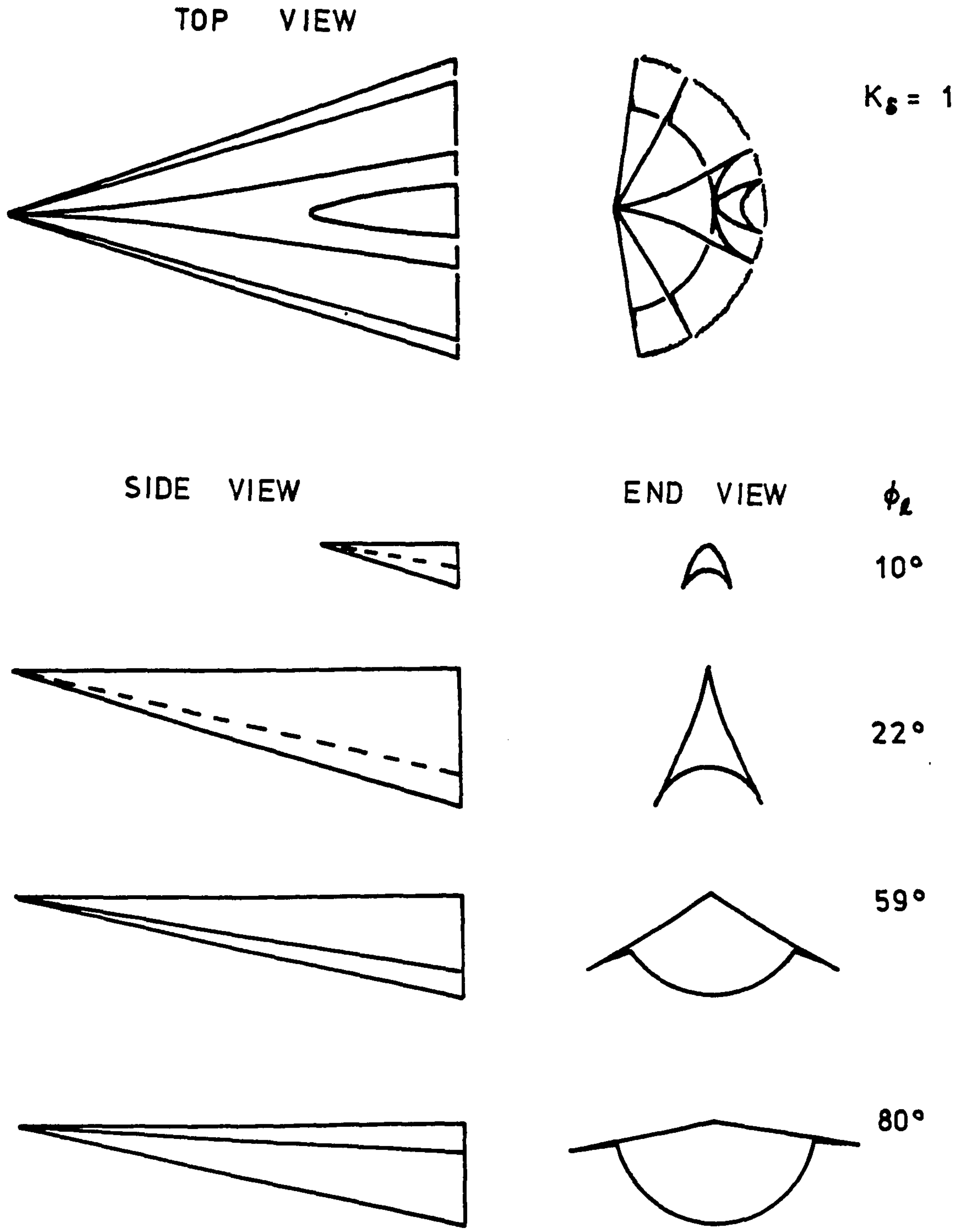

Fig. 4.3 Three Views of Semi-Optimized Waverider for K_δ=1.0.

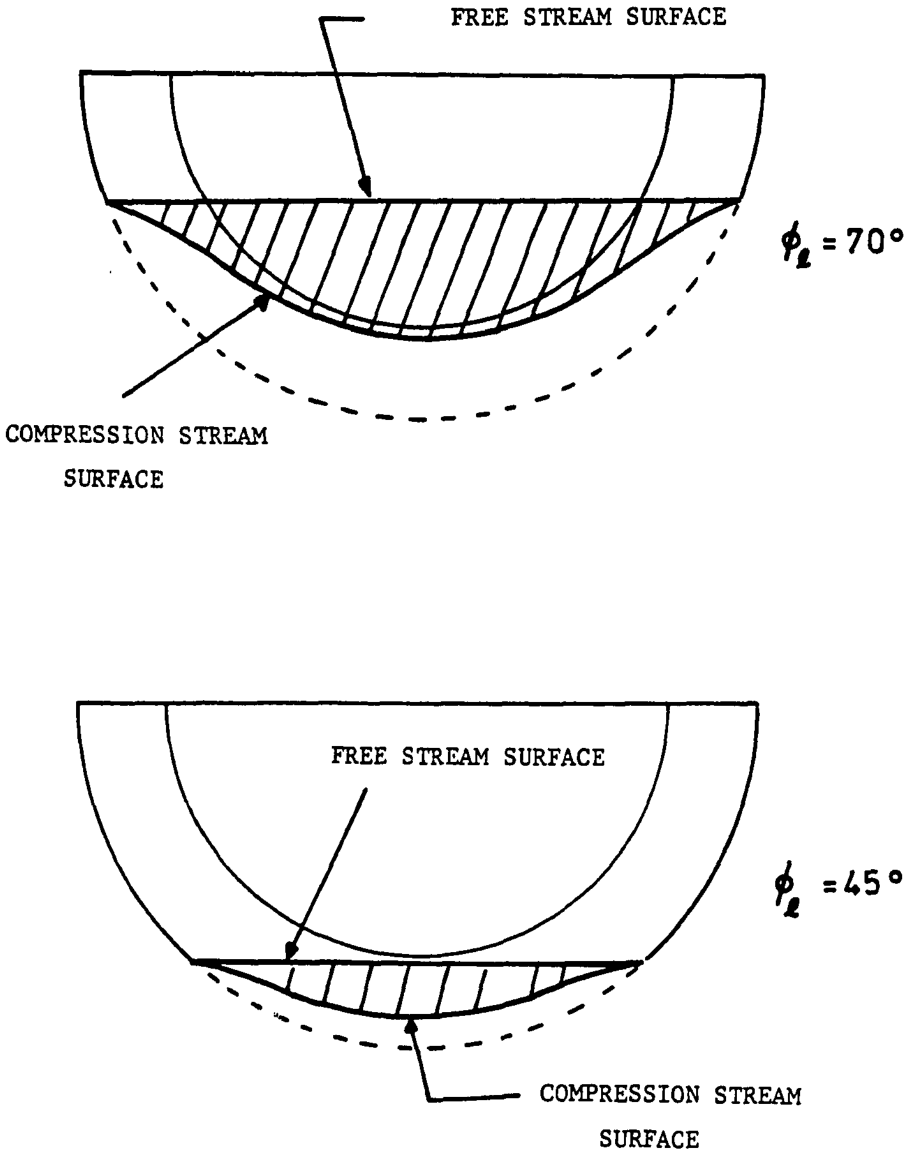

Fig. 4.4 End View of a Non-Optimized Waverider Configuration with Flat Top Free Stream Surface.

than unity for $0 < \phi < \phi_\ell$.

The second example of non-optimized body is the waverider in which its trailing edge of the compression stream surface is a straight line as shown in Fig. 4.5. The equation for the trailing edge in base plane is

$$R(\phi) = \frac{\sigma\cos\phi_\ell}{\cos\phi} \quad , \tag{4.26a}$$

for class-B type and

$$R(\phi) = \begin{cases} 1 \quad \text{for} \quad 0 < \phi < \phi_\delta \quad , \\ \dfrac{\sigma\cos\phi_\ell}{\cos\phi} \text{ for } \phi_\delta < \phi < \phi_\ell \quad , \end{cases} \tag{4.26b}$$

for class-A type where

$$\begin{aligned} \phi_\delta &= \cos^{-1}(\sigma\cos\phi_\ell) \ , \\ \phi_{\ell c} &= \cos^{-1}(1/\sigma) \quad . \end{aligned} \tag{4.27}$$

The trailing edge of the free stream surface is then obtained by using Eq. (4.23) as

$$R_{fs} = \frac{\sigma}{\cos\phi}\left(\frac{\sigma^2\cos^2\phi_\ell - \cos^2\phi}{\sigma^2-1}\right)^{1/2} \tag{4.28}$$

for $\phi_\delta < \phi < \phi_\ell$ where $\phi_\delta = 0$ for class B and ϕ_δ in Eq. (4.27) for class A.

The lift and drag for these non-optimized configurations can be calculated by using Eq. (4.1) and Eq. (4.12) for each class. These configurations are not optimized, so their L/D ratio should be less than the optimized body for given lift.

4.2.3 Other Geometric Variables

When the waverider configuration is known as a function of $R(\phi)$, other geometric variables of interest also can be determined. Among the variables of interest are the base area A_b, the volume V,

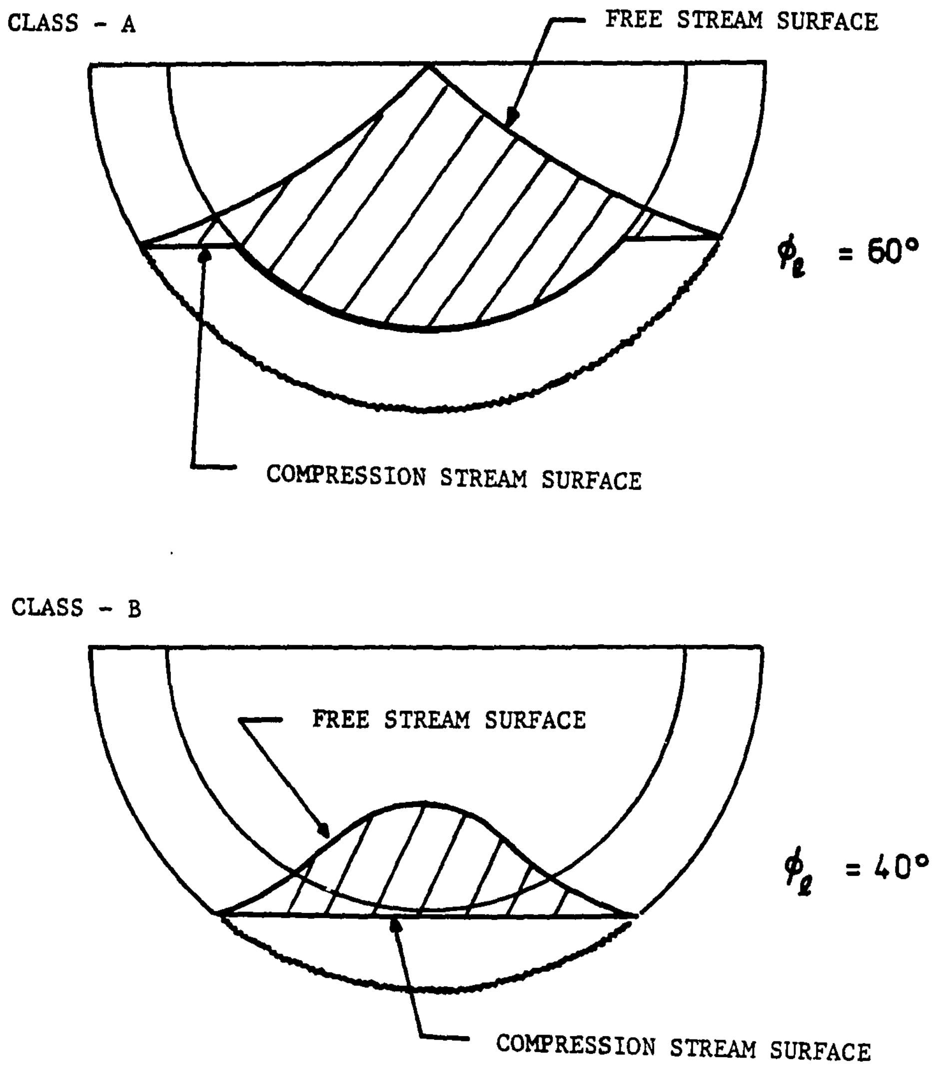

Fig. 4.5 Non-Optimized Waverider Configurations of Eq. (4.26).

projected planform area S_p onto y-z plane and wetted area S_w which is sum of two surface area of the compression stream surface and free stream surface. The variables can be determined by the following integrals.

$$A_b = \ell^2\delta^2 \int_0^{\phi_\ell}\left(1 - \frac{R^2-1}{\sigma^2-1}\right) d\phi$$

$$V = \ell^3\delta^2 \int_0^{\phi_\ell}\left[\frac{1}{3} - \frac{R^2-1}{\sigma^2-1} + \frac{2}{3}\left(\frac{R^2-1}{\sigma^2-1}\right)^{\frac{3}{2}}\right] d\phi \tag{4.29}$$

$$S_p = \frac{2\ell^2\delta\sigma}{\sigma^2-1}\int_0^{\phi_\ell} R\,\frac{dR}{d\phi}\,\sin\phi d\phi$$

$$S_w = 2\ell^2\delta \int_0^{\phi_\ell}\left[\sigma(1-z^2)\left(\frac{R^2R'^2}{z^2(\sigma^2-1)^2} + z^2\right)^{\frac{1}{2}} d\phi + \int_{z(\phi_\delta)}^{1}\left(\frac{R^2R'^2}{R^2+\zeta^2-1} + R^2+\zeta^2-1\right)^{\frac{1}{2}} d\zeta\right] d\phi$$

where

$$z = \left(\frac{R^2-1}{\sigma^2-1}\right)^{\frac{1}{2}}$$

As for the lift and drag functionals, these integrals also are functions of $R(\phi)$.

As basis for comparison with above variables, it is useful to consider a simple configuration that is a special case of non-optimized configurations and easy to visualize. This idealized waverider configuration is conical in shape with infinitesimally thin delta winglets as illustrated in Fig. 4.6. The particular results for all the geometric variables come from setting $R(\phi) = 1$ in all the integrals in Eq. (4.29) then we get

$$A_b{}^* = \ell^2\delta^2\phi_\ell \tag{4.30a}$$

$$V^* = \ell^3\delta^2\phi_\ell/3 \tag{4.30b}$$

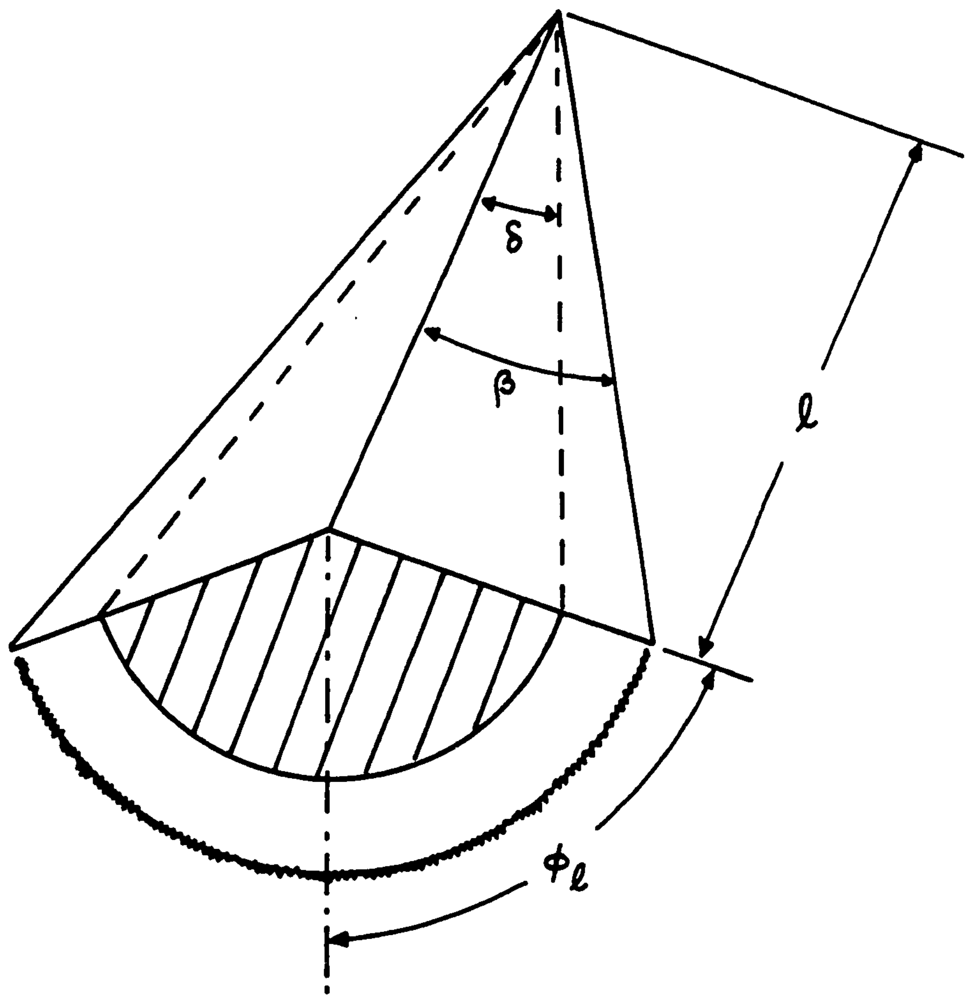

Fig. 4.6 An Idealized Cone Waverider.

$$S^* = \ell^2 \delta \sigma v \sin\phi_\ell \tag{4.30c}$$

$$S_w^* = \ell^2 \delta \; (2\sigma + \phi_\ell - 1) \tag{4.30d}$$

where the star denotes the idealized cone waverider case.

The base area, volume, projected planform area and wetted area for the semi-optimized configurations, ratioed with the corresponding values of the idealized cone waverider are shown in Fig. 4.7 through Fig. 4.10 as a function of dihedral angle ϕ_ℓ for various values of K_δ. For large values of K_δ, the idealized cone waverider provides a good approximation for the semi-optimized configurations, except for small dihedral angle ϕ_ℓ.

Out of the dimensional variables, there are two independent dimensionless combinations. One combination is $V^{2/3}/S_p$ which is regarded as a measure of volume and another combination is A_b/S_p which can be regarded as a measure of slenderness. For the semi-optimized configurations, these two combinations, in ratio with their counterparts for the idealized cone waverider, are shown in Fig. 4.11 and Fig. 4.12 as a function of ϕ_ℓ for various values of K_δ. For the class A configurations, the ratio V/S_p is smaller than its counterpart for the idealized cone waverider by less than ten percent. The effective slenderness ratio A_b/S_p is only slightly smaller for all conditions than its counterpart for the idealized cone waverider.

4.3 Lift and Drag of Semi-Optimized Configurations

The lift and drag of the semi-optimized configurations can be obtained by performing integration for the integrals in Eq. (4.12) for class A and Eq. (4.1) for class B. By substituting the solution $R(\phi)$

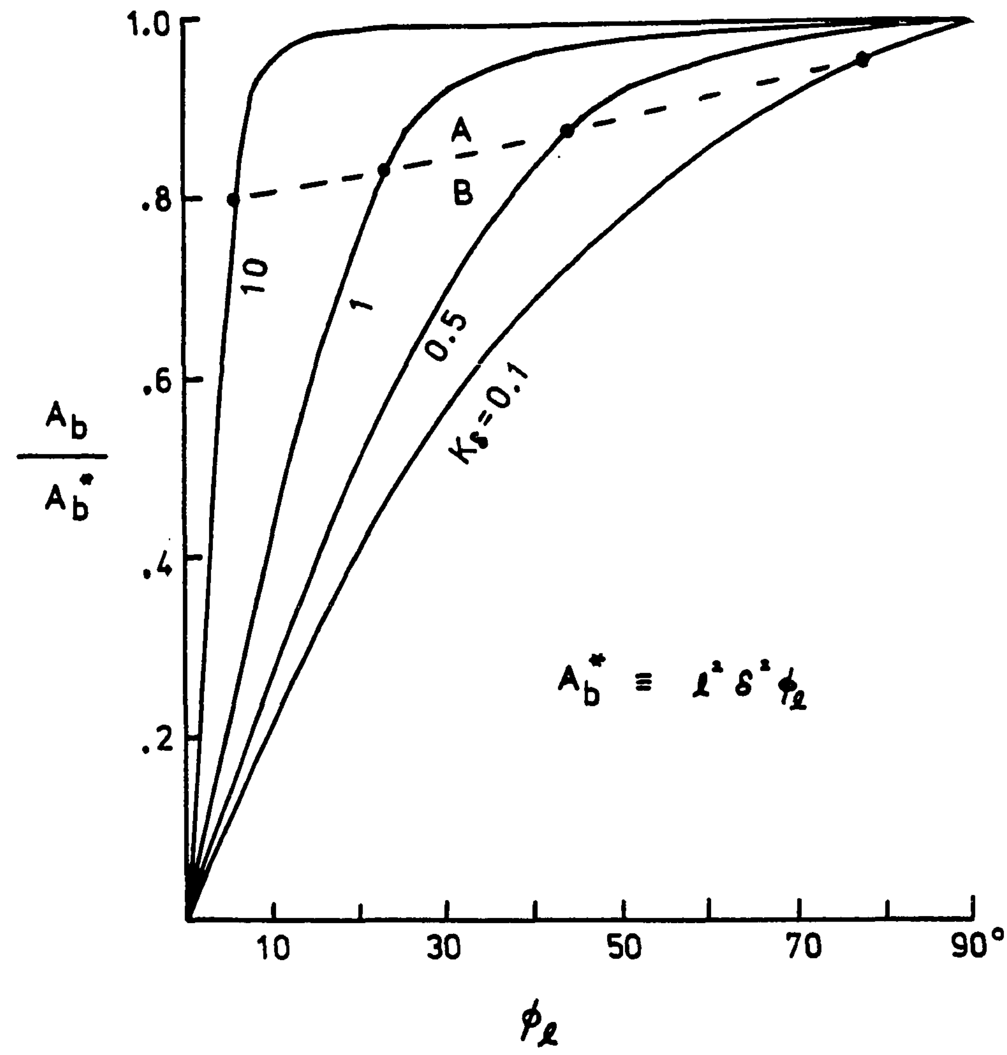

Fig. 4.7 Base Area of Semi-Optimized Waverider as a Function of Dihedral Angle.

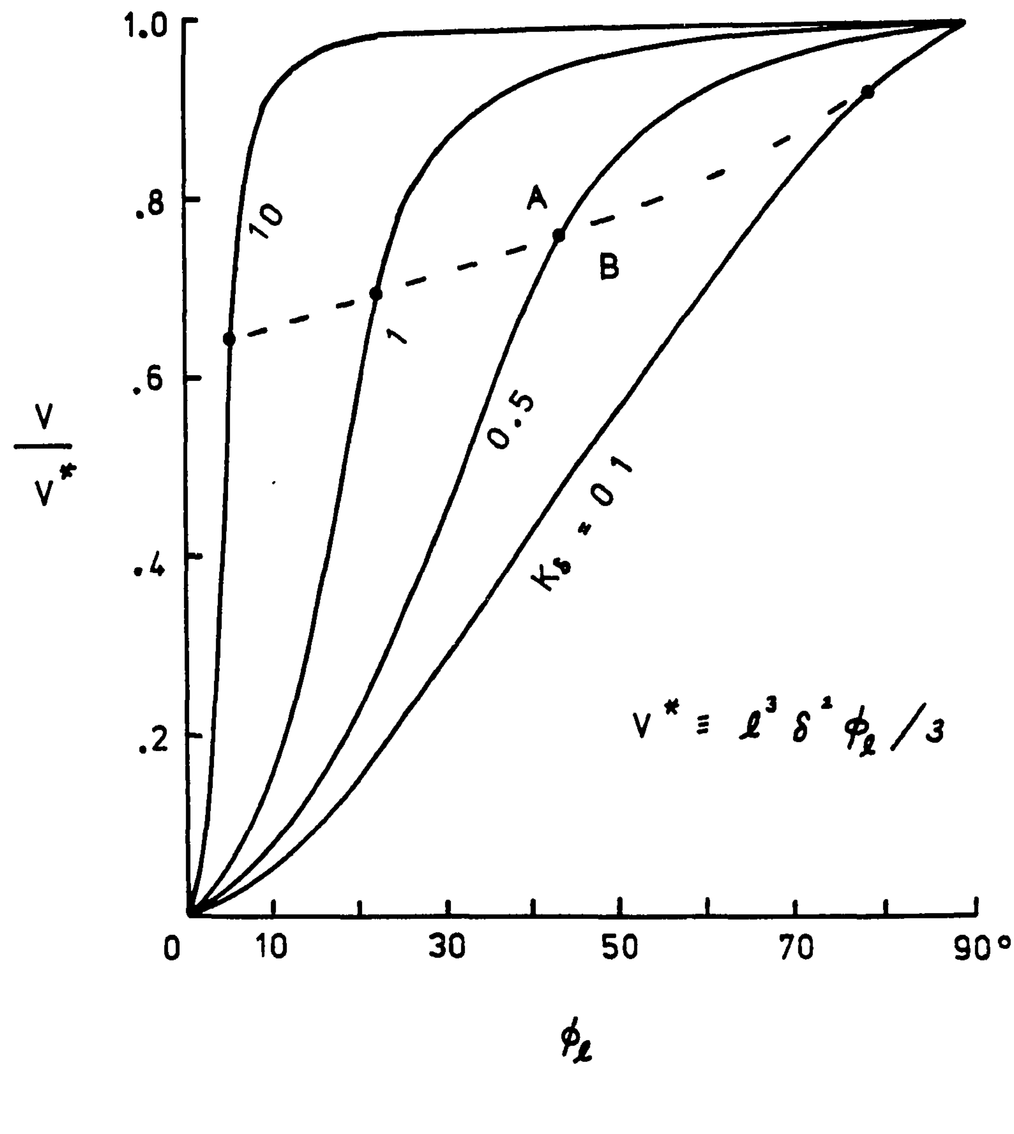

Fig. 4.8 Volume of Semi-Optimized Waverider as a Function of Dihedral Angle.

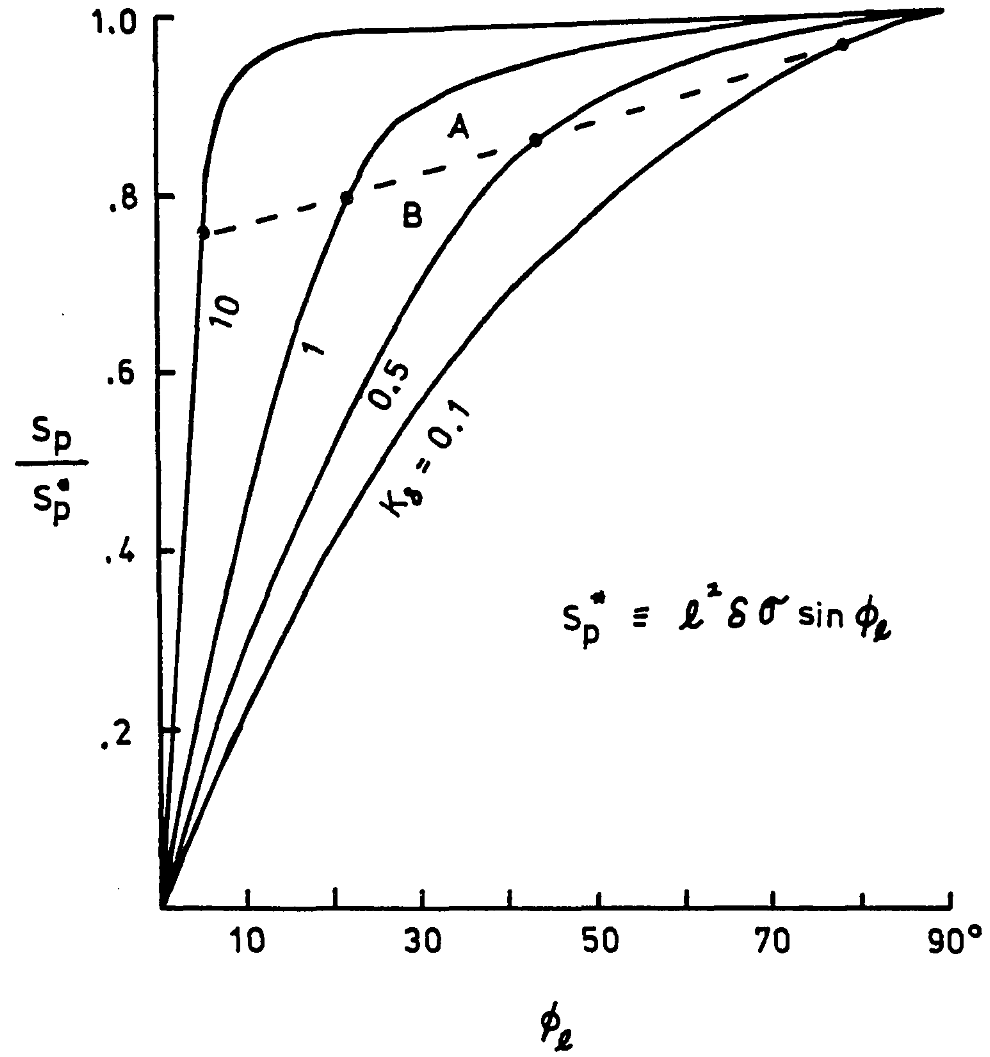

Fig. 4.9 Projected Planform Area of Semi-Optimized Waverider as a Function of Dihedral Angle.

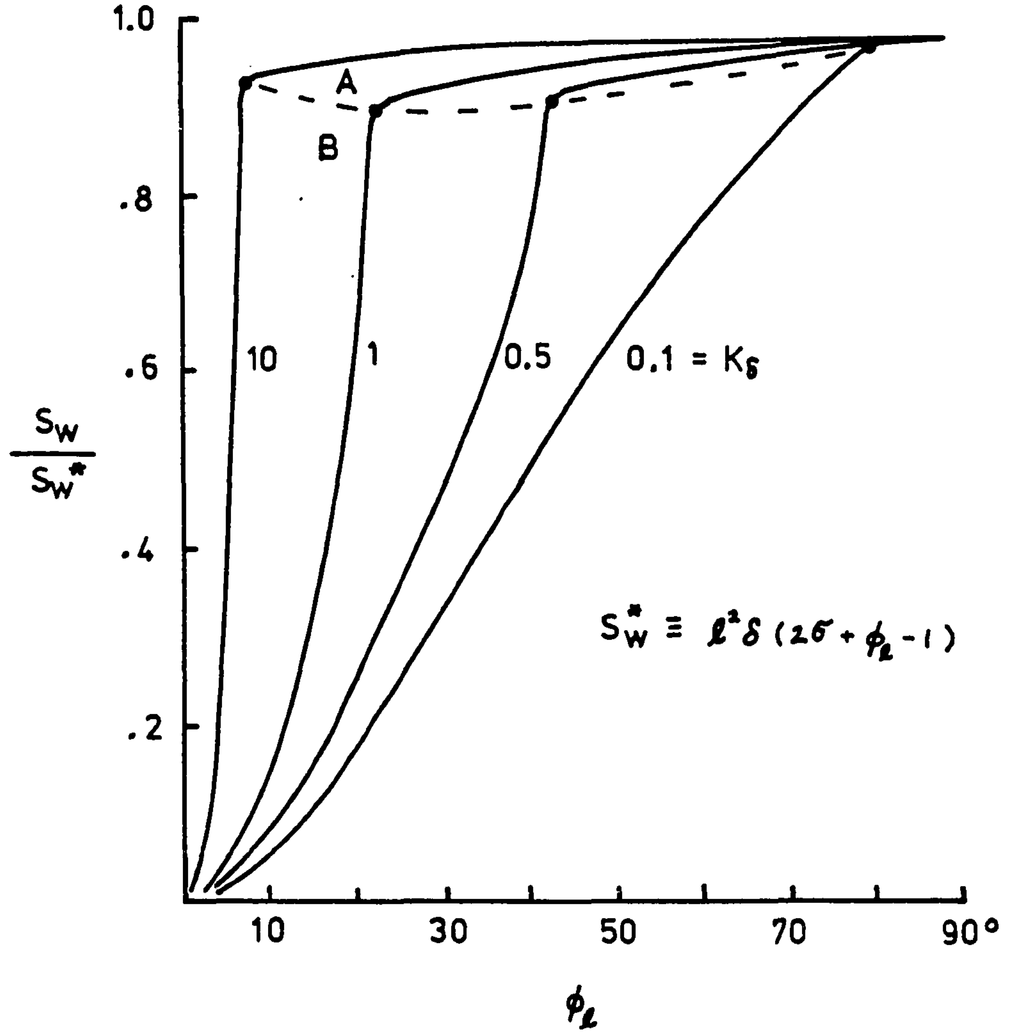

Fig. 4.10 Wetted Area of Semi-Optimized Waverider as a Function of Dihedral Angle.

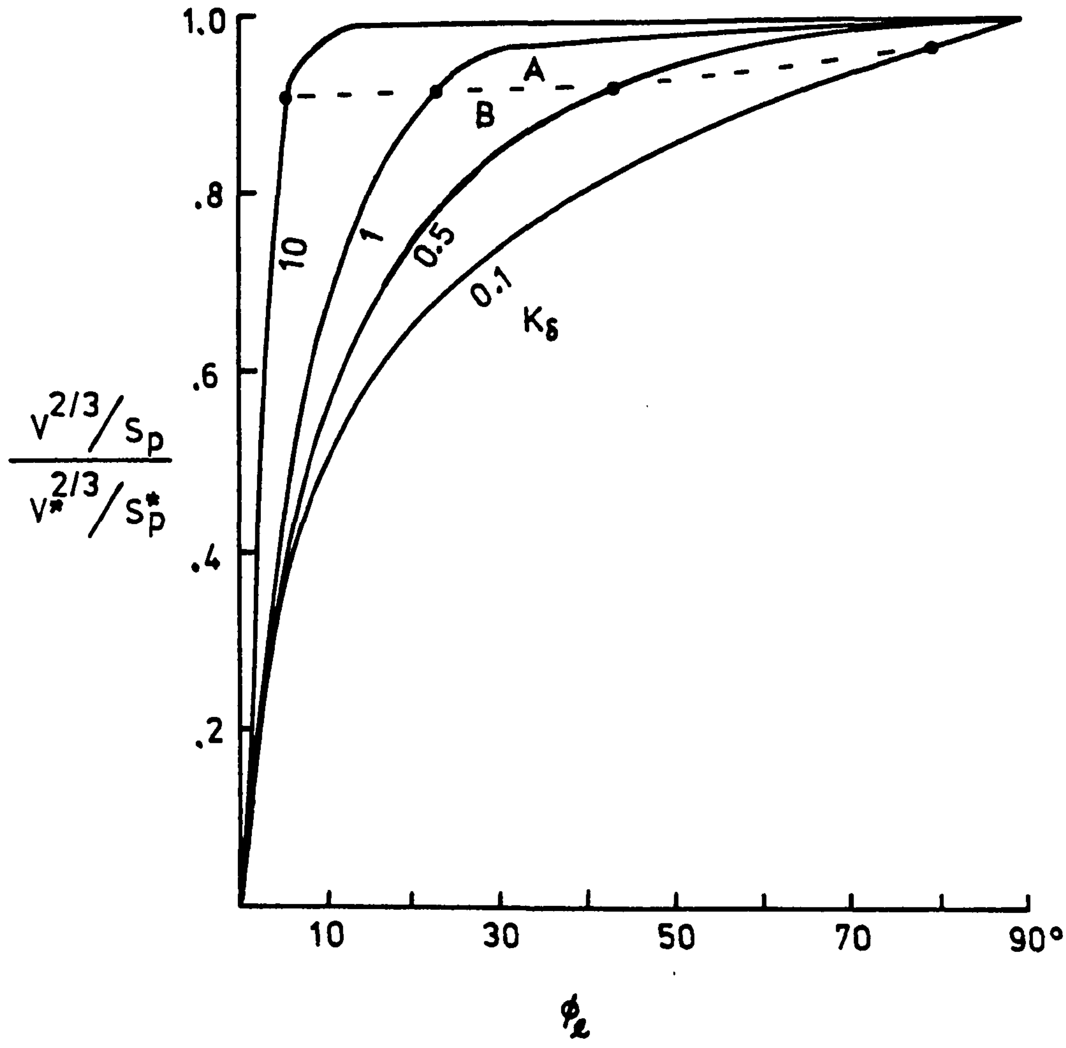

Fig. 4.11 Volume Ratio for Semi-Optimized Waverider as a Function of Dihedral Angle.

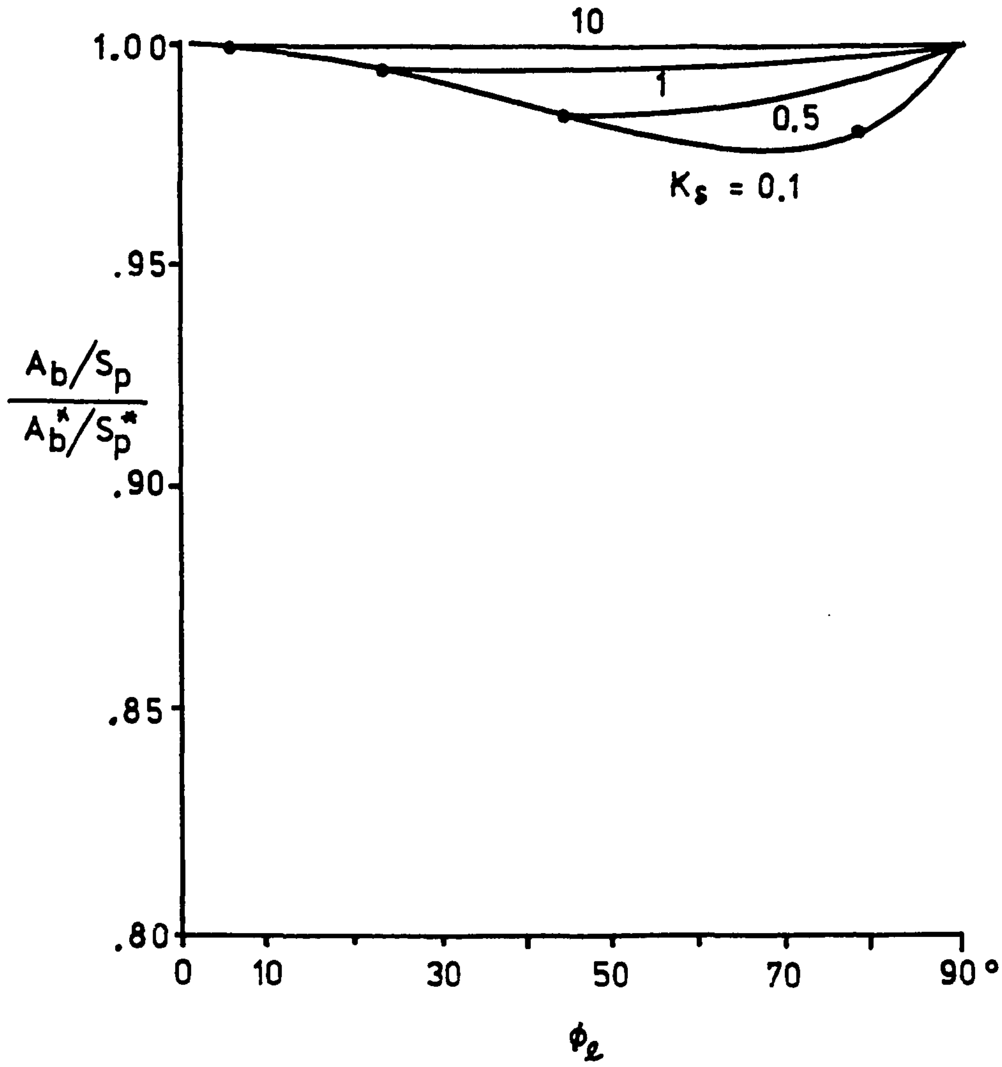

Fig. 4.12 Effective Slenderness Ratio for Semi-Optimized Waverider as a Function of Dihedral Angle.

in Eq. (4.15) into Eq. (4.12), we have lift and drag for class A as

$$L = 4q\ell^2\delta^3 \frac{\sigma^3}{\sigma^2-1}\Big[\sin\phi_\ell - \frac{\sin\phi_\delta}{\sigma} - \frac{1}{4\cos\phi_\ell}\{2(\phi_\ell-\phi_\delta)$$

$$+ \sin2\phi_\ell - \sin2\phi_\delta - \sin^2\phi_\ell(\pi-2\psi-\sin2\psi)\}\Big] \ , \qquad (4.31a)$$

$$D = q\ell^2\delta^4 \frac{\sigma^2}{\sigma^2-1}\Big[\Big(\frac{\sigma^2-1}{\sigma^2} + \ln\sigma^2\Big)\ \phi_\delta + \frac{1}{2\cos^2\phi\ell}\{(4\cos^2\phi_\ell-2)(\phi_\ell-\phi_\delta)$$

$$- \sin2\phi_\ell + \sin2\phi_\delta + \sin^2\phi_\ell\ (\pi-2\psi-\sin2\psi)\}$$

$$-2\int_{\phi_\delta}^{\phi_\ell} \ln\Big(\frac{\cos\phi}{\cos\phi_\ell} - \sqrt{\frac{\cos^2\phi}{\cos^2\phi_\ell} - 1}\Big)d\phi\Big] \ , \qquad (4.31b)$$

where $\psi = \sin^{-1}(\sin^2\phi_\delta/\sin^2\phi_\ell)$ and the integral part in Eq. (4.31b) should be carried out numerically.

The lift and drag of the class B configurations are obtained by using Eq. (4.1) and Eq. (4.9) as

$$L = 2q\ell^2\delta^3 \frac{\sigma^3}{\sigma^2-1}\Big(\sin\phi_\ell - \frac{\phi_\ell}{\cos\phi_\ell} + \frac{\pi}{2}\frac{\sin^2\phi_\ell}{\cos\phi_\ell}\Big) \ , \qquad (4.32a)$$

$$D = 4q\ell^2\delta^4 \frac{\sigma^2}{\sigma^2-1}\Big[\frac{1}{8\cos^2\phi\ell}\{(4\cos^2\phi_\ell-2)\phi_\ell - \sin2\phi_\ell \qquad (4.32b)$$

$$+ \pi\sin^2\phi_\ell\} - \frac{1}{2}\int_0^{\phi_\ell} \ln\Big(\frac{\cos\phi}{\cos\phi_\ell} - \sqrt{\frac{\cos^2\phi}{\cos^2\phi_\ell} - 1}\Big)d\phi\Big] \ .$$

The lift and drag of the semi-optimized configurations are plotted in Fig. 4.13 in forms of $D/q\ell^2\delta^4\sigma$ and $L/q\ell^2\delta^3\sigma$ with K_δ used as a parameter. The origin of the curves corresponds to $\phi_\ell = 0°$ and the end of the curves corresponds to $\phi_\ell = 90°$. The solid-circle point presents $\phi_{\ell c}$ of each K_δ. For a given lift when q, ℓ, δ is fixed, the drag for the non-optimized configuration is always greater than the semi-optimized configurations as shown in Fig. 4.14 and Fig. 4.15 for two cases of non-optimized configurations.

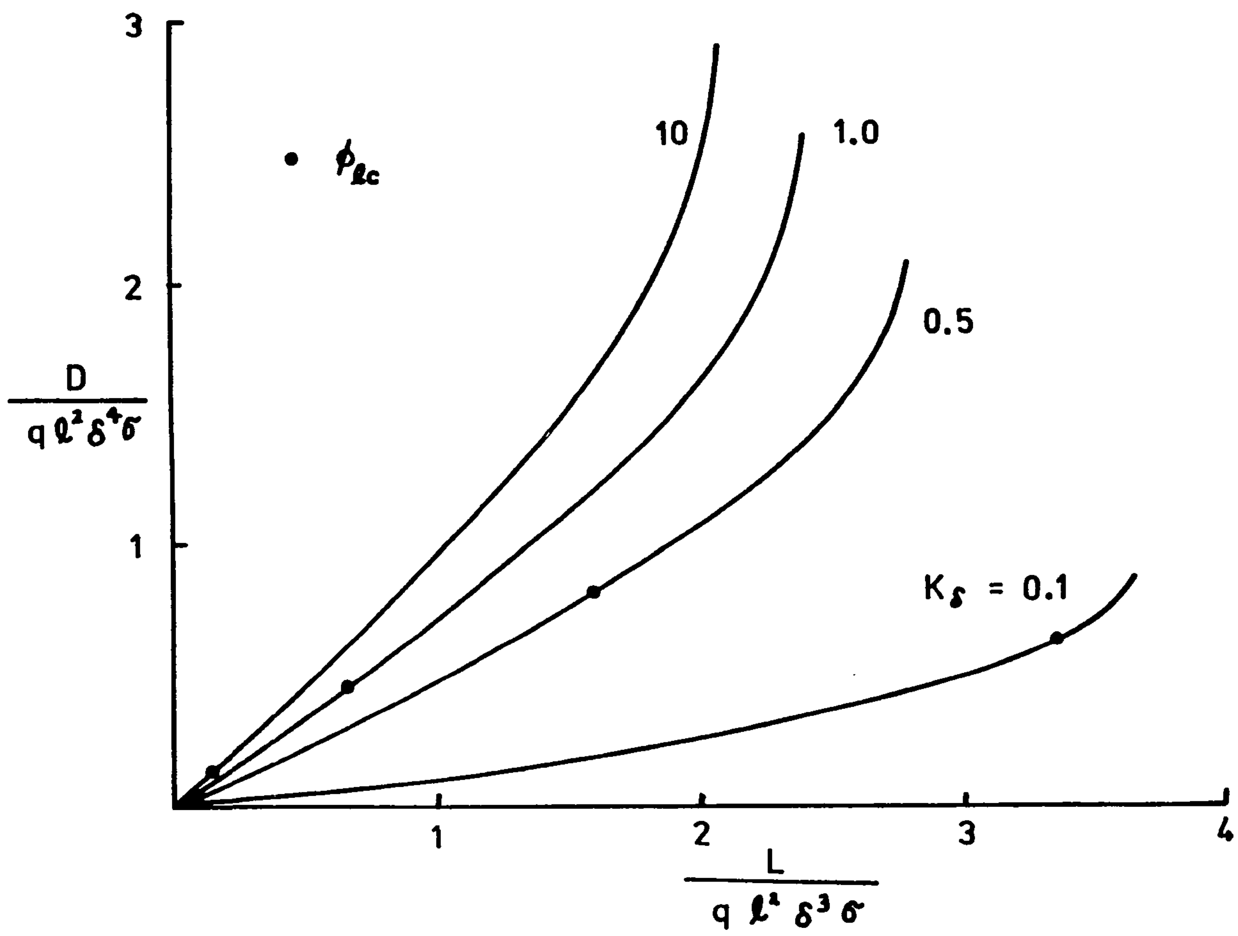

Fig. 4.13 Drag as a Function of Lift for Semi-Optimized Waveriders.

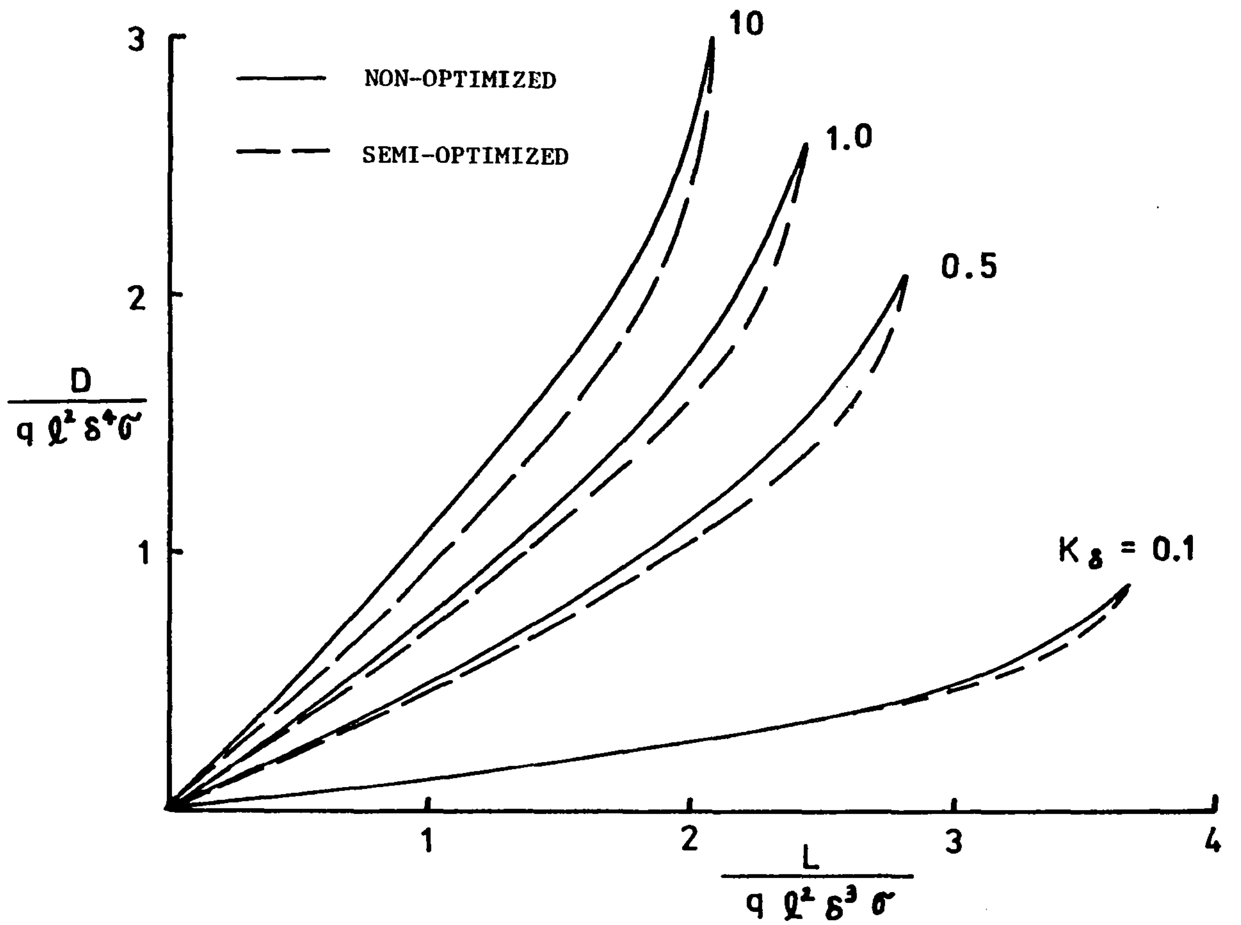

Fig. 4.14 Drag as a Function of Lift for Non-Optimized Waverider with Flat Top Free Stream Surface.

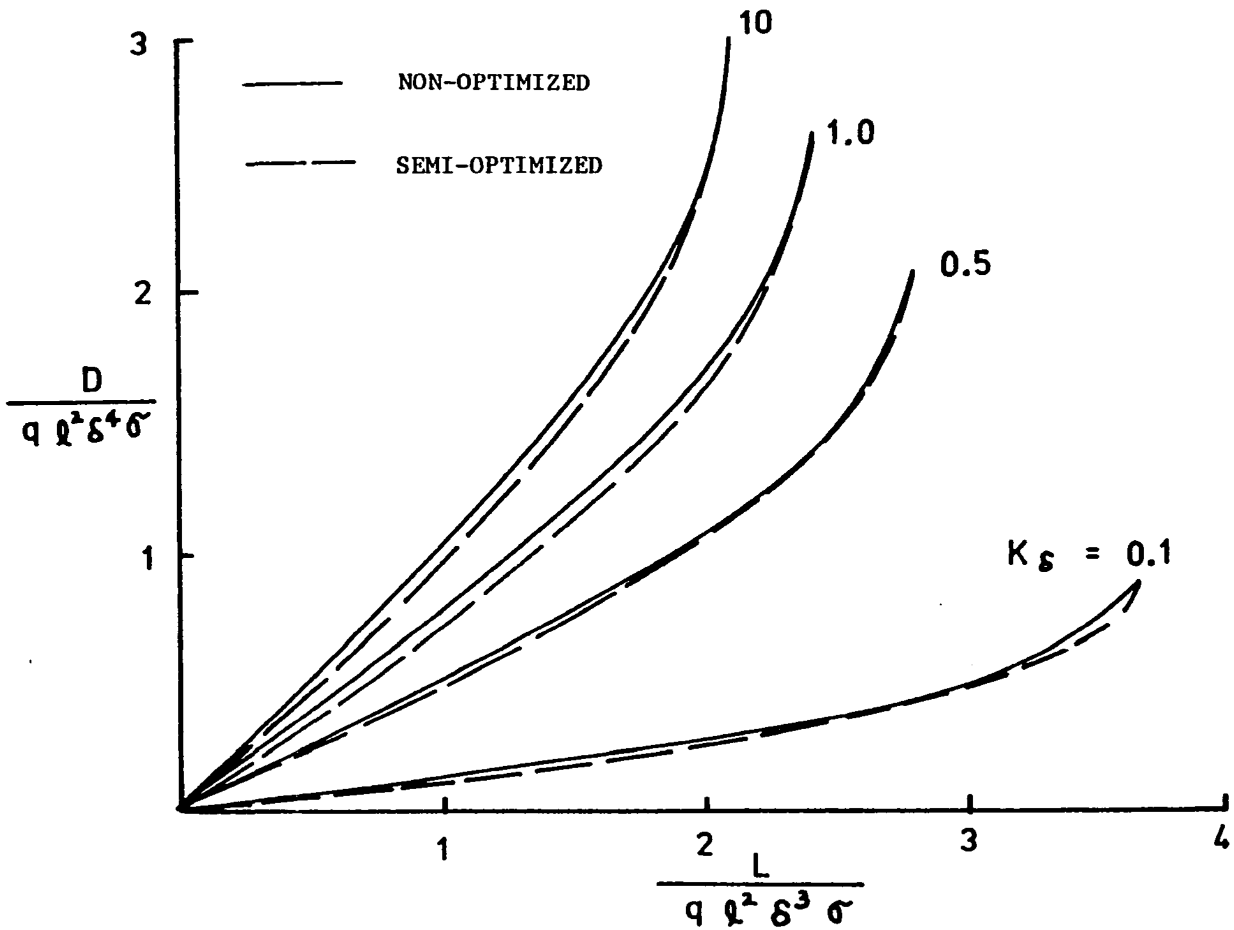

Fig. 4.15 Drag as a Function of Lift for Non-Optimized Waverider of Eq. (4.26).

Fig. 4.16 shows the ratio $(L\delta)/(D\sigma)$ as a function of ϕ_ℓ for various values of K_δ for the semi-optimized configurations. All curves for various K_δ stem from a common curve, the point of tangential departure being $\phi_{\ell c}$. The ratio $(L\delta)/(D\sigma)$ increases as K_δ increases. The dashed curves are for the idealized cone waverider for $K_\delta = 0.1$ and 0.5 for comparison. The lift and drag of the idealized cone waveriders can be obtained by setting $R(\phi) = 1$ in the integrals in Eq. (4.1) and results are

$$L = q\ell^2\delta^3 \left(\frac{4\sigma^2}{\sigma+1}\right) \sin\phi_\ell \quad , \tag{4.33a}$$

$$D = q\ell^2\delta^4 \left(1 + \frac{\sigma^2}{\sigma^2-1} \ln \sigma^2\right) \phi_\ell \quad . \tag{4.33b}$$

The values of $(L\delta)/(D\sigma)$ for the idealized cone waverider gives smaller values than the corresponding semi-optimized shapes for $K_\delta = 0.1$ and 0.5, as should be expected, but for larger K_δ, the idealized cone waverider gives a better approximation being nearly indistinguishable from the semi-optimized configurations at $K_\delta = \infty$. For given value of K_δ, the class B configurations have larger values of $(L\delta)/(D\sigma)$ than class A.

4.4 Fully-Optimized Configurations

When $\partial H/\partial\delta = 0$ in Eq. (3.7) enforced, the semi-optimized shapes are restricted by a relation between ϕ_ℓ and K_δ. Since other variables q and ℓ are independent on δ, performing the differentiation of the functional H with respect to δ leads

$$\frac{\partial}{\partial\delta}\left(\frac{\delta^4\sigma^2}{\sigma^2-1} I_d + \lambda \frac{4\delta^3\sigma^3}{\sigma^2-1} I_\ell\right) = 0 \quad . \tag{4.34}$$

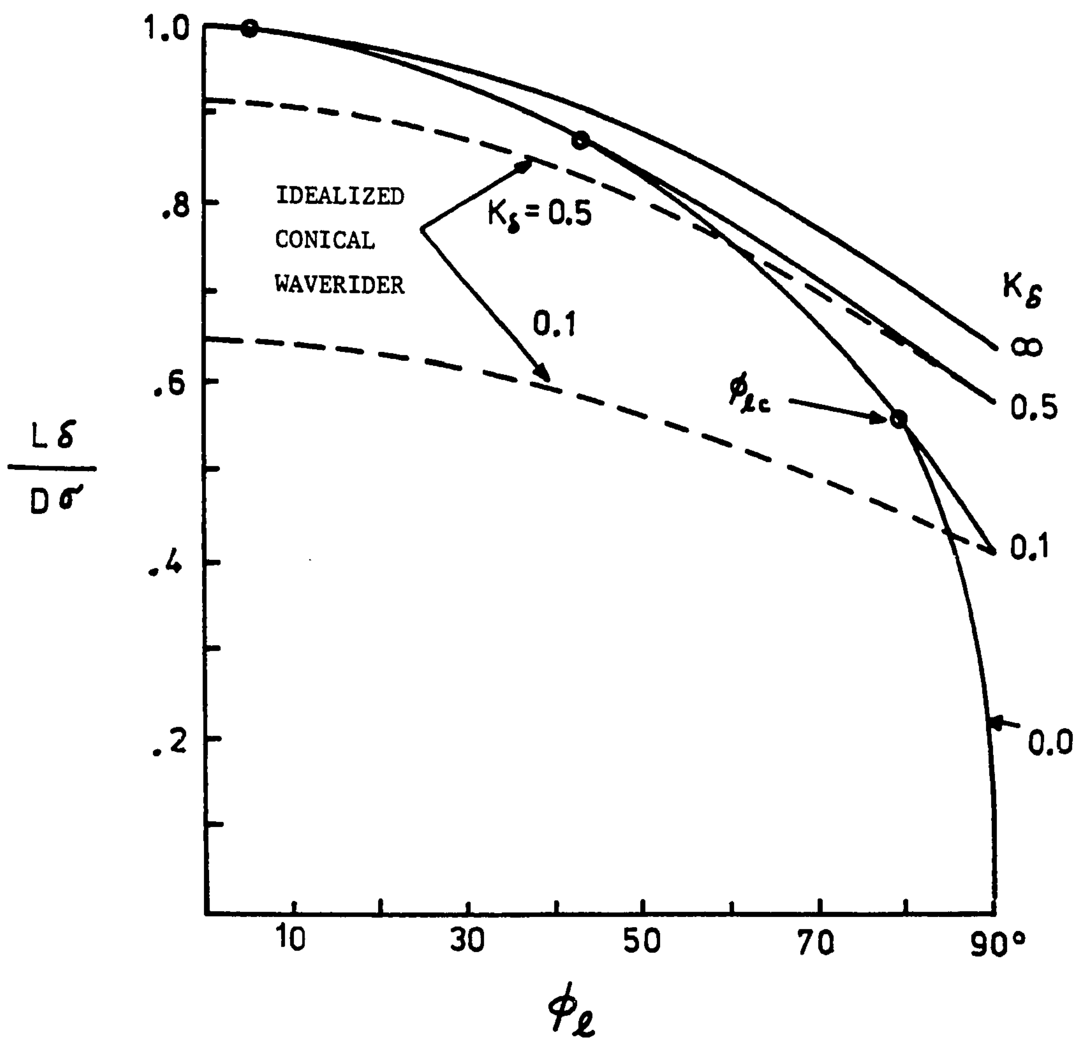

Fig. 4.16 Lift-to-Drag Ratio as a Function of Dihedral Angle for Semi-Optimized Waverider.

Using the relations

$$\frac{\partial\sigma}{\partial\delta} = -\frac{1}{K_\delta 2\sigma\delta} \tag{4.35}$$

and

$$\frac{\partial I_\ell}{\partial\delta} = \begin{cases} 0 & , \quad \text{class A} \\ \dfrac{\sin\phi\delta}{\sigma^2} & , \quad \text{class B} \end{cases} \tag{4.36}$$

$$\frac{\partial I_d}{\partial\delta} = \begin{cases} 0 & , \quad \text{class A} \\ \dfrac{2(1+\sigma^2)}{\sigma^3}\,\phi\delta & , \quad \text{class B} \end{cases} \tag{4.37}$$

and accounting $\lambda = -\delta/(\sigma\cos\phi_\ell)$ leads to the equation

$$\frac{4}{\cos\phi_\ell}\,\frac{I_\ell}{I_d} = \frac{4\sigma^2 k_\delta{}^2 + 2/(\sigma-1) - \dfrac{\sigma}{I_d}\dfrac{\partial I_d}{\partial\sigma}}{3\sigma^2 K_\delta{}^2 - (\sigma^2-3)/(\sigma^2-1) - \dfrac{\sigma}{I_\ell}\dfrac{\partial I_\ell}{\partial\sigma}} \tag{4.38}$$

For class A bodies, the integrals I_ℓ and I_d depend both on ϕ_ℓ and σ, where as for the class B bodies, they depend only on ϕ_ℓ. The relation between ϕ_ℓ and K_δ generated by Eq. (4.38) is shown in Fig. 4.17 with $\phi_{\ell c}$. For small K_δ, the fully-optimized lift-fixed bodies are of class B, and $\phi_{\ell 0} \to 72.3°$ as $K_\delta \to 0$. As K_δ increases above $K_\delta = 0.17$, the fully-optimized bodies are of class A and $\phi_{\ell 0} \to 49°$ as $K_\delta \to \infty$. This asymptotic hypersonic limit result is in very close agreement with numerical result of Cole and Zien [15] for $K_\delta = \infty$.

Fully-optimized values of $(L\delta)/(D\sigma)$ are shown in Fig. 4.18 as a functionof K_δ, together with the corresponding fully-optimized results for the idealized cone waverider [21]. For larger values of K_δ, the two results become closer. Note that since σ becomes larger as K_δ becomes smaller, the actual value of $L\delta/D$ tends to increase as K_δ becomes smaller. The circle shows the location which separates the

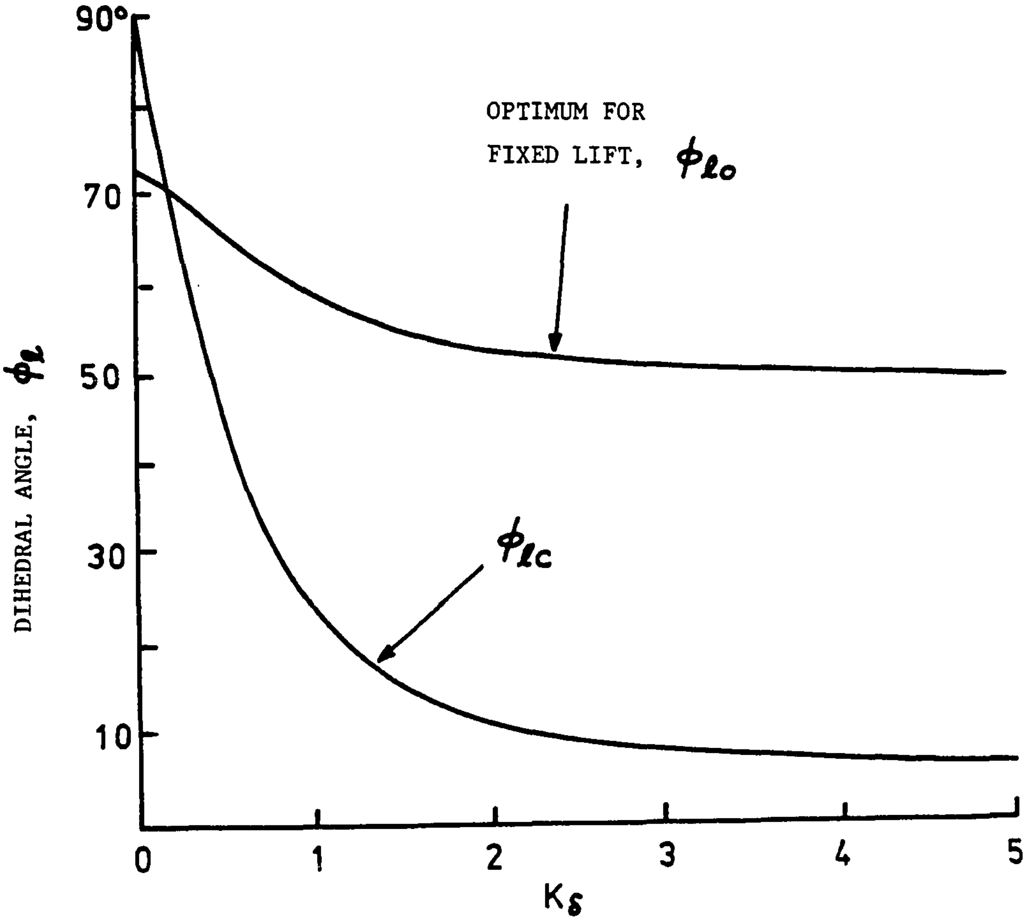

Fig. 4.17 Dihedral Angle for Fully-Optimized Waveriders.

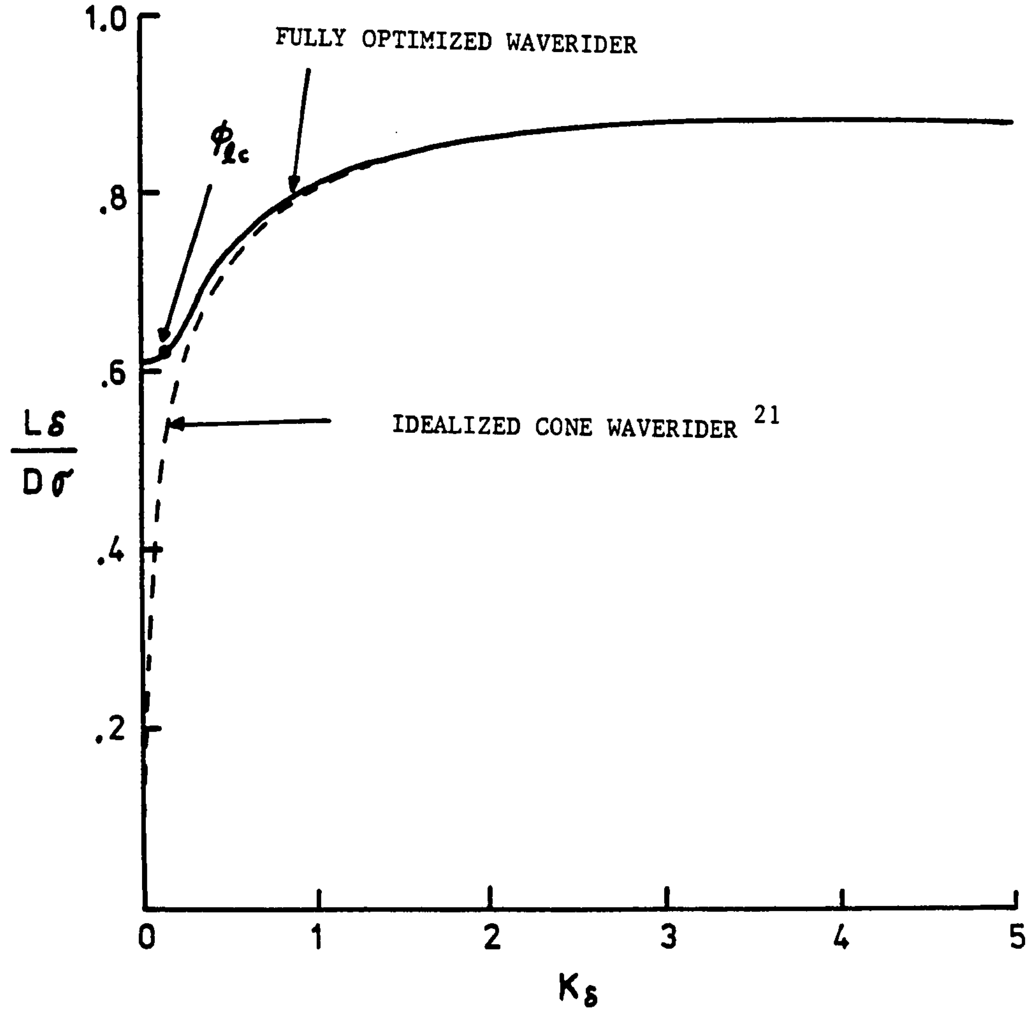

Fig. 4.18 Lift-to-Drag Ratio as a Function for K_δ for Fully-Optimized Waveriders.

class B (small K_δ) from the class A (large K_δ) configurations.

Fig. 4.19 shows the actual values of L/D for the fully-optimized waveriders as a function of δ for $M_\infty = 3, 4, 5$ and 6. All these curves represent the class A configurations since the class B correspond to large values of L/D and small δ thus off the scale of Fig. 4.19. For a fixed δ, the values of L/D decrease as M_∞ increases. the solid circle data point represents the on-design elliptic cone waverider of Ref. 18, ($M_\infty = 4$, $\delta = 18.6°$), which is slightly under the curve for $M_\infty = 4$ for the fully-optimized waverider. The square data point represents the conical lifting body of Schindel [19] ($M_\infty = 6$, $\delta = 13°$), which produces less L/D than the fully-optimized waveriders. The experimental results include the friction drag on the forebody whereas the theory ignores friction drag.

Fig. 4.20 shows L/D for the fully-optimized waveriders as a function of $V^{2/3}/S_p$ for $M_\infty = 3, 4,$ and 5. For a fixed $V^{2/3}/S_p$ the L/D increases as M_∞ increases. Fig. 4.21 shows L/D for the fully-optimized waveriders as a function of A_b/S_p for $M_\infty = 3,5$. For large mach numbers, this representation is nearly independent of M_∞. The curves in both Fig. 4.20 and Fig. 4.21 represent only the class A configurations since the results for the class B are off scale (large L/D). The solid circle data point in both figures represents the on-design elliptic cone waverider of Ref. 18 and it falls slightly under the curves for the present optimized waveriders. The square data point in both figures represents the experimental maximum L/D (at $M_\infty = 6$) for the lifting body of Schindel [19] which falls below the curves for the present optimized waveriders. The shaped trapezoidal area represents the

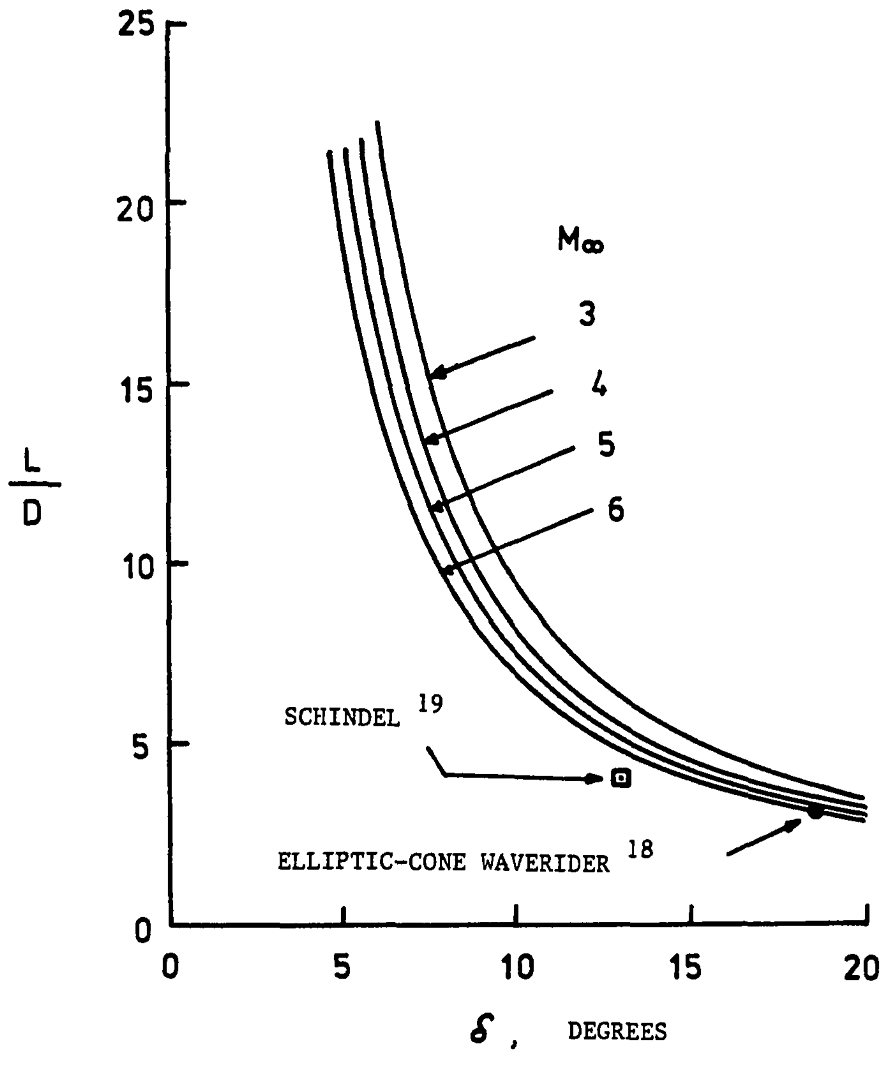

Fig. 4.19 Lift-to-Drag Ratio as a Function of Cone Angle for Fully-Optimized Waverider.

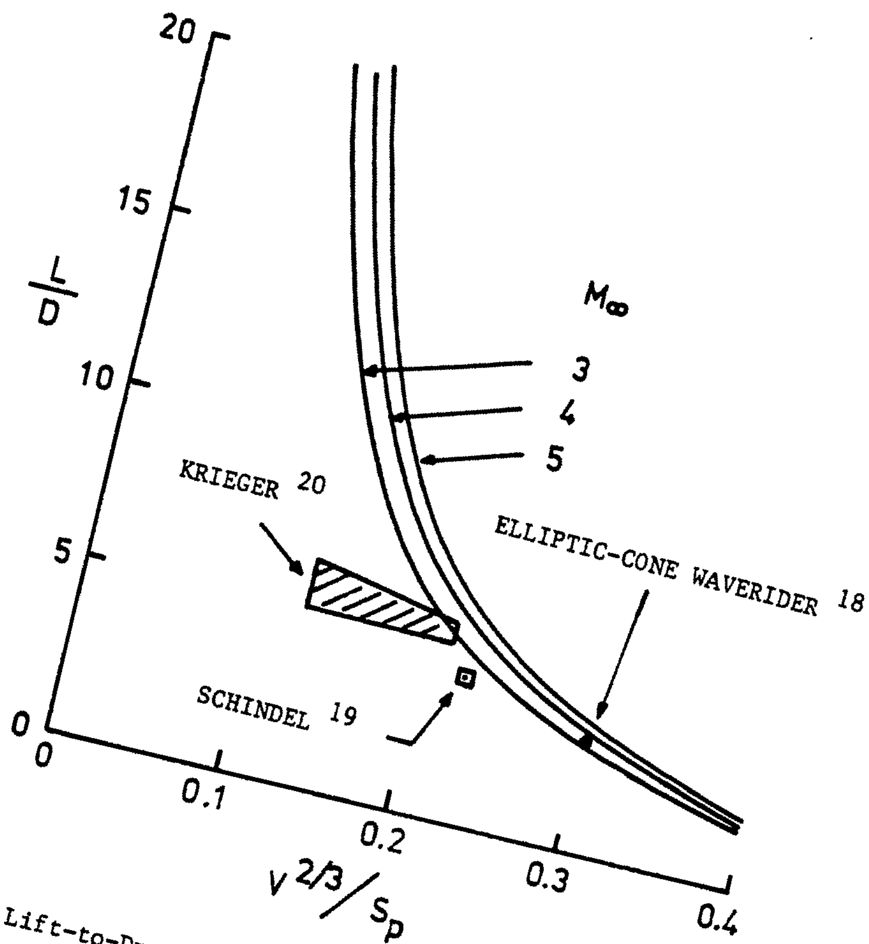

Fig. 4.20 Lift-to-Drag Ratio of Fully-Optimized Waverider as a Function of Volume Ratio.

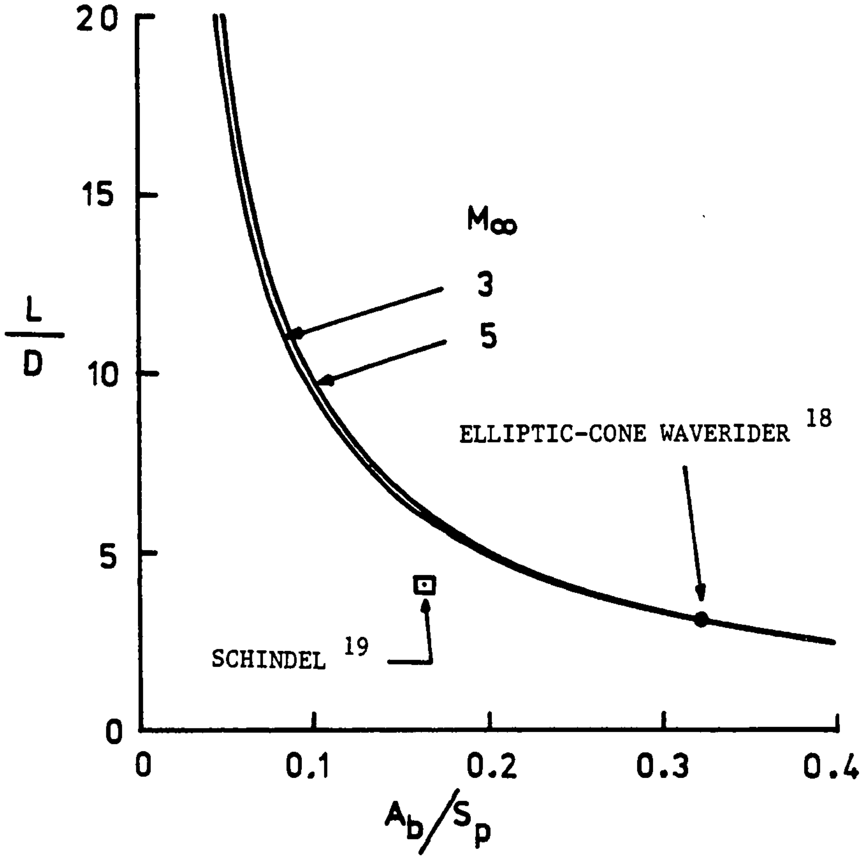

Fig. 4.21 Lift-to-Drag Ratio of Fully-Optimized Waverider as a Function of Slenderness Ratio.

data range of "aerodynamic configured" missiles discussed by Krieger [20], which also have less L/D than the present optimized waveriders except in the low Mach number range. The results of Krieger as a function of A_b/S_p were not available.

Since experimental results include friction drag, it is reasonable to calculate friction drag of the forebody of the present optimized waverider and compare with the experimental results. The viscous or friction drag for the fore body of a waverider can be represented by $D_f = q\ S_w\ C_f$ where S_w is the wetted area of the body, given by Eq. (4.29), and C_f is an appropriately averaged coefficient of friction. The drag can now be written as $D_w + D_f$ where D_w is the drag used previously.

The value of C_f must be estimated for a given configuration and range of flight conditions. It depends on Reynolds number, Mach number, laminar or turbulent flow, transition, wall heating, and effects of corner flow. For laminar flow on a flat plate, C_f is approximated by $C_f = 1.328\ f(M_\infty)/\sqrt{Re}$, where $Re = \rho_\infty V_\infty \ell/\mu_\infty$ is the free stream Reynolds number based on the length, and $f(M_\infty)$ is a function of Mach number depending on the nature of the viscousity-temperature relation, being somewhat less than unity. Based on expressions such as this, modified for conical flow and turbulence, possible values of C_f of interest were taken to lie in the range $0.001 < C_f < 0.003$.

Fig. 4.22 is a redrawing of Fig. 4.20 for $M_\infty = 4$ showing the effect of friction drag. The figure shows that friction drag becomes more significant when the body is more slender, that is, the smaller that δ, V/S_p, and A_b/S_p become. It can be seen that there is another

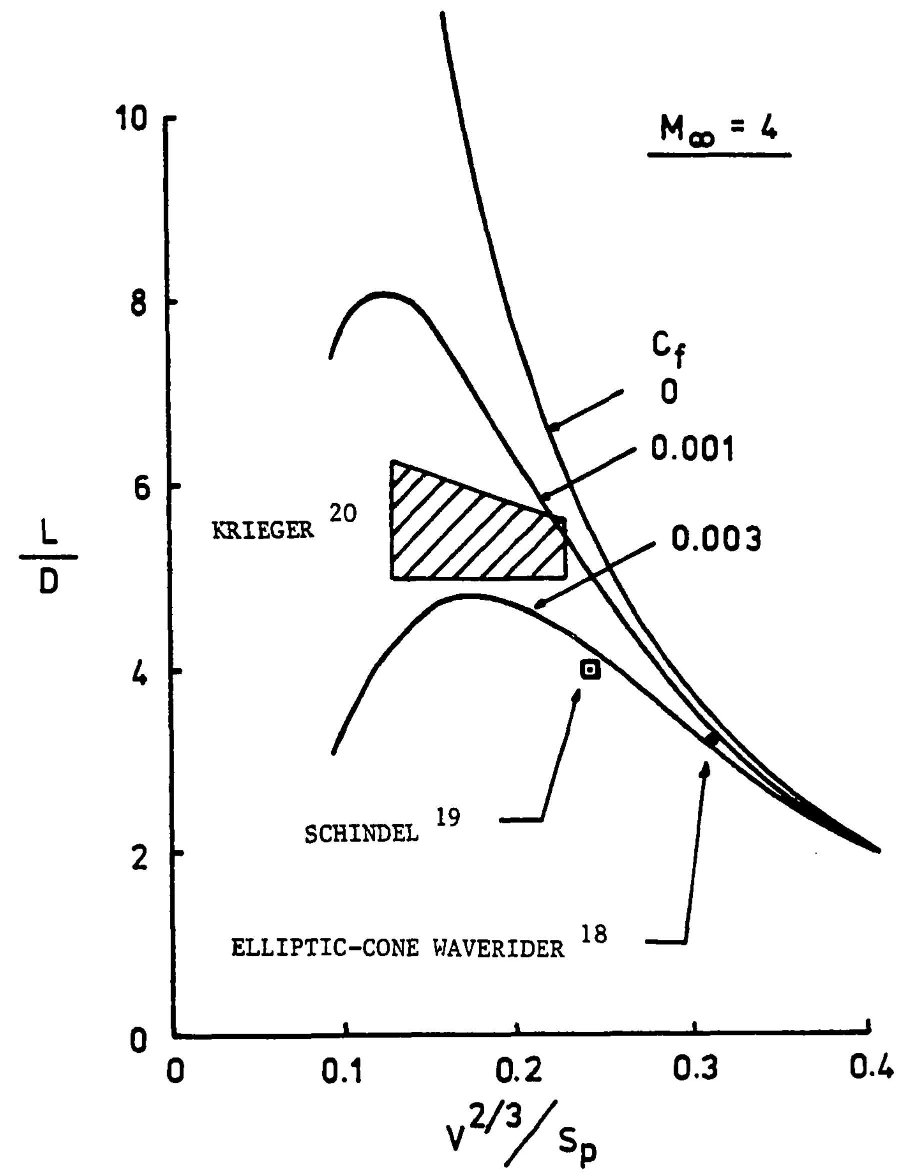

Fig. 4.22 Lift-to-Drag Ratio of Fully-Optimized Waverider as a Function of Volume Ratio.

optimum for L/D that involves the friction drag, since the curves for for nonzero values of C_f shows maximum values. The experimental results all contain friction drag, and only the curve for $C_f = 0$ is frictionless.

SECTION V

WAVERIDER CONFIGURATIONS OF N =1 CASE

The body and shock expressions in Eq. (2.9) and Eq. (2.10) can be written for n = 1 case as

$$\theta_{body} = \delta(1 + E_1 \cos\phi) \tag{5.1}$$

$$\theta_{shock} = \delta(\sigma + E_1 g_1 \cos\phi) \tag{5.2}$$

in spherical coordinate system when $E_1 = \varepsilon_1/\delta$ is a small parameter and δ and β are semi-vertex angle of body and shock respectively of a circular cone. Since Eq. (5.1) describes a circular cone body with angle of attack within error of $O(E_1{}^2)$, the optimization problem of n = 1 case is to obtain optimum configurations from flow past an inclined cone.

The lift and drag in Eq. (2.26) and Eq. (2.27) for n = 1 case are written as

$$L = 4q\ell^2\delta^3 \frac{\sigma^2}{\sigma^2-1} \int_0^{\phi_\ell} F_\ell \;(R(\phi),\ \phi;\ \sigma, E_1)d\phi \tag{5.3}$$

$$D = 4q\ell^2\delta^4 \frac{\sigma^2}{\sigma^2-1} \int_0^{\phi_\ell} F_d \;(R(\phi),\ \phi;\ \sigma, E_1)d\phi \tag{5.4}$$

where

$$F_\ell = \{\sigma-R(\phi)\}\cos\phi + E_1 \int_{R(\phi)}^{\sigma} \xi\{V_1(\xi) \cos^2\phi - W_1(\xi)\sin^2\phi\}d\xi + E_1 g_1 \cos^2\phi \tag{5.5}$$

$$F_d = \frac{\sigma^2 - R^2(\phi)}{4\sigma^2} - \frac{1}{2}\,\ell n\,\frac{R(\phi)}{\sigma} + E_1 \int_{R(\phi)}^{\sigma} \{V_1(\xi) + \xi F_1\} \cos\phi d\xi + \frac{E_1 g_1}{\sigma}\cos\phi \tag{5.6}$$

where $R(\phi)$ is the trailing edge function of the compression stream surface and is to be determined in following sections.

5.1 Semi-Optimized Configurations

When other parameters q, ℓ, and M_∞ are fixed, following the same procedure outlined in the previous chapters, the variational problem of minimizing drag with fixed lift reduces the problem to that of minimizing functional

$$H = D + \lambda L$$

where L and D are given in Eq. (5.3) and (5.4), and λ is a Lagrange multiplier.

After taking variations of H with respect to $R(\phi)$ we get the Euler-Lagrange equation as

$$\frac{R^2+\sigma^2}{2R\sigma^2} + E_1(V_1(R) + RF_1)\cos\phi + \frac{\lambda}{\delta}\{\cos\phi + E_1 R(V_1(R)\cos^2\phi - W_1(R)\sin^2\phi)\} = 0 \tag{5.8}$$

and the transversality condition as

$$\left[F_d + \frac{\lambda}{\delta} F_\ell\right]_{\phi=\phi_\ell} = 0 \quad . \tag{5.9}$$

The λ/δ term can be replaced after applying the boundary condition

$$R(\phi_\ell) = \sigma \tag{5.10}$$

to Eq. (5.8) and the result is

$$\bar{\lambda} \equiv \frac{\lambda}{\delta} = -\frac{1/\sigma + E_1(V_1(\sigma) + \sigma F_1)\cos\phi_\ell}{\cos\phi_\ell + E_1\sigma(V_1(\sigma)\cos^2\phi_\ell - w_1(\sigma)\sin^2\phi_\ell)} \qquad (5.11)$$

With the values

$$V_1(\sigma) = \frac{4}{\gamma+1} g_1 \quad , \quad W_1(\sigma) = \frac{g_1}{\sigma^2} \quad , \quad F_1 = \frac{g_1}{\sigma^3}$$

Eq. (5.11) yields

$$\bar{\lambda} = -\frac{1 + E_1 g_1 \sigma\left(\frac{4}{\gamma+1} + \frac{1}{\sigma^2}\right)}{\sigma\cos\phi_\ell + E_1 g_1 \sigma^2\left(\frac{4}{\gamma+1}\cos^2\phi_\ell - \frac{1}{\sigma^2}\sin^2\phi_\ell\right)} \qquad (5.12)$$

Notice that $E_1 = 0$ case of Eq. (5.11) leads to

$$\lambda = -\frac{\delta}{\sigma\cos\phi_\ell}$$

which is the same result as Eq. (4.5) for $E_1 = 0$ case.

If the denominator of Eq. (5.12) becomes zero, the value of $\bar{\lambda}$ becomes infinity. We can get approximate value of ϕ_ℓ where $\bar{\lambda}\to\infty$ by setting the denomenator equal to zero,

$$E_1 g_1\left(\frac{4\sigma^2}{\gamma+1} + 1\right)\cos^2\phi_\ell + \sigma\cos\phi_\ell - E_1 g_1 = 0 \qquad (5.13)$$

and the approximate solution is

$$\cos\phi_{\ell m} \cong \frac{E_1 g_1}{\sigma} \qquad (5.14)$$

If ϕ_ℓ is larger than $\phi_{\ell m}$, the lift no longer increases as ϕ_ℓ increases, therefore, we are not interested in the value of ϕ_ℓ which is greater than $\phi_{\ell m}$. The special case value for $\phi_{\ell m}$ is 90° when $E_1 = 0$. Also $\phi_{\ell m}\to 90°$ when $K_\delta \to 0$ since $\sigma\to\infty$ as $K\delta\to 0$.

By using the boundary condition of Eq. (5.10), the transversality condition becomes

$$\frac{E_1 g_1}{\sigma} + \bar{\lambda} E_1 g_1 \cos\phi_\ell = 0 \qquad (5.15)$$

which is automatically satisfied since we can write $\bar{\lambda}$ as

$$\bar{\lambda} = -\frac{1}{\sigma\cos\phi_\ell} + O(E_1)$$

then Eq. (5.15) becomes of order of $O(E_1{}^2)$ which is ignored in our analysis.

The Euler-Lagrange equation, Eq. (5.8), which is a quadratic equation for $\cos(\phi)$ can be written as

$$A(R)\cos^2\phi + B(R)\cos\phi + C(R) = 0 \tag{5.16a}$$

where

$$\begin{aligned} A(R) &= E_1\bar{\lambda}R(V_1(R) + W_1(R)) \quad , \\ B(R) &= \bar{\lambda} + E_1(V_1(R) + RF_1)) \quad , \\ C(R) &= \frac{R^2+\sigma^2}{2R\sigma^2} - E_1\bar{\lambda}\, RW_1(R) \quad , \end{aligned} \tag{5.16b}$$

can be solved easily for $\cos(\phi)$ as

$$\cos\phi = \frac{-B(R) \pm \sqrt{B^2(R) - 4A(R)C(R)}}{2A(R)} \tag{5.17}$$

The solution is an inverse one because the solution for $R(\phi)$ cannot be obtained explicitly.

For $\phi = 0$, if we take a limit $E_1 \to 0$, Eq. (5.15) yields

$$0 = \frac{1}{\sigma\cos\phi_\ell} \pm \frac{1}{\sigma\cos\phi_\ell} \tag{5.18}$$

so the minus sign should be used to satisfy the above equation. Finally, we get the solution as

$$\phi = \cos^{-1}\left[\frac{-B(R) - \sqrt{B^2(R) - 4A(R)C(R)}}{2A(R)}\right] \tag{5.19}$$

The solution to Eq. (5.19) can be obtained by using a different approach. Instead of using an unknown function $R(\phi)$ for the trailing edge of the compression surface, we use an unknown function $\Phi(\xi)$. Then from Eq. (2.22), the lift and drag become

$$L = 4q\ell^2\delta^3 \frac{\sigma^2}{\sigma^2-1} \left[\int_{\xi_0}^{\sigma} \tilde{F}_\ell\ (\Phi,\ \xi;\ \sigma,\ E_1)d\xi + E_1 g_1 \left(\frac{\phi_\ell}{2} + \frac{\sin^2\phi_\ell}{4}\right)\right] \quad ,$$

$$D = 4q\ell^2\delta^4 \frac{\sigma^2}{\sigma^2-1} \left[\int_{\xi_0}^{\sigma} \tilde{F}_d\ (\Phi,\ \xi;\ \sigma,\ E_1)d\xi + \frac{E_1 g_1}{\sigma} \sin^2\phi_\ell\right] \quad , \qquad (5.20)$$

where

$$\tilde{F}_\ell = \sin\Phi(\xi) + E_1\xi V_1(\xi) \left\{\frac{\Phi(\xi)}{2} + \frac{\sin2\Phi(\xi)}{4}\right\} - \varepsilon E_1 W_1(\xi)\left\{\frac{\Phi(\xi)}{2} - \frac{\sin2\Phi(\xi)}{4}\right\} \quad ,$$

$$\tilde{F}_d = \frac{1}{2}\left(\frac{\xi^2+\sigma^2}{2\xi\sigma^2}\right)\Phi(\xi) + E_1(V_1(\xi) + \xi F_1) \sin\Phi(\xi) \quad .$$

Then the Euler-Lagrange equation from $\delta\tilde{H} = 0$ yields

$$A(\xi)\cos^2\Phi(\xi) + B(\xi)\cos\Phi(\xi) + C(\xi) = 0 \qquad (5.21)$$

where $A(\xi)$, $B(\xi)$, and $C(\xi)$ have the forms in Eq. (5.16b) except ξ appears instead of R. The transversality condition for free end point ξ_0 is

$$\left[\tilde{F}_d + \frac{\lambda}{\delta} \tilde{F}_\ell\right]_{\text{at } \xi = \xi_0} = 0 \qquad (5.22)$$

is automatically satisfied since $\Phi(\xi_0) = 0$. Then the solution for $\phi(\xi)$ is

$$\Phi(\xi) = \cos^{-1}\left[\frac{-B(\xi) - \sqrt{B^2(\xi) - 4A(\xi)C(\xi)}}{2A(\xi)}\right] \qquad (5.23)$$

which is the same solution as in Eq. (5.19).

The critical value, $\phi_{\ell c}$, for $n = 1$ case can be obtained by using the condition

$$R(0) = 1 \quad \text{at} \quad \phi_\ell = \phi_{\ell c} \tag{5.24}$$

The value $\bar{\lambda}$ for $\phi_\ell = \phi_{\ell c}$, denoted by $\bar{\lambda}_c$, is obtained by applying the condition Eq. (5.24) to the Lagrange equation, Eq. (5.8) as

$$\bar{\lambda}_c = -\frac{(\sigma^2+1)/2\sigma^2 + E_1(V_1(1) + F_1)}{1 + E_1 V_1(1)} \tag{5.25}$$

Equating above equation with Eq. (5.11) for $\phi_\ell = \phi_{\ell c}$ we have

$$\cos\phi_{\ell c} = \left[\frac{-B^*(\sigma) - \sqrt{B^{*2}(\sigma) - 4A^*(\sigma)C^*(\sigma)}}{2A^*(\sigma)}\right]$$

where $A^*(\sigma)$, $B^*(\sigma)$ and $C^*(\sigma)$ are in forms as Eq. (5.16b) except $\bar{\lambda}_c$ instead of $\bar{\lambda}$. The values of $\bar{\lambda}_c$ is given in Eq. (5.25).

In Fig. 5.1, the values of $\phi_{\ell c}$ are plotted as a function of K_δ for various values of E_1. As E_1 decreases, $\phi_{\ell c}$ decreases for given K_δ value. For certain value of K_δ and E_1, there are only class A configurations available. For example, if $E_1 = -0.05$ and K_δ is greater than 3.0, there is no class B configurations in that range. However, the range is not acceptable since we assumed that the perturbed shock layer base area S_{bn} is much smaller than S_{bo} in Eq. (2.19), in other words, the absolute value of E_1 is much smaller than the thickness of the shock layer, $(\sigma-1)$, which is a function of K_δ. As $K_\delta \to 0$, $\phi_{\ell c} \to 90°$ for all E_1 values and $\phi_{\ell c}$ values for $E_1=0$ case are same as that in Fig. 4.1.

When ϕ_ℓ is greater than $\phi_{\ell c}$, we have class A configurations and the trailing edge of the compression stream surface should be written as

$$\begin{cases} \xi = 1 + E_1 \cos\phi & \text{for } 0 < \phi < \phi_\delta \;, \\ \xi = R(\phi) & \text{for } \phi_\delta < \phi < \phi_\ell \;, \end{cases} \tag{5.27}$$

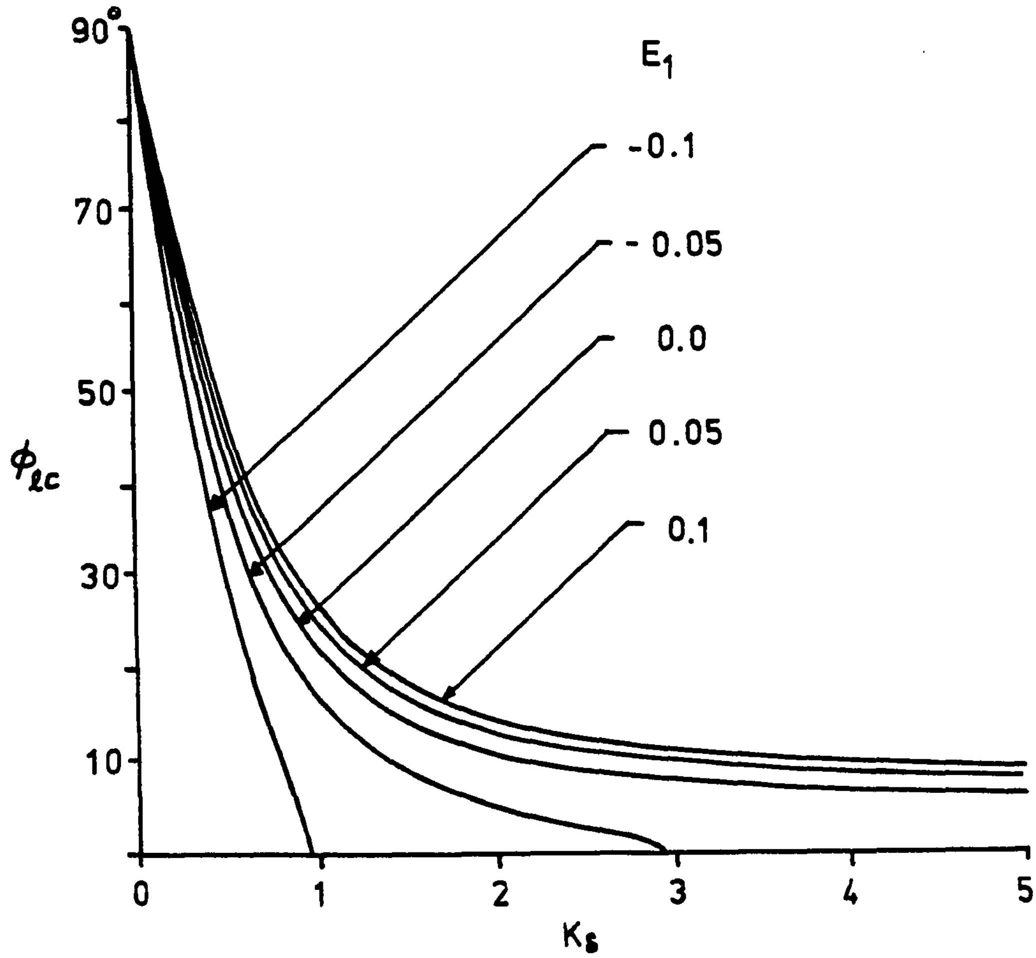

Fig. 5.1 Critical Dihedral Angle for Semi-Optimized Waveriders of n=1 Case.

where ϕ_δ satisfies the condition $R(\phi_\delta) = 1$. Substituting Eq. (5.27) into Eq. (5.3) through Eq. (5.6) and neglecting higher order terms, we can get

$$L = 4q\ell^2\delta^3 \frac{\sigma^2}{\sigma^2-1} \left[\int_0^{\phi_\delta} F_{\ell 1}\, d\phi + \int_{\phi_\delta}^{\phi_\ell} F_{\ell 2}\, d\phi\right] \quad , \tag{5.28}$$

$$D = 4q\ell^2\delta^4 \frac{\sigma^2}{\sigma^2-1} \left[\int_0^{\phi_\delta} F_{d1}\, d\phi + \int_{\phi_\delta}^{\phi_\ell} F_{d2}\, d\phi\right] \quad , \tag{5.29}$$

where

$$F_{\ell 1} = (\sigma-1)\cos\phi + E_1 \int_1^\sigma \xi\{V_1(\xi)\cos^2\phi - W_1(\xi)\sin^2\phi\}\, d\xi + E_1(g_1-1)\cos^2\phi \quad , \tag{5.30a}$$

$$F_{\ell 2} = (\sigma-R)\cos\phi + E_1 \int_R^\sigma \xi\{V_1(\xi)\cos^2\phi - W_1(\xi)\sin^2\phi\}\, d\xi + E_1 g_1\cos^2\phi \quad , \tag{5.30b}$$

$$F_{d1} = \frac{\sigma^2-1}{4\sigma^2} + \frac{1}{2}\ell n\sigma + E_1\int_1^\sigma \{V_1(\xi) + \xi F_1\}\cos\phi\, d\xi + \frac{E_1 g_1}{\sigma}\cos\phi - \frac{E_1}{2}\left(1 + \frac{1}{\sigma^2}\right)\cos\phi \quad , \tag{5.30c}$$

$$F_{d2} = \frac{\sigma^2-R^2}{4\sigma^2} + \frac{1}{2}\ell n\frac{\sigma}{R} + E_1\int_R^\sigma \{V_1(\xi) + \xi F_1\}\cos\phi\, d\xi + \frac{E_1 g_1}{\sigma}\cos\phi \quad . \tag{5.30d}$$

By using new lift and drag functionals, the variation of $H = D + \lambda L$ leads to the same Euler-Lagrange equation as Eq. (5.8) and the transversality conditions are

$$\left[F_{d2} + \frac{\lambda}{\delta} F_{\ell 2}\right]_{\phi=\phi_\ell} = 0 \tag{5.31}$$

and

$$\left[(F_{d1}-F_{d2}) + \frac{\lambda}{\delta}(F_{\ell 1} - F_{\ell 2})\right]_{\phi=\phi_\delta} = 0 \tag{5.32}$$

In a similar way of class B configuration cases, Eq. (5.31) is satisfied automatically by the boundary condition $R(\phi_\ell) = \sigma$. Eq. (5.32) can be written by applying the condition $R(\phi_\delta) = 1$ as

$$\frac{E_1}{2}\left(1 + \frac{1}{\sigma^2}\right) + \frac{\lambda}{\delta} E_1 \cos^2\phi_\delta = 0 \tag{5.33}$$

Then by using the relation

$$\frac{\lambda}{\delta} = -\frac{1}{\sigma\cos\phi_\ell} + O(E_1) \tag{5.34}$$

and

$$\frac{\cos\phi_\delta}{\cos\phi_\ell} = \frac{\sigma^2+1}{2\sigma} + O(E_1) \tag{5.35}$$

from Eq. (4.10) and Eq. (4.16), Eq. (5.33) is also satisfied since $O(E_1{}^2)$ is neglected in this analysis.

Finally the solution for $R(\phi)$ for the class A configurations is also given in the form of an inverse function as

$$\begin{cases} \xi = 1 + E_1 \cos\phi & \text{for} \quad 0 < \phi < \phi_\delta \\ \phi = \cos^{-1}\left[\dfrac{-B(R) - \sqrt{B^2(R) - 4A(R)C(R)}}{2A(R)}\right] & \text{for } \phi_\delta<\phi<\phi_\ell \end{cases} \tag{5.36}$$

where $A(R)$, $B(R)$ and $C(R)$ are given in eq. (5.16b) and $\bar{\lambda}$ given in Eq. (5.11). The value for ϕ_δ can be obtained from Eq. (5.36) by using $R = 1$.

In Fig. 5.2, 5.3, and 5.4, the trailing edges of the semi-optimized configurations are shown for $K_\delta = 0.5, 1.0, 5.0$ for various values of ϕ_ℓ which are 20° to 80° with 20° interval. Therefore, there are four trailing edges shown for given K_δ and E_1. For each K_δ, the

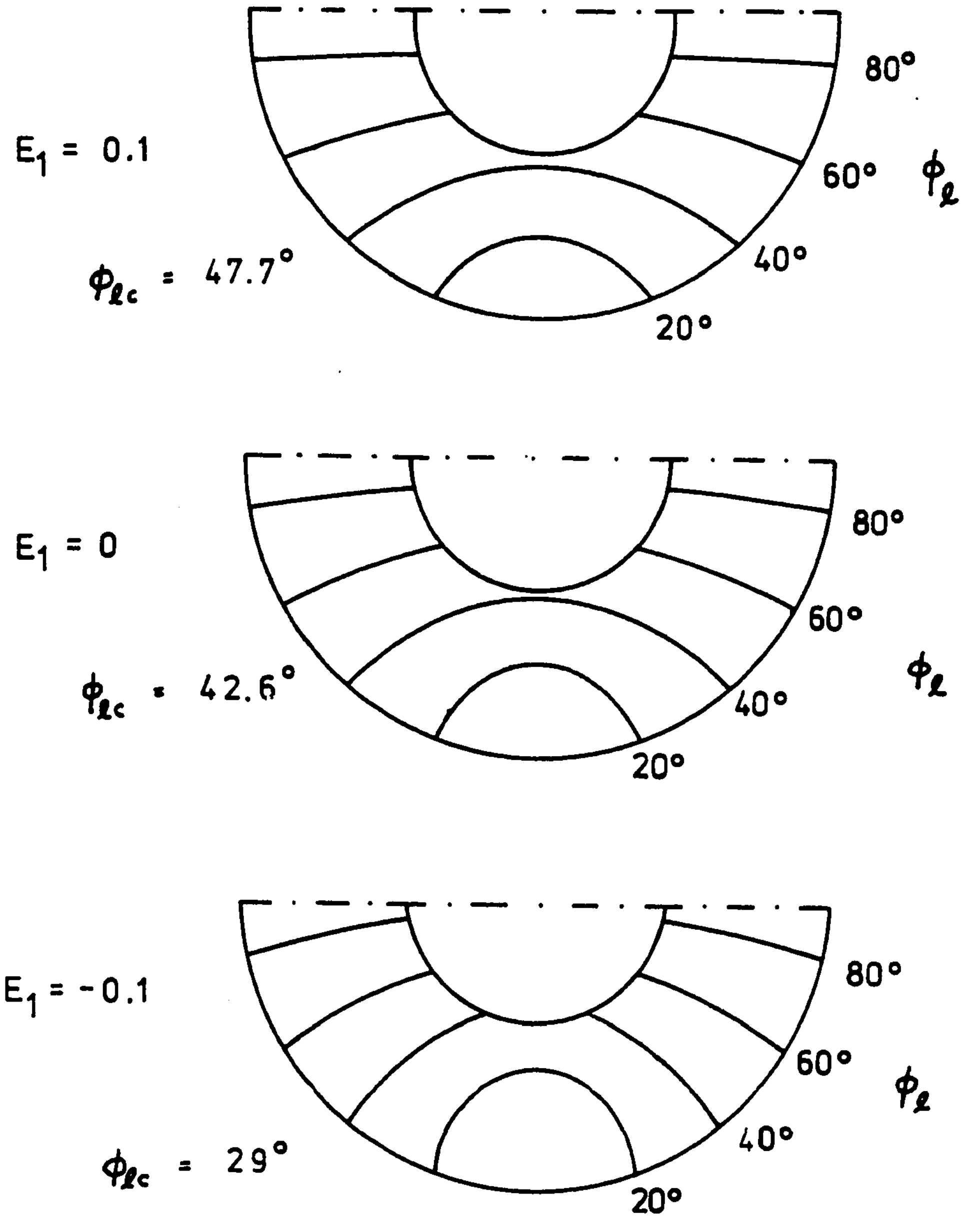

Fig. 5.2 Trailing Edge of the Compression Stream Surface for Semi-Optimized Waverider in n=1 Case (K_δ=0.5).

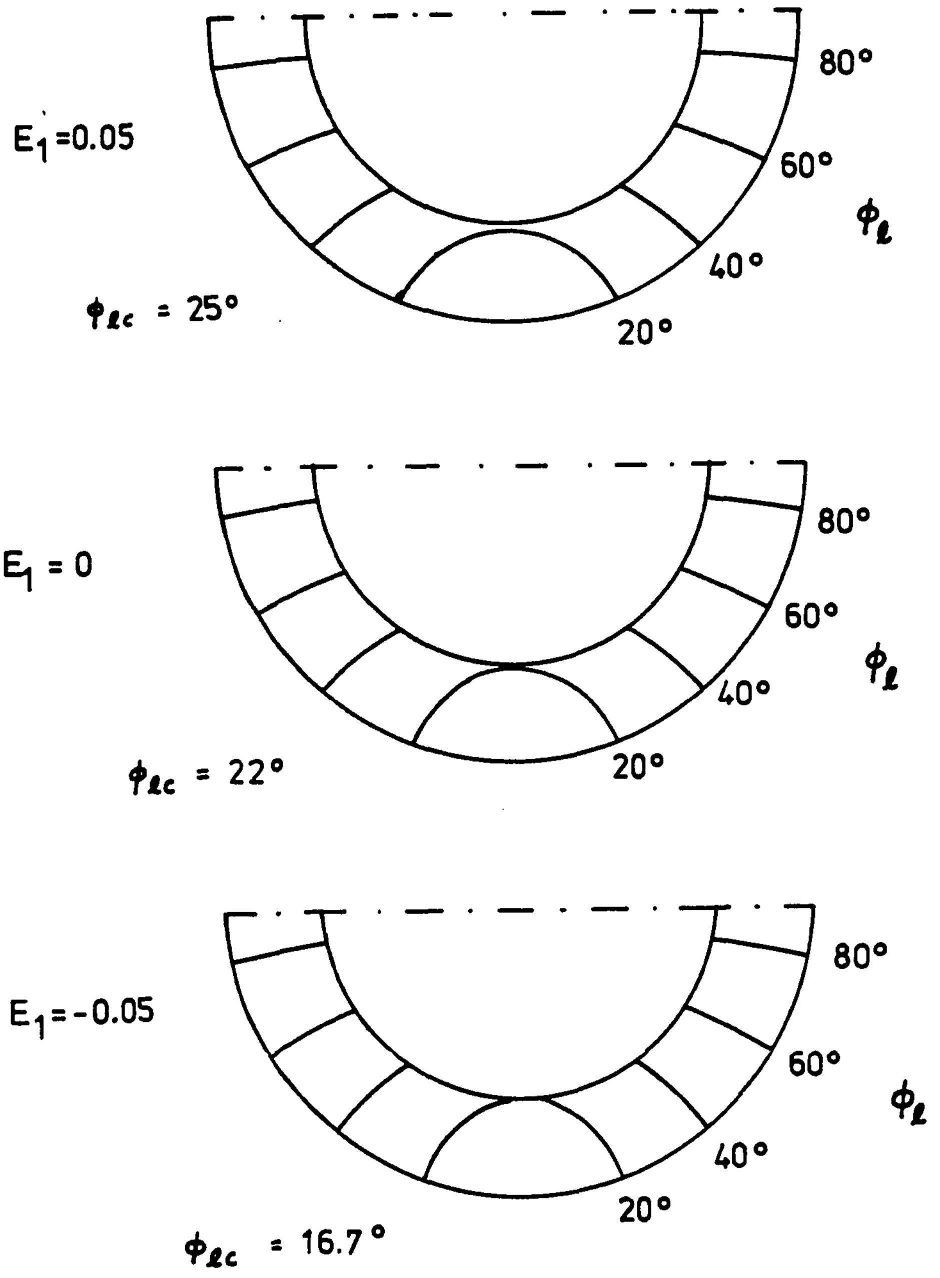

Fig. 5.3 Trailing Edge of the Compression Stream Surface for Semi-Optimized Waverider for n=1 Case (K_δ=1.0).

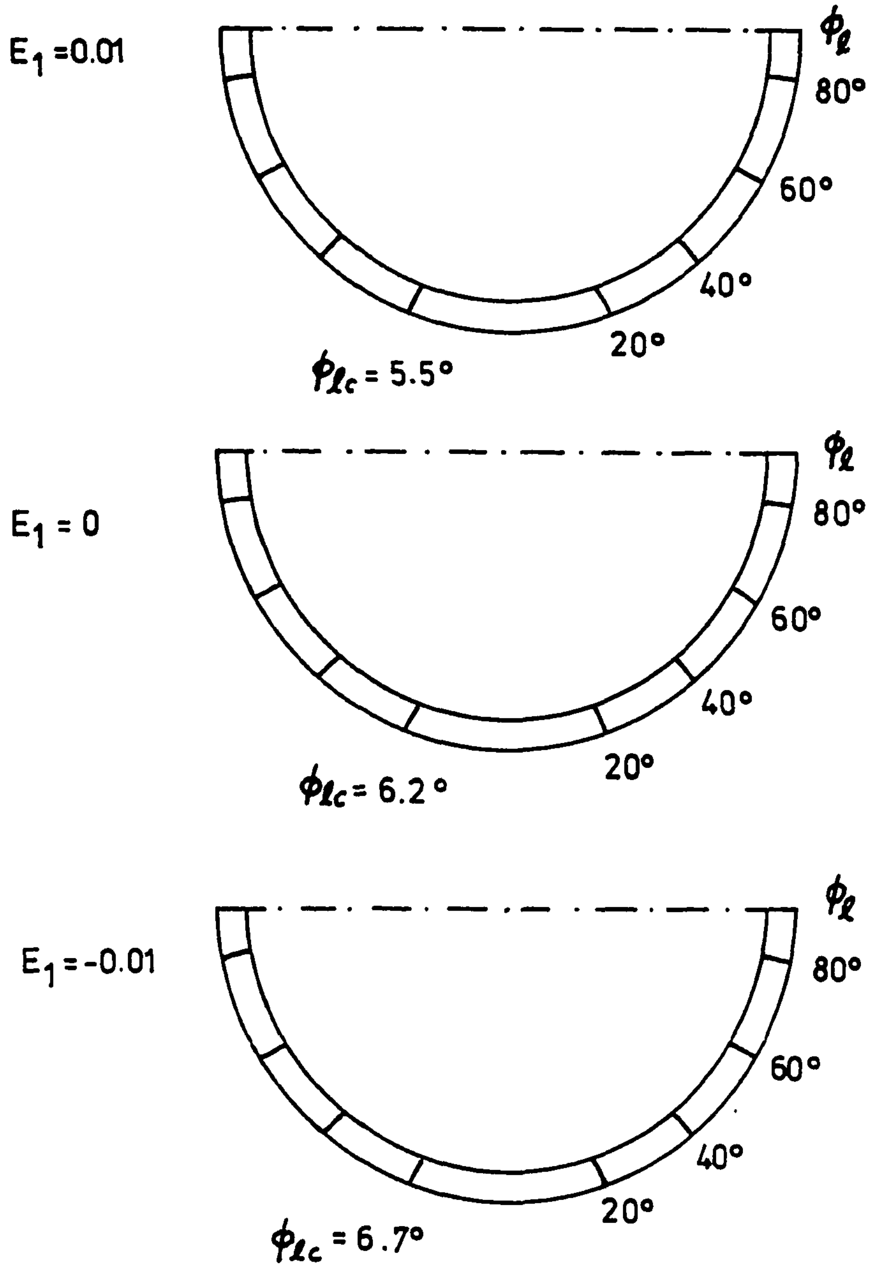

Fig. 5.4 Trailing Edge of the Compression Stream Surface for Semi-Optimized Waverider for n=1 Case (K_δ=5.0).

trailing edges for $E_1 = 0$ case are also shown in order to show the effect of E_1. Also $\phi_{\ell c}$ is plotted to distinguish class A configurations from class B. When E_1 is positive, the angle ϕ of the trailing edges decreases more rapidly as ξ decreases than $E_1 = 0$ case so the shock layer base plane area of the positive E_1 case is smaller than that of $E_1 = 0$ case for given K_δ and ϕ_ℓ.

The lift and drag of the semi-optimized configurations are calculated by using a numerical integration method and plotted in Fig. 5.5 for various values of K_δ and E_1. The curves for $E_1 = 0$ case for each K_δ, are exactly the same as those in Fig. 4.13. As E_1 decreases for given K_δ and lift, the drag decreases except the region near $\phi_\ell =$ 90°. The solid circle and triangle indicates each value $\phi_{\ell c}$ for given E_1 and K_δ. At small K_δ value, the effect of E_1 is smaller than large K_δ value. This means small deviation from a circular cone changes lift and drag more for large K_δ than for small K_δ.

5.2 Fully-Optimized Configurations

Performing the differentiation of the functional H with respect to δ leads

$$\frac{\partial}{\partial\delta}\left(\frac{\delta^4\sigma^2}{\sigma^2-1}\, I_d + \lambda\, \frac{\delta^3\sigma^2}{\sigma^2-1}\, I_\ell\right) = 0 \quad , \tag{5.37}$$

where

$$I_d = \begin{cases} \int_0^{\phi_\ell} F_d\, d\phi \quad , & \text{for class B} \\ \int_0^{\phi_\delta} F_{d1}\, d\phi + \int_{\phi_\delta}^{\phi_\ell} F_{d2}\, d\phi \; , & \text{for class A} \end{cases}$$

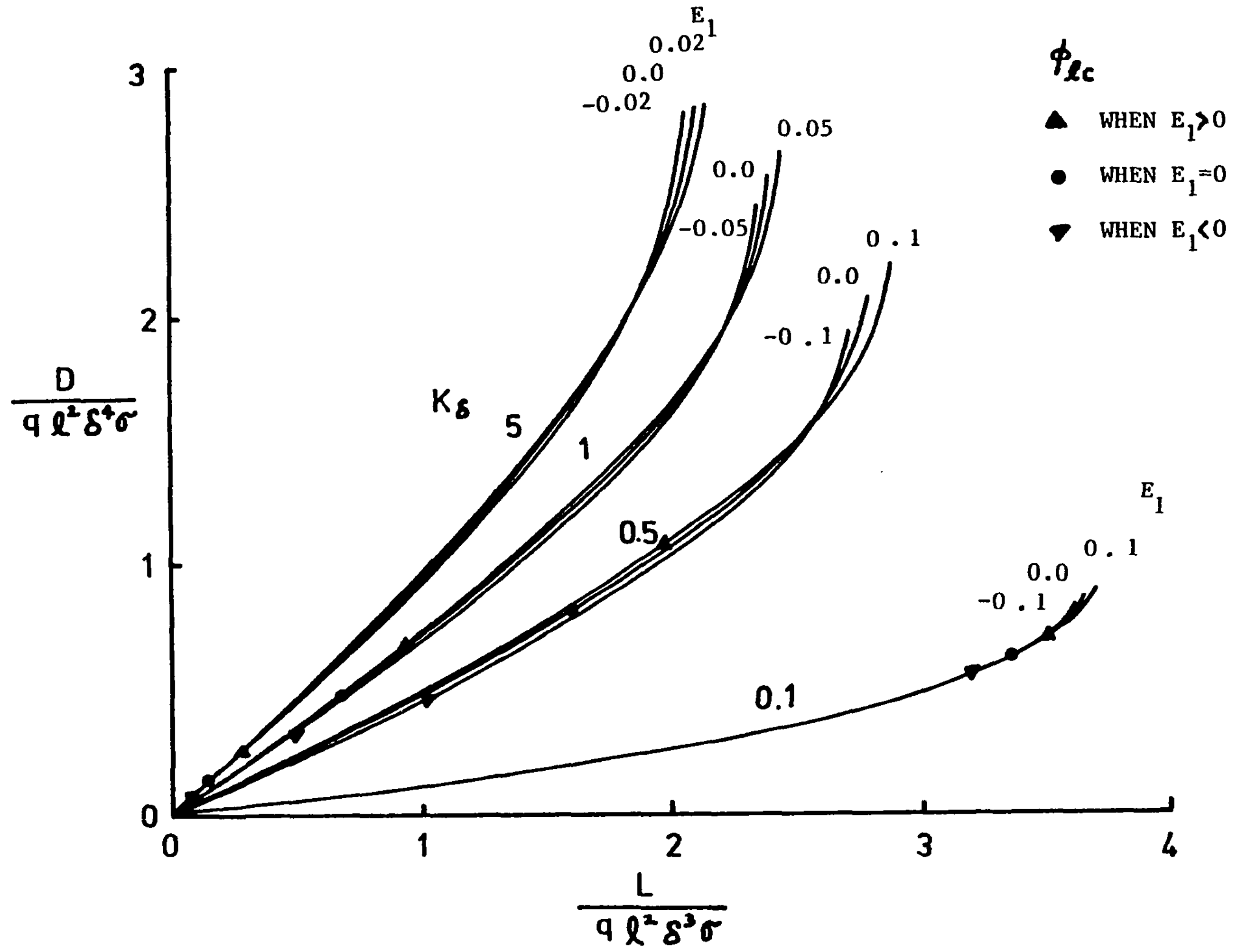

Fig. 5.5 Drag as a Function of Lift for Semi-Optimized Waveriders of n=1 Case.

$$I_\ell = \begin{cases} \int_0^{\phi_\ell} F_\ell \, d\phi & , \quad \text{for class B} \\ \int_0^{\phi_\delta} F_{\ell 1} \, d\phi + \int_{\phi_\delta}^{\phi_\ell} F_{\ell 2} \, d\phi & , \quad \text{for class A} \end{cases}$$

Using the relations

$$\frac{\partial \sigma}{\partial \delta} = - \frac{1}{K_\delta{}^2 \sigma \delta}$$

and

$$\frac{\partial K_\delta}{\partial \sigma} = - \sigma K_\delta^3$$

Eq. (5.37) can be written as

$$\bar{\lambda} = - \frac{\left(4\sigma^2 K_\delta{}^2 + \frac{2}{\sigma^2 - 1}\right) I_d + \sigma^2 K_\delta{}^3 \frac{\partial I_d}{\partial K_\delta}}{\left(3\sigma^2 K_\delta{}^2 + \frac{2}{\sigma^2 - 1}\right) I_\ell + \sigma^2 K_\delta{}^3 \frac{\partial I_\ell}{\partial K_\delta}} \tag{5.38}$$

where $\bar{\lambda}$ is given in Eq. (5.12).

Because I_d and I_ℓ involve complex functions of K_δ and ϕ_ℓ, it is impossible to solve the equation analytically. Therefore, a numerical scheme of the finite difference for calculating the derivatives in Eq. (5.38) is used as

$$\frac{\partial I}{\partial K_\delta} \cong \frac{I(\phi_\ell, K_\delta + \Delta K_\delta) - I(\phi_\ell, K_\delta - \Delta K_\delta)}{2\Delta K_\delta} \tag{5.39}$$

where ΔK_δ is a small value and I is either I_d or I_ℓ.

Fig. 5.6 shows the optimum values of ϕ_ℓ, denoted by $\phi_{\ell 0}$, as functions of K_δ for various values of E_1. As E_1 increases, $\phi_{\ell 0}$ decreases for given value of K_δ except K_δ is very small K_δ where $\phi_{\ell 0} \to$ 72.4° as $K_\delta \to 0$ and $\phi_{\ell 0} \to 49°$ as $K_\delta \to \infty$. The curve for $E_1 = 0$ case is identical to that of Fig. 4.17 that confirms the accuracy of the numerical calculation.

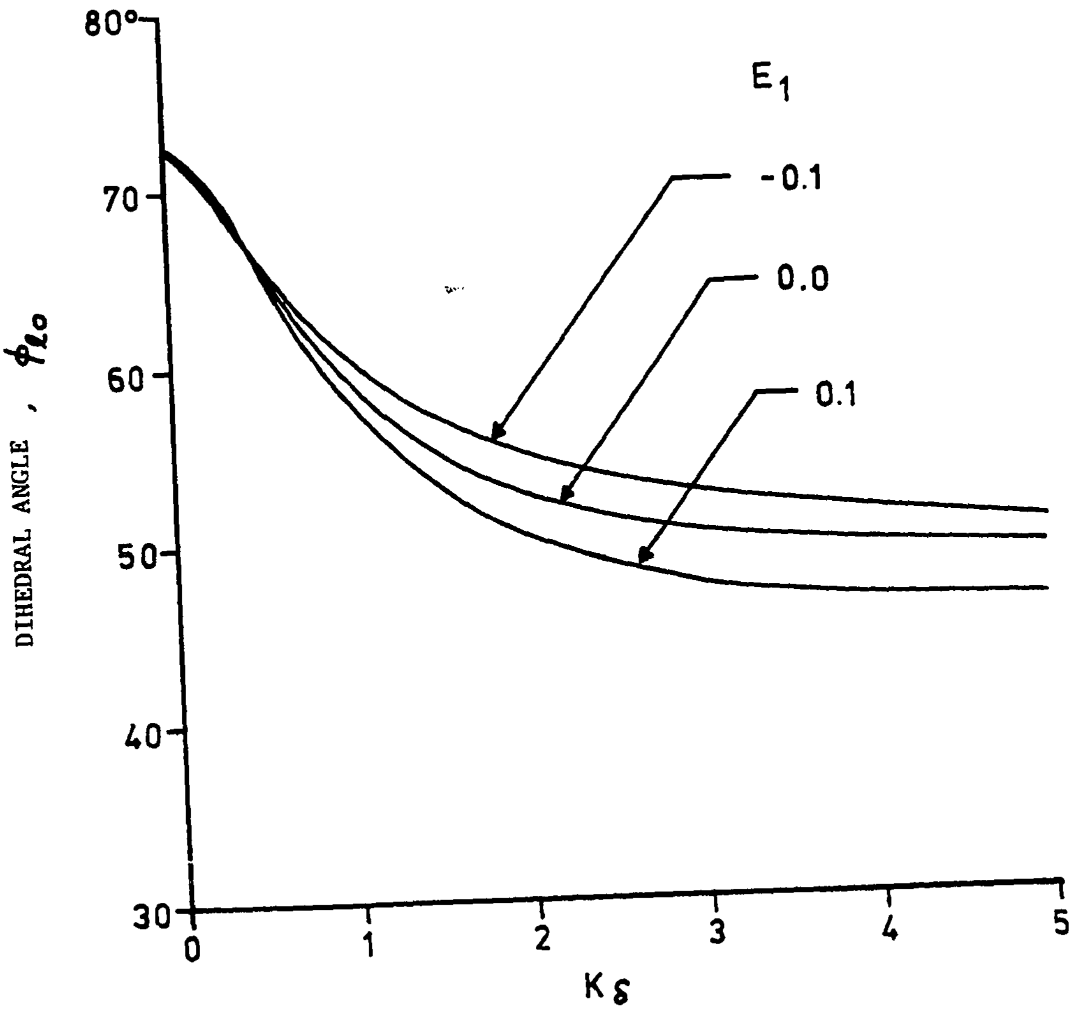

Fig. 5.6 Dihedral Angle of Fully-Optimized Waveriders of n=1 Case.

In Fig. 5.7, the lift and drag ratio of the fully optimized configurations are shown in forms of $(L\delta)/(D\sigma)$ as functions of K_δ for various E_1 values. As we expected, the negative value of E_1 case has higher lift-to-drag ratio than positive E_1 case.

Fig. 5.8 shows actual value of L/D ratio of the fully optimized configurations for $M_\infty = 4.0$ as a function of δ for various values of E_1. Again, negative values of E_1 case shows higher L/D ratio than positive E_1 case.

5.3 Free Stream Surfaces

The streamlines of the flow field of n = 1 case can be determined from the solution of

$$\vec{V} \times d\vec{s} = 0 \tag{5.40}$$

where $\vec{s}$ is a vector giving position along the streamline and

$$\begin{aligned}\vec{V} &= [u_0(\theta) + \varepsilon_1 u_1(\theta)\cos\phi]\,\hat{e}_r \\ &+ [v_o(\theta) + \varepsilon_1 v_1(\theta)\cos\phi]\,\hat{e}_\theta \\ &+ [\varepsilon_1 w_1(\theta)\sin\phi]\,\hat{e}_\phi \quad .\end{aligned}$$

In spherical polar coordinates, Eq. (5.40) can be reduced to

$$\frac{dr}{u_0+\varepsilon_1 u_1\cos\phi} = \frac{rd\theta}{v_0+\varepsilon_1 v_1\cos\phi} = \frac{r\sin\theta\, d\phi}{\varepsilon_1 w_1\sin\phi} \tag{5.41}$$

To the lowest order, Eq. (5.41) becomes

$$\frac{dr}{r} = \frac{u_0}{v_0}\,d\theta \tag{5.42}$$

$$\frac{w_1}{v_0\sin\theta} = \frac{d\phi}{\varepsilon_1\sin\phi} \tag{5.43}$$

Eq. (5.42) can be integrated by using approximations for u_0 and v_0 in Eq. (2.16) to give

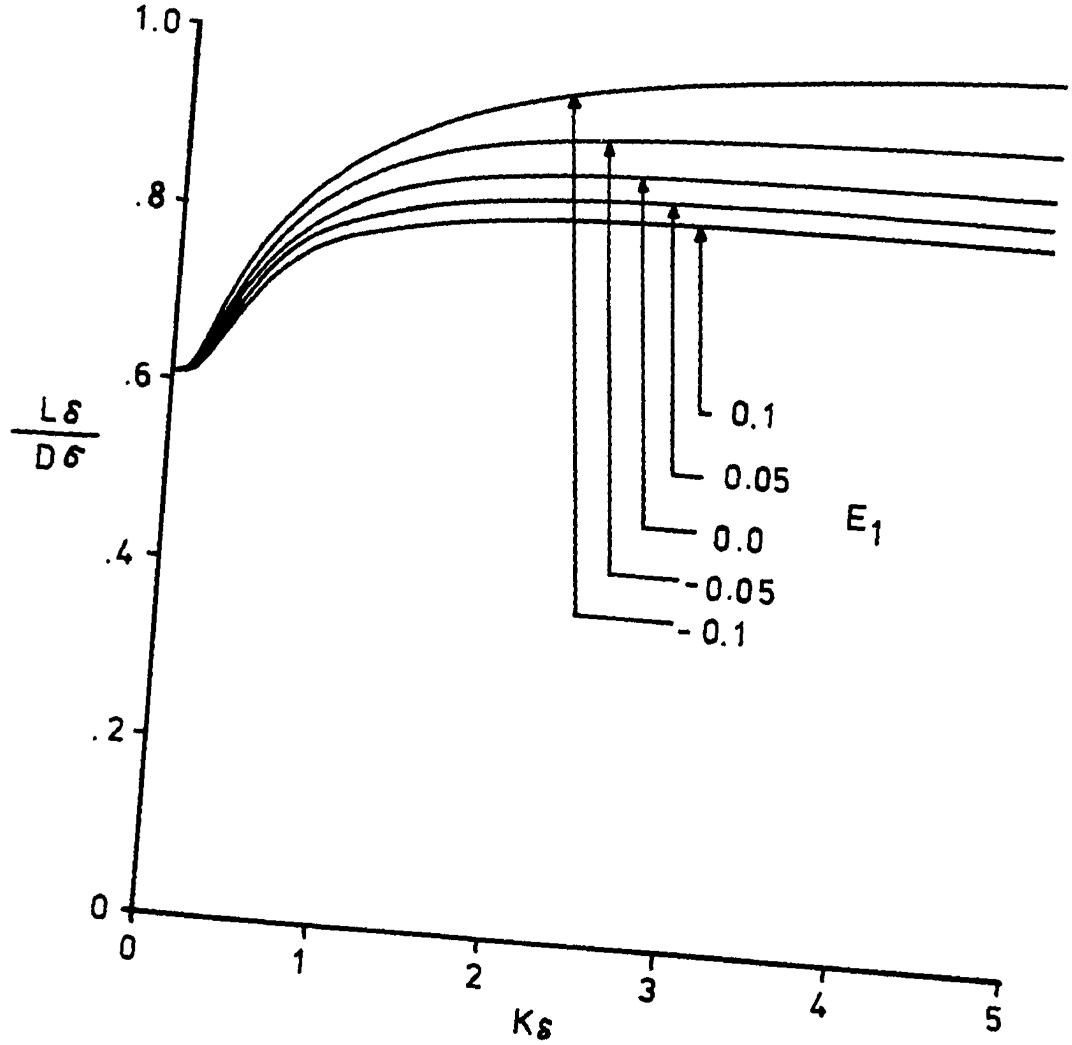

Fig. 5.7 Lift-to-Drag Ratio as a Function of K_δ for Fully-Optimized Waverider of n=1 Case.

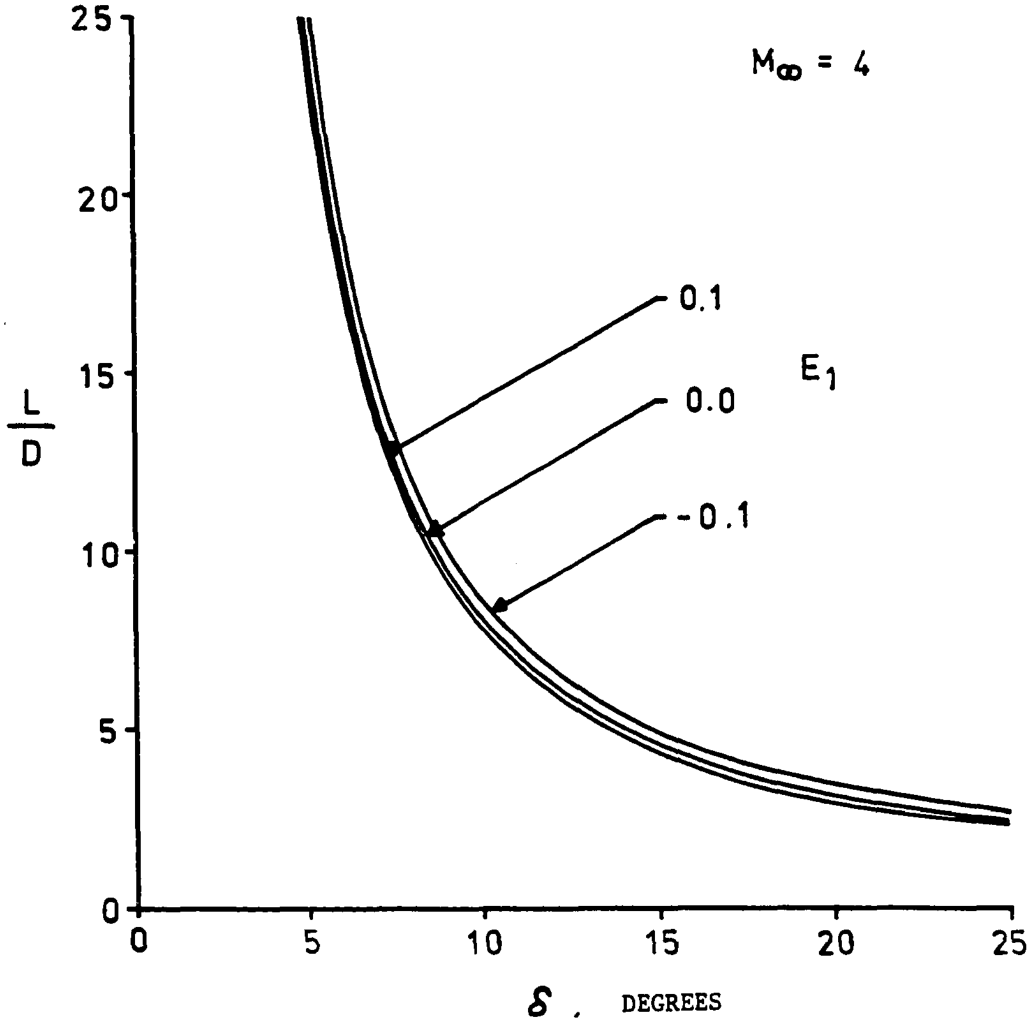

Fig. 5.8 Lift-to-Drag Ratio as a Function of Cone Angle for Fully-Optimized Waverider of n=1 Case.

$$r_s = r\left(\frac{\theta^2-\delta^2}{\theta_s{}^2-\delta^2}\right)^{1/2} \qquad (5.44)$$

where r_s and θ_s are constants of integration and correspond to the streamline passing through the point at (r_s,θ_s,ϕ_s) on the shock.

Eq. (5.43) can be integrated to give

$$\tan\left(\frac{\phi_s}{2}\right) = \tan\left(\frac{\phi}{2}\right) \exp\left[\int_{\theta}^{\theta_s} \frac{\varepsilon_1 w_1}{\theta v_0}\, d\theta\right] \qquad (5.45)$$

where ϕ_s and θ_s are constants of integration. Eq. (5.45) can be integrated approximately, however, in this paper, Eq. (5.45) is integrated numerically.

The trailing edge of the compression stream surface which orginates from the leading edge at (r_s,θ_s,ϕ_s) on the shock can be obtained by setting $\theta=\theta_b$ and $r=\ell$ in Eq. (5.44) and Eq. (5.45) and we get

$$r_s = \ell\left(\frac{\theta_b{}^2-\delta^2}{\theta_s{}^2-\delta^2}\right)^{1/2} \qquad (5.46)$$

and

$$\tan\left(\frac{\phi_s}{2}\right) = \tan\left(\frac{\phi_b}{2}\right) \exp\left[\int_{\theta_b}^{\theta_s} \frac{\varepsilon_1 w_1}{\theta v_0}\, d\theta\right] \qquad (5.47)$$

where the point (ℓ,θ_b,ϕ_b) in the shock layer base plane is on the same streamline which passing through the point at (r_s,θ_s,ϕ_s) at the shock.

The free stream surface intersecting the leading edge of the compression stream surface is given by

$$r\theta = r_s\theta_s \quad \text{and} \quad \phi = \phi_s \qquad (5.48)$$

and the corresponding trailing edge of the free stream surface in the shock layer base plane can be obtained by setting $r = \ell$ and $\theta=\theta_{fs}$ in

Eq. (5.48) as

$$\theta_{fs} = \frac{r_s}{\ell}\,\theta_s \quad \text{and} \quad \phi = \phi_s \tag{5.49}$$

By using Eq. (5.46), it can be written as

$$\theta_{fs} = \theta_s \left(\frac{\theta_b{}^2-\delta^2}{\theta_s{}^2-\delta^2}\right)^{1/2} \quad \text{and} \quad \phi = \phi_s \tag{5.50}$$

Noticing $\theta_b/\delta = R(\phi_b)$ we can get

$$R_{fs} = \sigma \left(\frac{R^2(\phi_b)-1}{\sigma^2-1}\right)^{1/2} \quad \text{and} \quad \phi = \phi_s \tag{5.51}$$

where the relation between ϕ_b and ϕ_s is

$$\tan\left(\frac{\phi_s}{2}\right) = \tan\left(\frac{\phi_b}{2}\right) \exp\left[\int_{R(\phi_b)}^{\sigma} \frac{E_1 W_1}{\xi V_0}\, d\xi\right] \tag{5.52}$$

Therefore the trailing edge of the free stream surface can be determined from given trailing edge of the compression stream surface.

The free stream surface and compression stream surface of the fully-optimized configurations for given E_1 and K_δ are shown in Fig. 5.9, 5.10, and 5.11 for K_δ = 0.5, 1.0, 5.0. Two semi-optimized configurations are also shown in the figures. For positive E_1 case, the base plane of the configuration is thinner than the negative E_1 case.

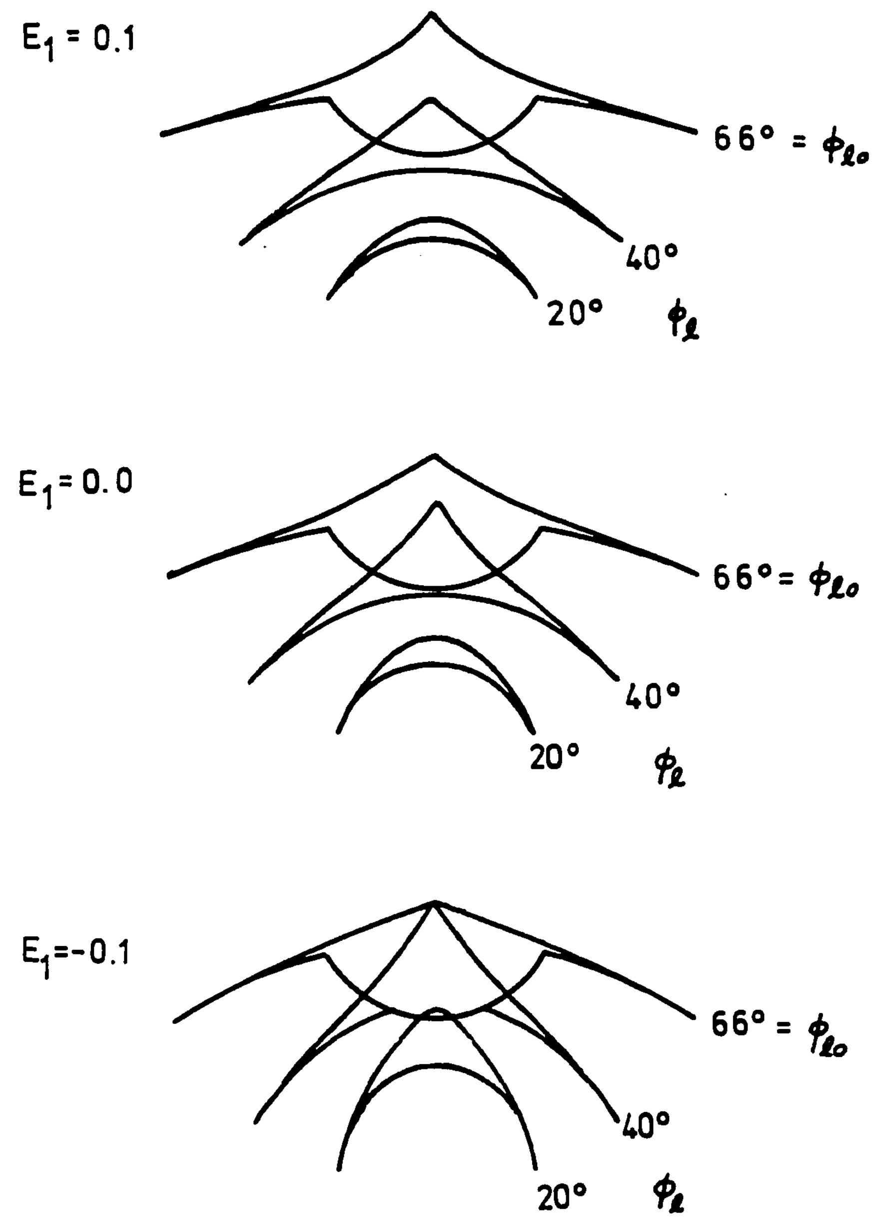

Fig. 5.9 Base Shapes of Fully-Optimized and Semi-Optimized Waveriders when $K_\delta = 0.5$.

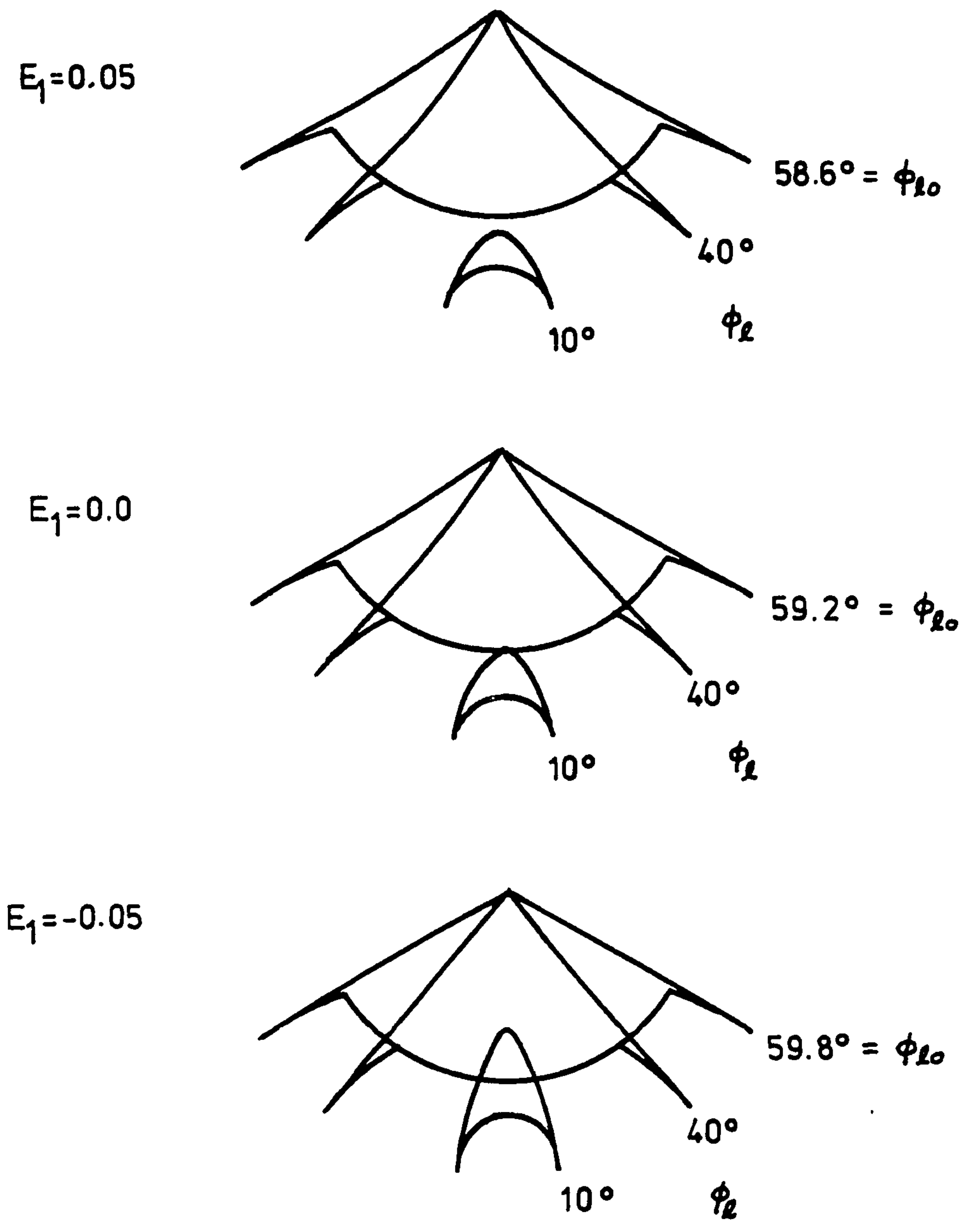

Fig. 5.10 Base Shapes of Fully-Optimized and Semi-Optimized Waveriders when K_δ = 1.0.

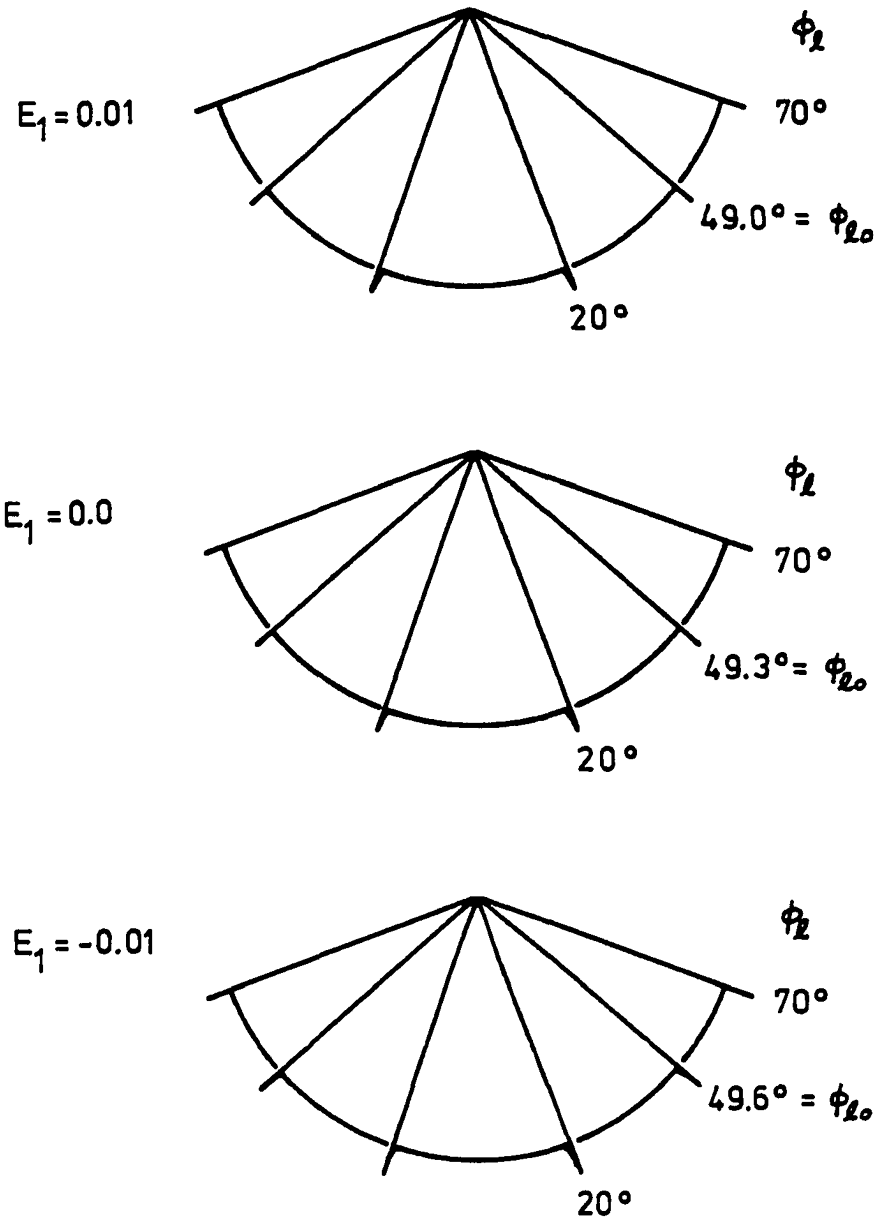

Fig. 5.11 Base Shapes of Fully-Optimized and Semi-Optimized Waveriders when $K_\delta = 5.0$.

SECTION VI

WAVERIDER CONFIGURATIONS OF N = 2 CASE

The body and shock expressions in Eq. (2.9) and Eq. (2.10) for $n = 2$ case become

$$\theta_{body} = \delta(1 + E_2 \cos 2\phi) \tag{6.1}$$

$$\theta_{shock} = \delta(\sigma + E_2 g_2 \cos 2\phi) \tag{6.2}$$

in spherical polar coordinates, where $E_2 = \varepsilon_2/\delta$ is a small parameter and δ and β are semi-vertex angle of body and shock of a circular cone. Since Eq. (6.1) represents an elliptic cone body with an error of $O(E_2{}^2)$, the optimization problem of $n = 2$ case is to obtain optimum shapes from the flow past an elliptic cone with zero angle of attack.

The lift and drag expressions of Eq. (2.26) for $n = 2$ case then become

$$L = 4q\ell^2\delta^3 \frac{\sigma^2}{\sigma^2-1} \int_0^{\phi_\ell} F_\ell(R(\phi), \phi; \sigma, E_2)\, d\phi \tag{6.3}$$

$$D = 4q\ell^2\delta^4 \frac{\sigma^2}{\sigma^2-1} \int_0^{\phi_\ell} F_d(R(\phi), \phi; \sigma, E_2)\, d\phi \tag{6.4}$$

where

$$F_\ell = \{\sigma - R(\phi)\} \cos\phi + E_2 \int_{R(\phi)}^{\sigma} \xi\{V_2(\xi) \cos 2\phi \cos\phi$$

$$- W_2(\xi) \sin 2\phi \sin\phi\}\, d\xi + E_2 g_2 \cos 2\phi \cos\phi \tag{6.5}$$

$$F_d = \frac{\sigma^2 - R^2(\phi)}{4\sigma^2} - \frac{1}{2}\ell n\frac{R(\phi)}{\sigma} + E_2\int_{R(\phi)}^{\sigma}\{V_2(\xi) + \xi F_2\}\cos 2\phi\, d\xi$$

$$+ \frac{E_2 g_2}{\sigma}\cos 2\phi \qquad (6.6)$$

where $R(\phi)$ is the trailing edge function of the compression stream surface to be optimized in the next sections.

6.1 Semi-Optimized Configurations

When the parameters q, ℓ, M_∞ are fixed, following the same procedure in the previous chapters, the variational problem becomes the problem to that of minimizing functional

$$H = D + \lambda L \qquad (6.7)$$

where L and D are given in Eq. (6.3) and Eq. (6.4), respectively.

The Euler-Lagrange equation can be obtained as

$$\frac{R^2+\sigma^2}{2R\sigma^2} + E_2\{V_2(R) + RF_2\}\cos 2\phi$$

$$+ \frac{\lambda}{\delta}\{\cos\phi + E_2 R(V_2(R)\cos 2\phi\cos\phi - W_2(R)\sin 2\phi\sin\phi)\} = 0 \qquad (6.8)$$

and the transversality condition as

$$\left[F_d + \frac{\lambda}{\delta}F_\ell\right]_{\phi=\phi_\ell} = 0 \qquad (6.9)$$

The λ/δ term can be replaced by applying the boundary condition

$$R(\phi_\ell) = \sigma \qquad (6.10)$$

to Eq. (6.8) and the result is

$$\bar{\lambda} \equiv \frac{\lambda}{\delta} = -\frac{1/\sigma + E_2(V_2(\sigma) + \sigma F_2)\cos 2\phi_\ell}{\cos\phi_\ell + E_2\sigma\{V_2(\sigma)\cos 2\phi_\ell\cos\phi_\ell - W_2(\sigma)\sin\phi_\ell\sin 2\phi_\ell\}} \qquad (6.11)$$

where the values of $V_2(\sigma)$, $W_2(\sigma)$ and F_2 can be obtained from Appendix A as

$$V_2(\sigma) = \frac{4}{\gamma+1} g_2 \quad , \quad W_2(\sigma) = \frac{g_2}{\sigma^2} \quad , \quad F_2 = \frac{g_2}{\sigma^3}$$

When $E_2 = 0$, Eq. (6.11) becomes

$$\lambda = -\frac{\delta}{\sigma \cos\phi_\ell}$$

which is the same result as Eq. (4.5) for $E_n = 0$ case.

By using Eq. (6.10), the transversality condition becomes

$$\frac{E_2 g_2}{\sigma} + \bar{\lambda} E_2 g_2 \cos 2\phi_\ell = 0 \qquad (6.12)$$

which is automatically satisfied since we can write $\bar{\lambda}$ as

$$\bar{\lambda} = -\frac{1}{\sigma \cos\phi_\ell} + O(E_2)$$

then Eq. (6.12) becomes in order of $O(E_2{}^2)$ which is neglected in this paper.

Eq. (6.8) can be rewritten as

$$\cos^3\phi + A(R)\cos^2\phi + B(R)\cos\phi + C(R) = 0 \qquad (6.13a)$$

where

$$A(R) = 2E_2\{V_2(R) + RF_2\}/D(R)$$

$$B(R) = [\bar{\lambda} - \bar{\lambda} E_2 R\{V_2(R) + 2W_2(R)\}]/D(R)$$

$$C(R) = \frac{R^2+\sigma^2}{2R\sigma^2} - E_2\{V_2(R) + RF_2\}]/D(R)$$

and

$$D(R) = 2\bar{\lambda} E_2 R\{V_2(R) + W_2(R)\} \qquad (6.13b)$$

The Eq. (6.13), which is a cubic equation for $\cos(\phi)$, can be solved analytically and the solutions are also in inverse form as the $n = 1$ case. The result is

$$\cos^{-1}\{-\frac{a}{2}+\sqrt{b})^{1/3}+(-\frac{a}{2}-\sqrt{b})^{1/3}-\frac{A(R)}{3} \tag{6.14}$$

where

$$a=\frac{1}{27}\{2A^3(R)-9\,A(R)B(R)+27C(R)\}$$

$$b=\frac{a^2}{4}+\frac{c^3}{27}$$

$$c=\frac{1}{3}\{3B(R)-A^2(R)\}$$

The critical value, $\phi_{\ell c}$, for n = 2 case can be obtained by using the condition

$$R(0)=1 \quad \text{at} \quad \phi_\ell=\phi_{\ell c} \tag{6.15}$$

The value $\bar{\lambda}$ for $\phi_\ell = \phi_{\ell c}$, denoted by $\bar{\lambda}_c$, is obtained by applying Eq. (6.15) to Eq. (6.8) as

$$\bar{\lambda}_c=-\frac{(\sigma^2+1)/2\sigma^2+E_2\{V_2(1)+F_2\}}{1+E_2V_2(1)} \tag{6.16}$$

Equating Eq. (6.16) and Eq. (6.11), we can get the equation for $\phi_{\ell c}$ as

$$\cos^3\phi_{\ell c}+A^*(\sigma)\cos^2\phi_{\ell c}+B^*(\sigma)\cos\phi_{\ell c}+C^*(\sigma)=0 \tag{6.17}$$

where $A^*(\sigma)$, $B^*(\sigma)$ and $C^*(\sigma)$ have forms as those in Eq. (6.13b) but $\bar{\lambda}_c$ instead of $\bar{\lambda}$. Eq. (6.17) can be solved for $\cos(\phi_{\ell c})$ and plotted as a function of K_δ for various values of E_2 in Fig. 6.1. The curves are very similar to those of n = 1 case.

When $\phi_\ell > \phi_{\ell c}$ we have class A configurations and the function $R(\phi)$ consists of two curves

$$\begin{cases} \xi = 1+E_2\cos 2\phi & \text{for} \quad 0<\phi<\phi_\delta \\ \xi = R(\phi) & \text{for} \quad \phi_\delta<\phi<\phi_\ell \end{cases} \tag{6.18}$$

where ϕ_δ satisfies the condition $R(\phi_\delta) = 1$. Substitute Eq. (6.18) into

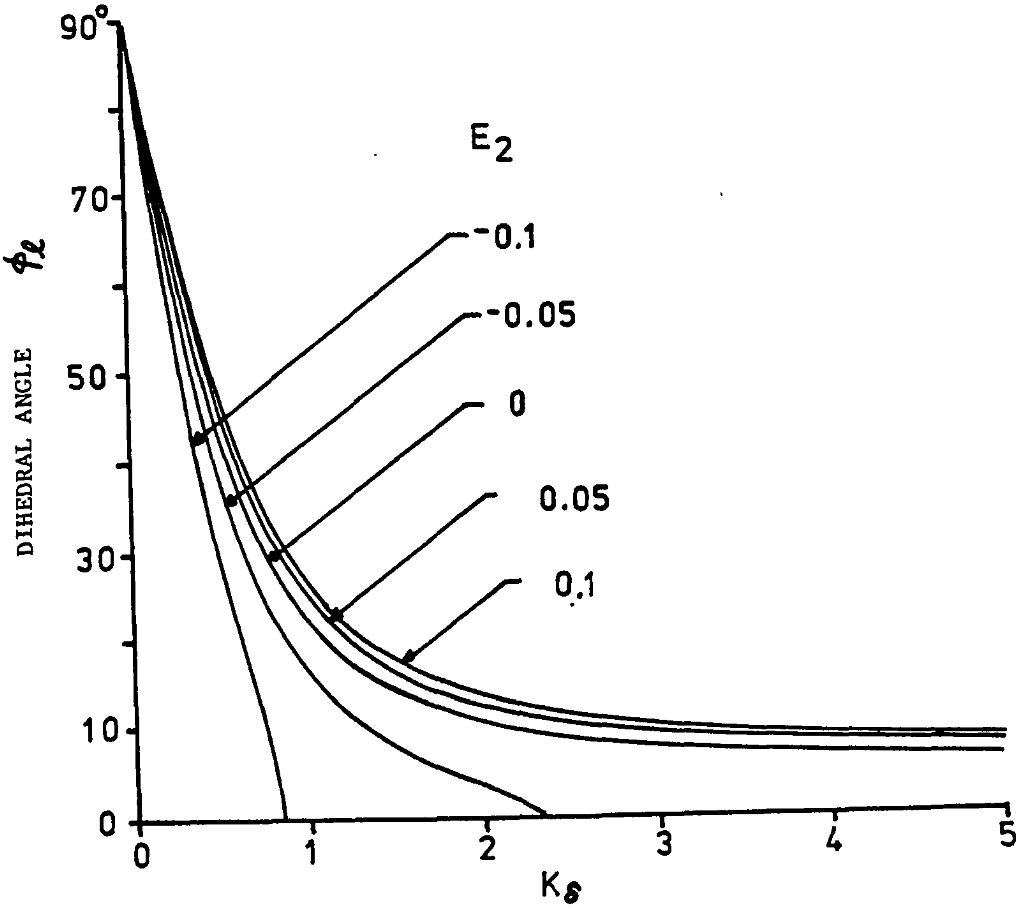

Fig. 6.1 Critical Dihedral Angle for Semi-Optimized Waveriders of n=2 Case.

Eq. (6.3) through Eq. (6.6) and neglecting lower order terms, we have

$$L = 4q\ell^2\delta^3 \frac{\sigma^2}{\sigma^2-1} \left[\int_0^{\phi_\ell} F_{\ell 1} d\phi + \int_{\phi_\delta}^{\phi_\ell} F_{\ell 2}\, d\phi\right] \tag{6.19}$$

$$D = 4q\ell^2\delta^4 \frac{\sigma^2}{\sigma^2-1} \left[\int_0^{\phi_\delta} F_{d1} d\phi + \int_{\phi_\delta}^{\phi_\ell} F_{d2}\, d\phi\right] \tag{6.20}$$

where

$$F_{\ell 1} = \{\sigma-1)\cos\phi + E_2 \int_1^{\sigma} \xi\{V_2(\xi)\cos 2\phi \cos\phi - W_2(\xi)\sin 2\phi \sin\phi\} d\xi$$
$$+ E_2(g_2-1)\cos 2\phi \cos\phi \tag{6.21a}$$

$$F_{\ell 2} = \{\sigma-R)\cos\phi - E_2 \int_R^{\sigma} \xi\{V_2(\xi)\cos 2\phi \cos\phi - W_2(\xi)\sin 2\phi \sin\phi\} d\xi$$
$$+ E_2 g_2 \cos 2\phi \cos\phi \tag{6.21b}$$

$$F_{d1} = \frac{\sigma^2-1}{4\sigma^2} + \frac{1}{2}\,\ell n\sigma + E_2\int_1^{\sigma} \{V_2(\xi) + \xi F_2\} \cos 2\phi\, d\xi$$
$$+ \frac{E_2 g_2}{\sigma}\cos 2\phi - \frac{E_2}{2}\left(1 + \frac{1}{\sigma^2}\right)\cos 2\phi \tag{6.21c}$$

$$F_{d2} = \frac{\sigma^2-R^2}{4\sigma^2} - \frac{1}{2}\,\ell n\frac{R}{\sigma} + E_2\int_R^{\sigma} \{V_2(\xi) + \xi F_2\} \cos 2\phi\, d\xi$$
$$+ \frac{E_2 g_2}{\sigma}\cos 2\phi \tag{6.21d}$$

By using the new lift and drag functionals, the variation of $H = D + \lambda L$ leads to the same Euler-Lagrange equation in Eq. (6.8) and the transversality conditions are

$$\left[F_{d2} - \frac{\lambda}{\delta} F_{\ell 2}\right]_{\phi=\phi_\ell} = 0 \tag{6.22}$$

and

$$\left[(F_{d1} - F_{d2}) + \frac{\lambda}{\delta}(F_{\ell 1} - F_{\ell 2})\right]_{\phi=\phi_\ell} = 0 \tag{6.23}$$

Eq. (6.22) again satisfied automatically with the condition $R(\phi_\ell) = \sigma$. Eq. (6.23) can be written by applying the condition $R(\phi_\delta) = 1$ as

$$\frac{E_2}{2}\left(1 + \frac{1}{\sigma^2}\right) + \frac{\lambda}{\delta} E_2 \cos\phi_\delta \cos 2\phi_\delta = 0 \tag{6.24}$$

Then by the relation

$$\frac{\lambda}{\delta} = -\frac{1}{\sigma\cos\phi_\ell} + O(E_2) \tag{6.25}$$

and

$$\frac{\cos\phi_\delta}{\cos\phi_\ell} = \frac{\sigma^2+1}{2\sigma} + O(E_2) \tag{6.26}$$

from Eq. (4.10) and Eq. (4.16), Eq. (6.24) is also satisfied automatically since $O(E_2{}^2)$ is neglected in the analysis.

The solution for $R(\phi)$ is also given in inverse form as Eq. (6.14). The value of ϕ_δ can be obtained from solving the equation for $R = 1$.

In Figs. 6.2, 6.3, and 6.4, the trailing edges of the semi-optimized configurations are shown for $K_\delta = 0.5$, 1.0, and 5.0 for various values of E_2. The values of ϕ_ℓ are from 20° to 80° with 20° intervals for each figure. The trailing edges of $E_2 = 0$ case are shown again to show the effect of E_2. The value of $\phi_{\ell c}$ is plotted for each figure to distinguish class A configurations from class B.

The lift and drag of the semi-optimized configurations are calculated by using numerical integration methods and plotted in Fig. 6.5 in terms of $L/(q\ell^2\delta^3\sigma)$ and $D/(q\ell^2\delta^4\sigma)$ for $K_\delta = 0.1$, 0.5, 1.0, and 5.0. As n = 1 case, the negative value of E_2 has less drag than positive E_2 case for given K_δ and lift.

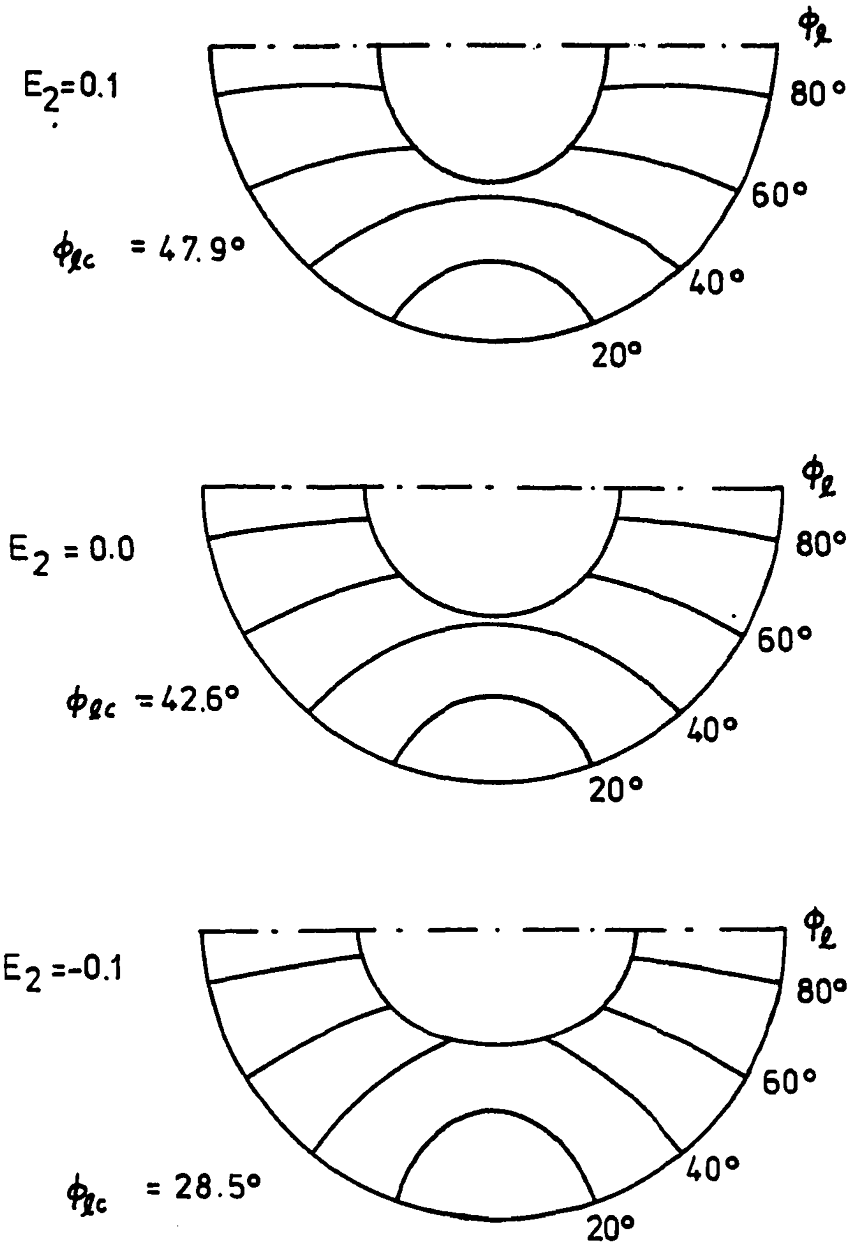

Fig. 6.2 Trailing Edge of the Compression Stream Surface for Semi-Optimized Waverider of n=2 Case (K_δ = 0.5).

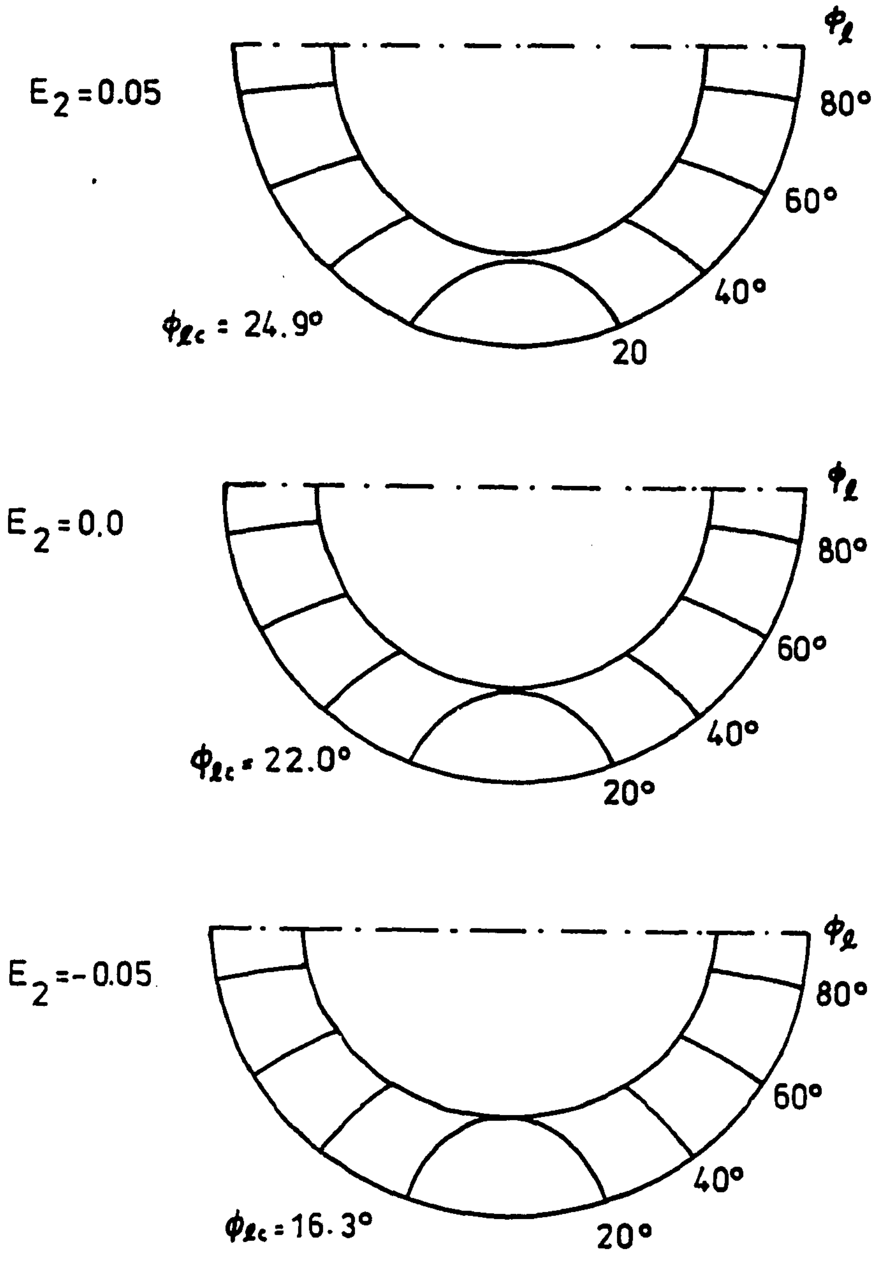

Fig. 6.3 Trailing Edge of the Compression Stream Surface for Semi-Optimized Waverider of n=2 Case (K_δ = 1.0).

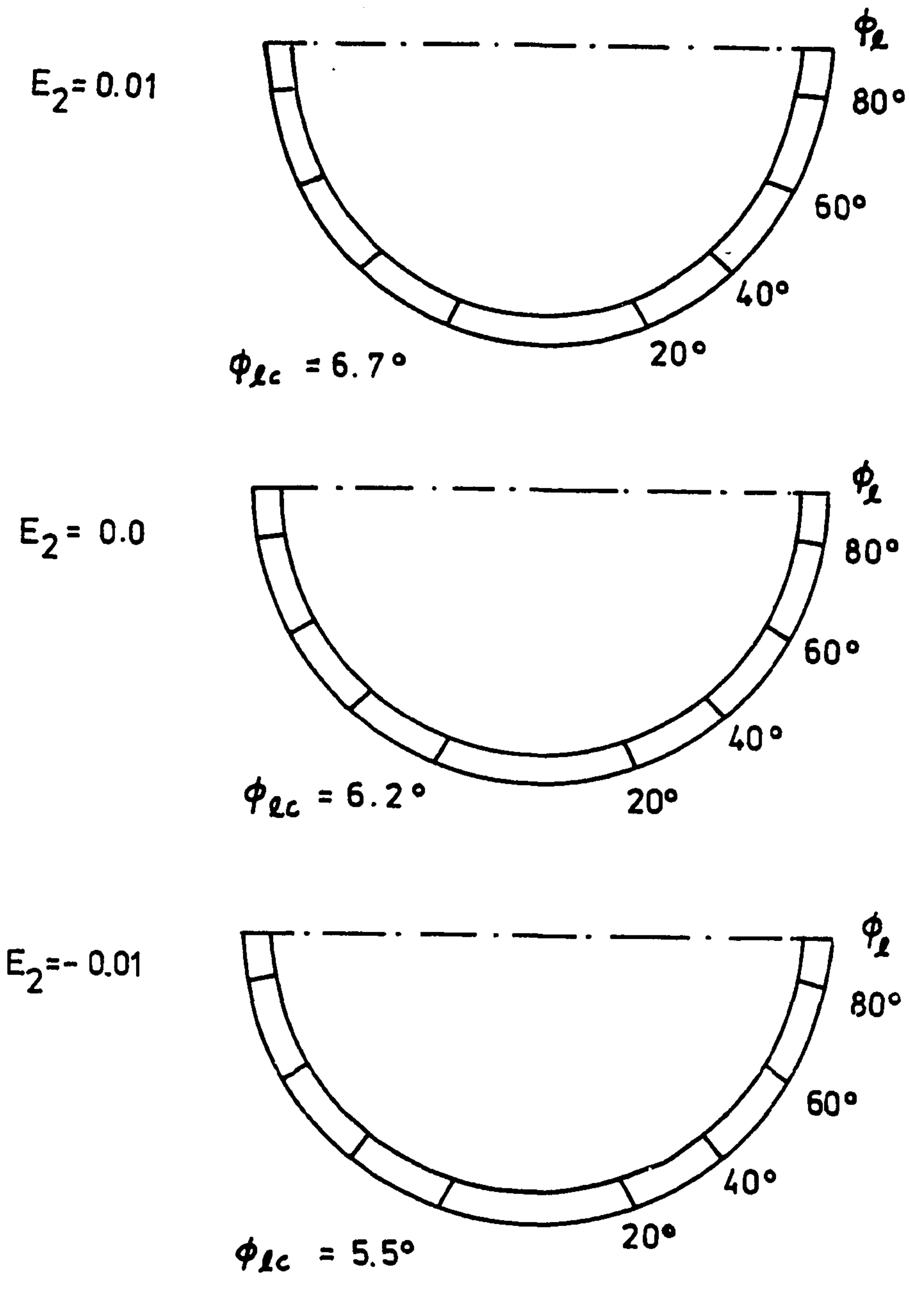

Fig. 6.4 Trailing Edge of the Compression Stream Surface for Semi-Optimized Waverider of n=2 Case (K_δ = 5.0).

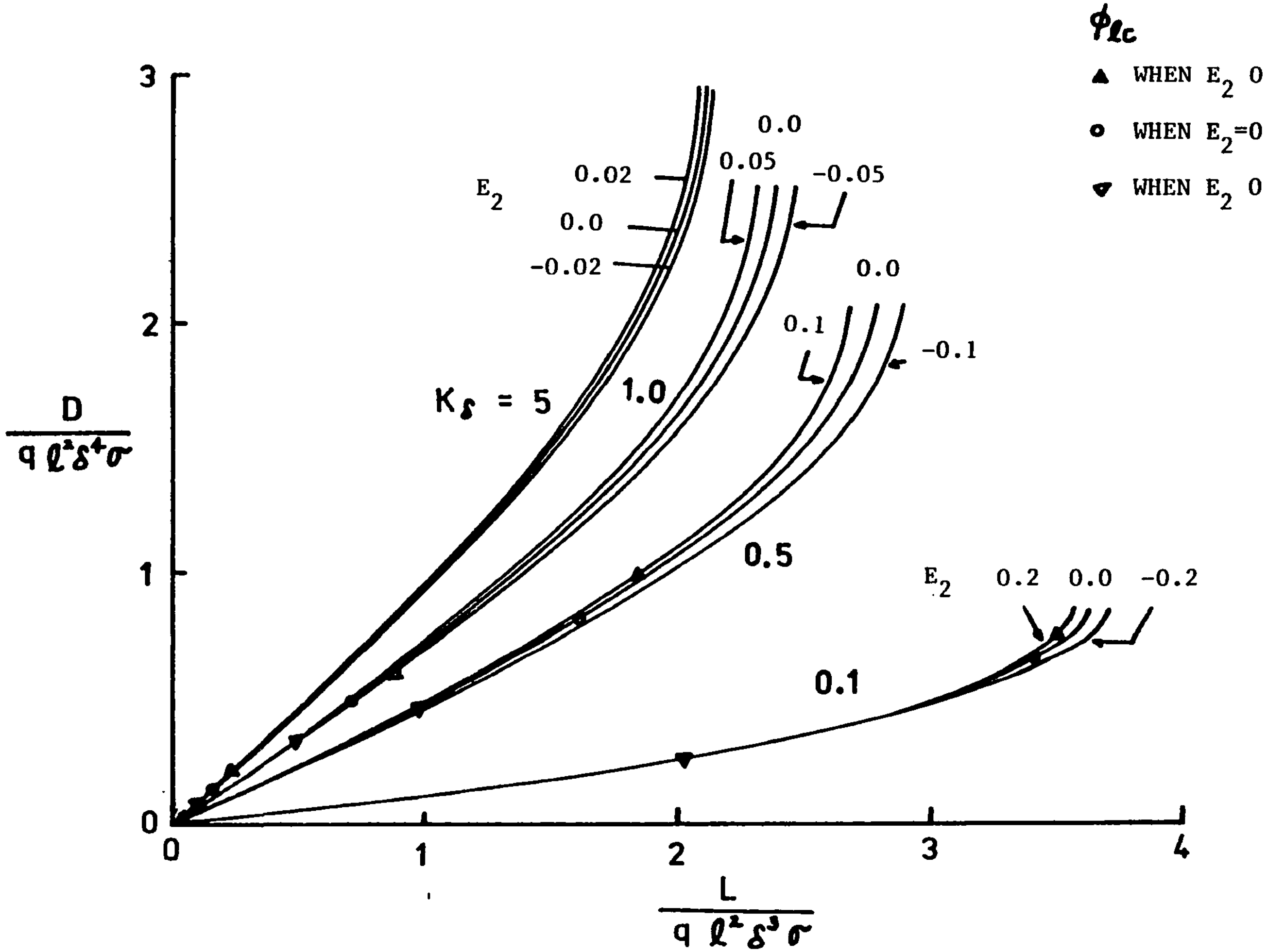

Fig. 6.5 Drag as a Function of Lift for Semi-Optimized Waveriders of n=2 Case.

6.2 Fully Optimized Configurations

Performing the differentiation of the functional H with respect to δ leads

$$\frac{\partial}{\partial\delta}\left(\frac{\delta^4\sigma^2}{\sigma^2-1} I_d + \lambda \frac{\delta^3\sigma^2}{\sigma^2-1} I_\ell\right) = 0 \qquad (6.26)$$

where

$$I_d = \begin{cases} \int_0^{\phi_\ell} F_d \, d\phi \quad , & \text{for class B} \\ \int_0^{\phi_\delta} F_{d1} \, d\phi + \int_{\phi_\delta}^{\phi_\ell} F_{d2} \, d\phi \, , & \text{for class A} \end{cases}$$

$$I_\ell = \begin{cases} \int_0^{\phi_\ell} F_\ell \, d\phi \quad , & \text{for class B} \\ \int_0^{\phi_\delta} F_{\ell 1} \, d\phi + \int_{\phi_\delta}^{\phi_\ell} F_{\ell 2} \, d\phi \, , & \text{for class A} \end{cases}$$

Using the relations

$$\frac{\partial\sigma}{\partial\delta} = - \frac{1}{K_\delta{}^2\sigma\delta}$$

and

$$\frac{\partial K\delta}{\partial\sigma} = - \sigma K\delta^3$$

we get

$$\bar{\lambda} = - \frac{\left(4\sigma^2 K_\delta{}^2 + \frac{2}{\sigma^2-1}\right) I_d + \sigma^2 K_\delta{}^3 \frac{\partial I_d}{\partial K_\delta}}{\left(3\sigma^2 K_\delta{}^2 + \frac{2}{\sigma^2-1}\right) I_\ell + \sigma^2 K_\delta{}^3 \frac{\partial I_\ell}{\partial K_\delta}} \qquad (6.28)$$

where $\bar{\lambda}$ is given in Eq. (6.11). Eq. (6.28) can be solved by using the same numerical scheme in section V and the results for $\phi_{\ell 0}$ are shown in Fig. 6.6 as a function of K_δ for various values of E_2. The curves are very similar to those of Fig. 5.6 of n = 1 case. Again $\phi_{\ell 0} \to 72.4°$ as $K_\delta \to 0$ and $\phi_{\ell 0} \to 49°$ as $K_\delta \to \infty$.

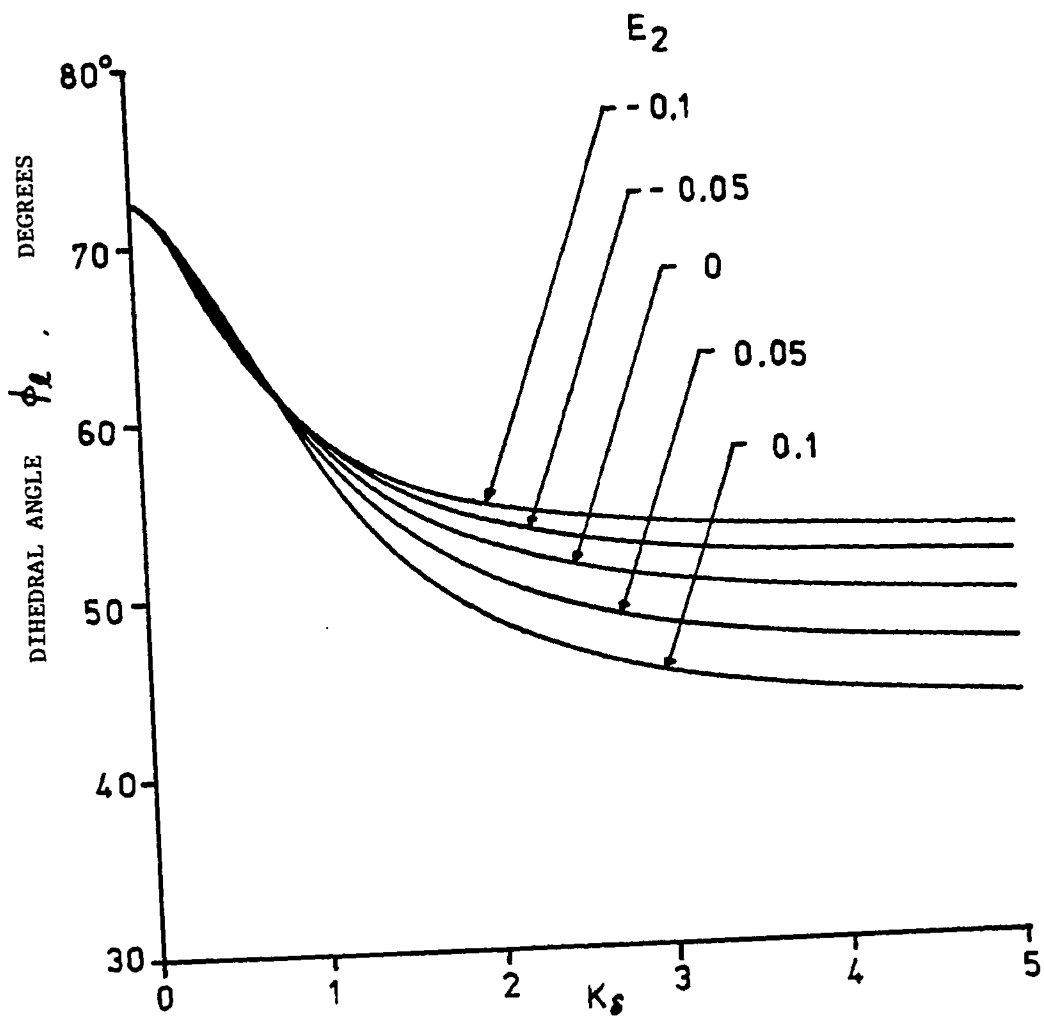

Fig. 6.6 Dihedral Angle of Fully-Optimized Waveriders of n=2 Case.

In Fig. 6.7, the lift and drag ratio of the fully optimized configurations are shown in forms of $(L\delta)/(D\sigma)$ as functions of K_δ for various E_2 values. As we expected, the negative value of E_2 case has higher lift-to-drag ratio than positive E_2 case.

Fig. 6.8 shows the actual value of L/D ratio of the fully optimized configurations for $M_\infty = 4.0$ as a function of δ for various values of E_2. Again negative values of E_2 case show higher L/D ratios than the positive E_2 case.

6.3 Free Stream Surfaces

The streamline equation $\vec{V} \times \vec{ds} = 0$ of the n = 2 case, can be written as

$$\frac{dr}{u_0+\varepsilon_2 u_2\cos\phi} = \frac{rd\theta}{v_0+\varepsilon_2 v_2\cos\phi} = \frac{r\sin\theta\, d\phi}{\varepsilon_2 w_2\sin\phi} \tag{6.29}$$

in the spherical polar coordinate system. To the lowest order, Eq. (6.29) becomes

$$\frac{dr}{r} = \frac{u_0}{v_0}\, d\theta \tag{6.30}$$

$$\frac{w_2}{v_0\sin\theta} = \frac{d\phi}{\varepsilon_2\sin_2\phi} \tag{6.31}$$

The solution of Eq. (6.30), which is the same solution as that of the n = 1 case, is

$$r_s = r\left(\frac{\theta^2-\delta^2}{\theta_s{}^2-\delta^2}\right)^{1/2} \tag{6.32}$$

and the solution of Eq. (6.31) is

$$\tan(\phi_s) = \tan(\phi)\exp\left[2\int_\theta^{\theta_s}\frac{\varepsilon_2 w_2}{\theta v_0}\, d\theta\right] \tag{6.33}$$

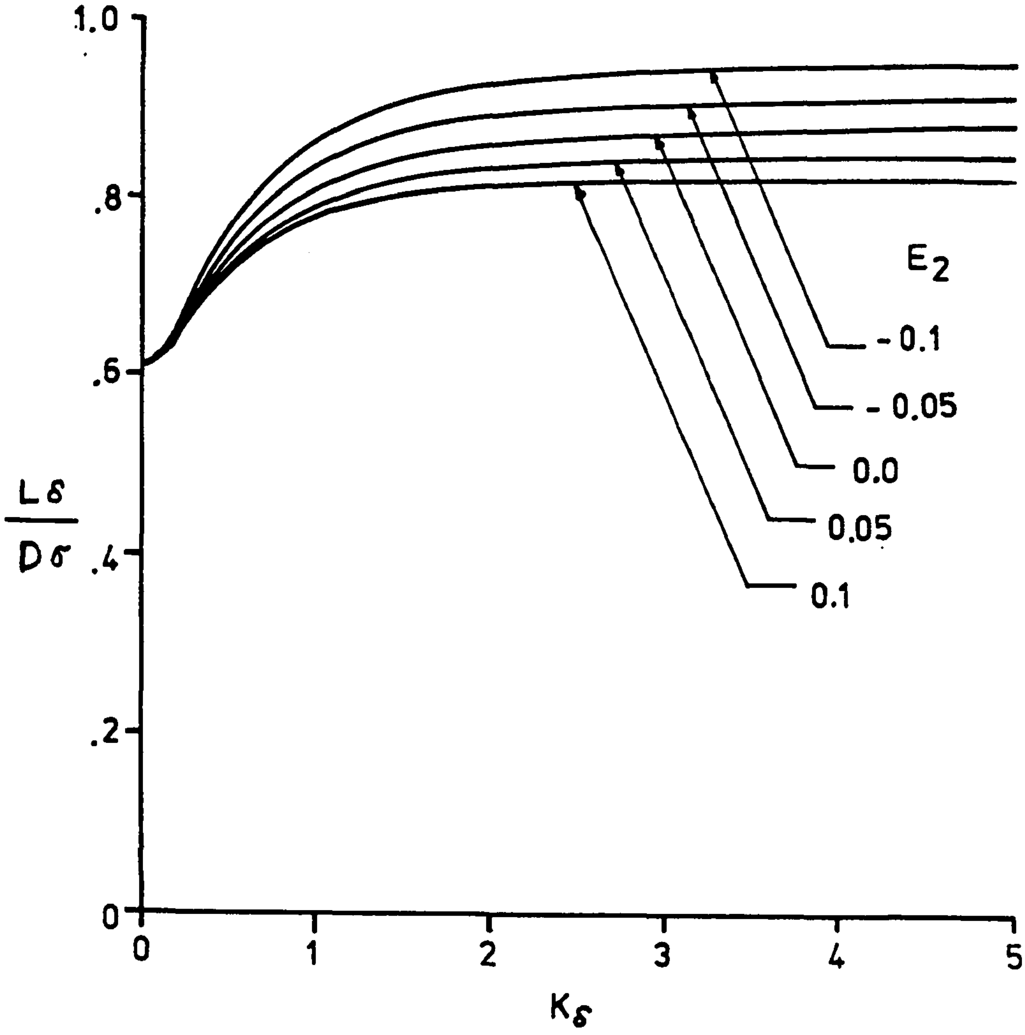

Fig. 6.7 Lift-to-Drag Ratio as a Function of K_δ for Fully-Optimized Waverider of n=2 Case.

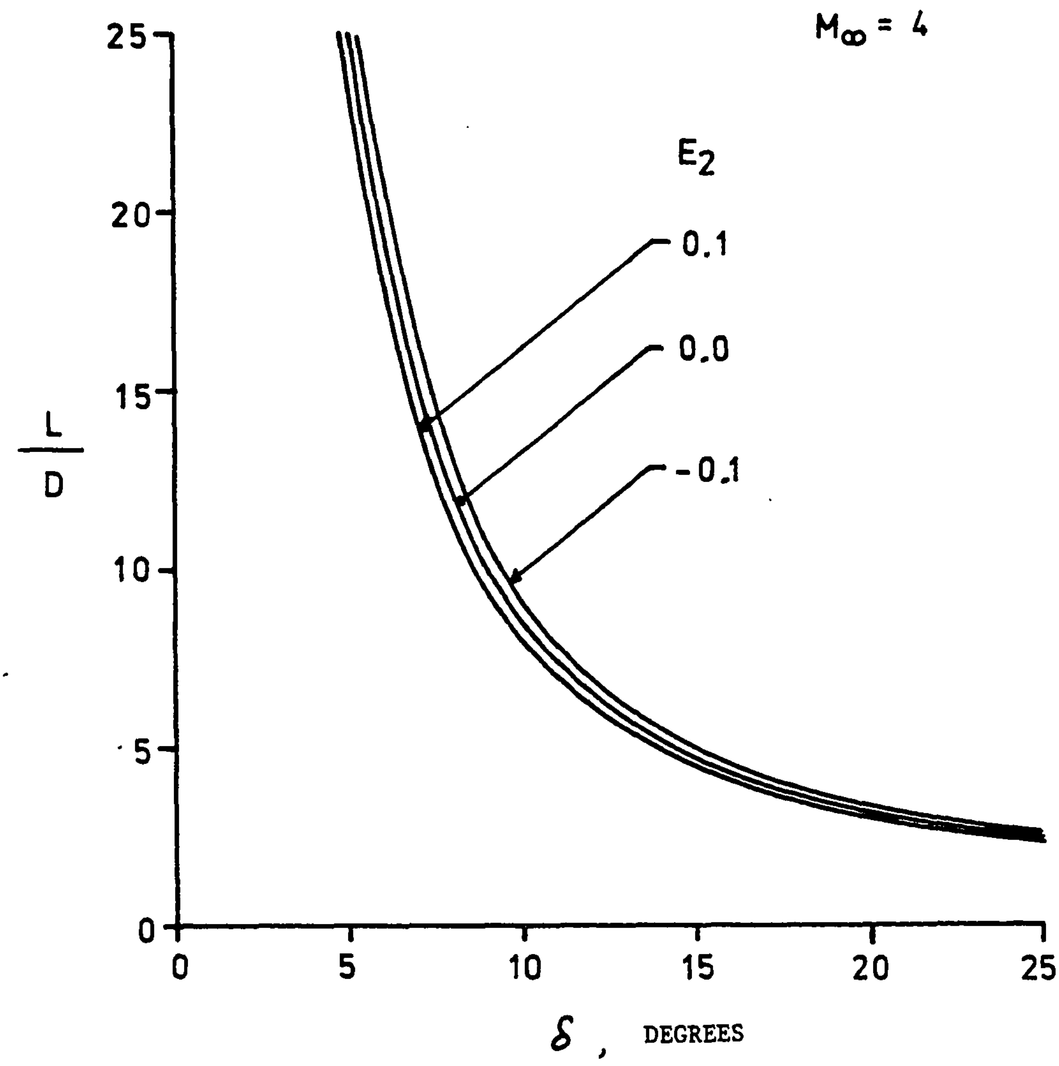

Fig. 6.8 Lift-to-Drag Ratio as a Function of Cone Angle for Fully-Optimized Waverider of n=2 Case.

where r_s, θ_s, ϕ_s are constants of integration.

The trailing edge of the compression stream surface which originates from the leading edge at (r_s, θ_s, ϕ_s) on the shock can be obtained by setting $\theta = \theta_b$ and $r = \ell$ in Eq. (6.32) and Eq. (6.33) and we get

$$r_s = \ell \left(\frac{\theta_b^2 - \delta^2}{\theta_s^2 - \delta^2}\right)^{1/2} \tag{6.34}$$

and

$$\tan(\phi_s) = \tan(\phi_b) \exp\left[2\int_{\theta_b}^{\theta_s} \frac{\varepsilon_2 w_2}{\theta v_0} d\theta\right] \tag{6.35}$$

where the point $(\ell, \theta_b, \theta_b)$ in the shock layer base plane is on the same streamline which passes through the point (r_s, θ_s, ϕ_s) at the shock.

The training edge of the free stream surface can be obtained by using Eq. (5.49) and Eq. (6.34) as

$$\theta_{fs} = \theta_s \left(\frac{\theta_b^2 - \delta^2}{\theta_s^2 - \delta^2}\right)^{1/2} \quad \text{and} \quad \phi = \phi_s \tag{6.36}$$

or

$$R_{fs} = \sigma \left(\frac{R^2(\phi_b) - 1}{\sigma^2 - 1}\right)^{1/2} \quad \text{and} \quad \phi = \phi_s \tag{6.37}$$

where the relation between ϕ_b and ϕ_s is given by

$$\tan(\phi_s) = \tan(\phi_b)\exp\left[2\int_{R(\phi_b)}^{\sigma} \frac{E_2 w_2}{\xi v_0} d\xi\right] \tag{6.38}$$

The trailing edges of both compression stream surface and free stream surface of the fully optimized waverider for given E_2 and K_δ are shown in Figs. 6.9, 6.10, and 6.11 for $K_\delta = 0.5$, 1.0, and 5.0. Two examples of semi-optimized waveriders are also shown in each figure. Similar to those waveriders of n = 1 case, n = 2 case waveriders also show that

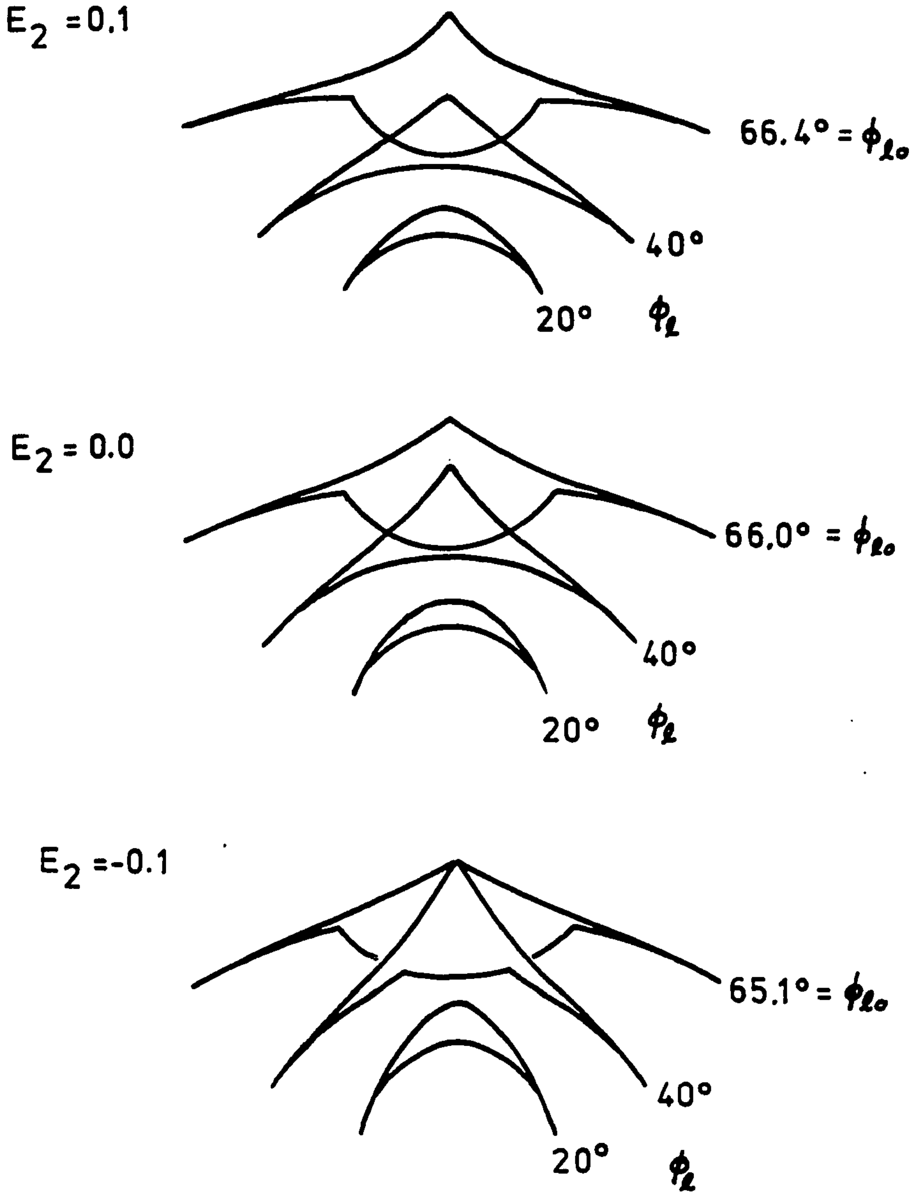

Fig. 6.9 Base Shapes of Fully-Optimized and Semi-Optimized Waveriders of n=2 Case (K_δ = 0.5).

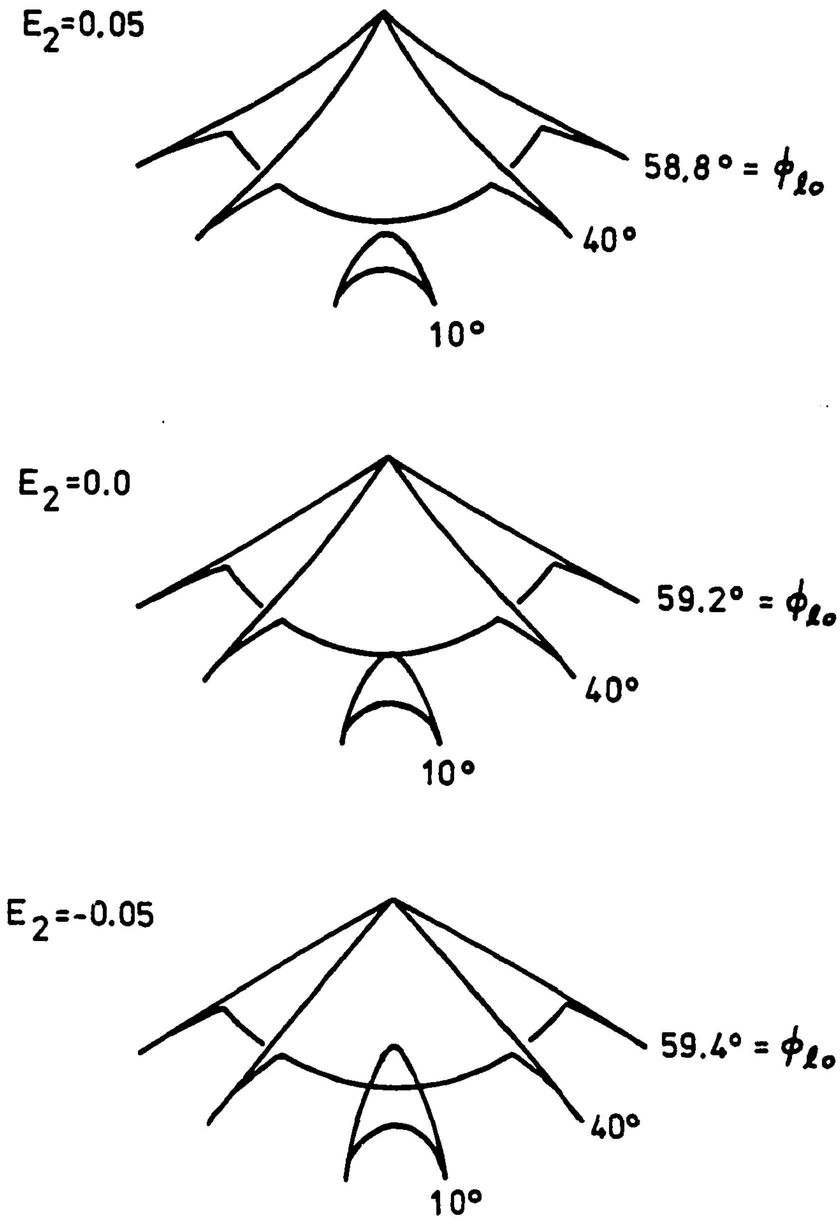

Fig. 6.10 Base Shapes of Fully-Optimized and Semi-Optimized Waveriders of n=2 Case (K_δ = 1.0).

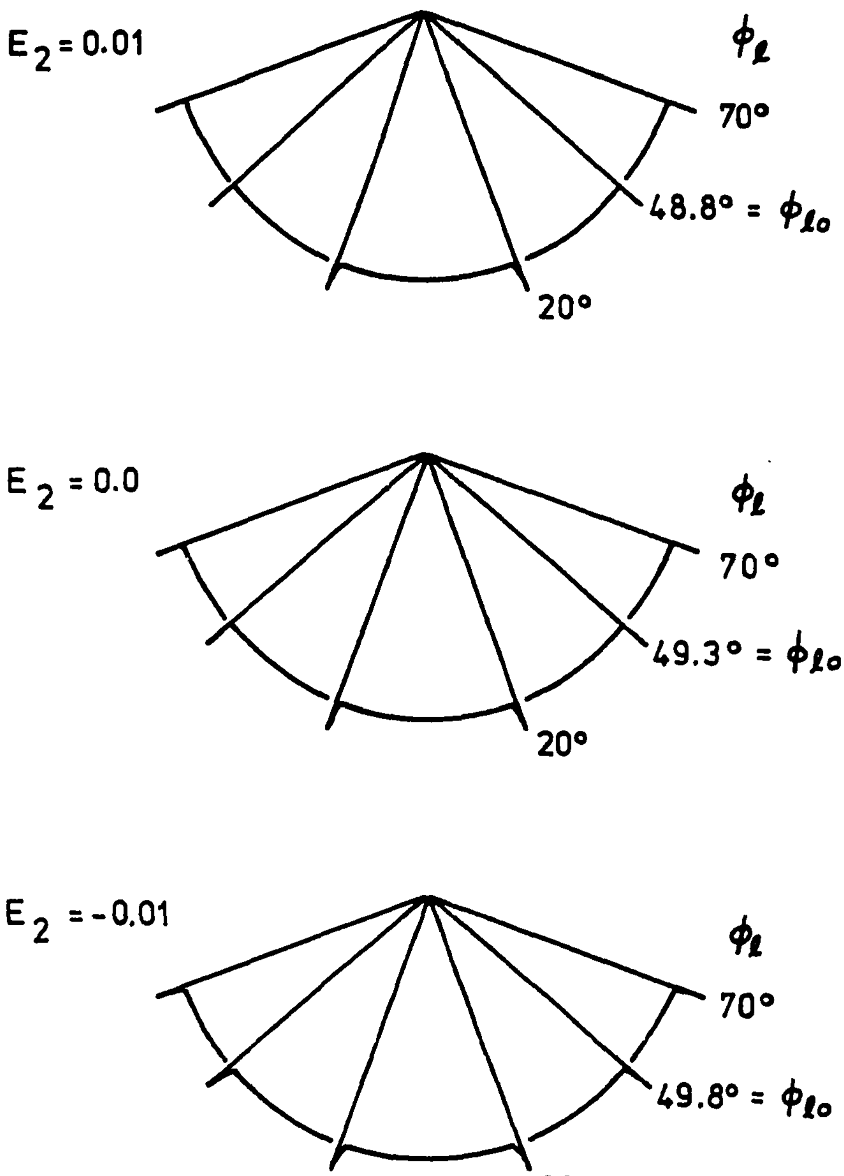

Fig. 6.11 Base Shapes of Fully-Optimized and Semi-Optimized Waveriders of n=2 Case (K_δ = 5.0).

the base plane is thinner when E_2 is positive than when E_2 is negative. However, there is very little difference between fully-optimized waveriders of different E_2 values when K_δ is very large.

SECTION VII

CONCLUDING REMARKS

The variational problem of maximizing lift-to-drag ratio of waveriders subject to general constraint condition is formulated and solved for fixed lift constraint case. Approximate analytic solutions for flow variables are used to calculate lift and drag. The results are valid for all values of K_δ.

For each case of E_n, there are two classes of waveriders, class A, a pointed-nose waverider with discrete winglet and a cone segment underbody, for small K_δ and class B, a rounded-nose sharp-lip waverider with a curved concave underbody.

When E_n is negative, waveriders of $n = 1$ and $n = 2$ cases give a higher lift-to-drag ratio than $E_n = 0$ case. Since the $E_n = 0$ case waverider is compared with other lifting bodies and it is shown that the $E_n = 0$ case waverider has higher lift-to-drag ratio, negative E_n case waveriders are the best producers of large lift-to-drag ratios. Those are waveriders generated from flows past a circular cone with negative angle of attack or generated from flows past an elliptic cone its horizontal axis is longer than its vertical axis.

However, we assumed the perturbation of the shock layer are to be much smaller than the circular cone shock layer and that there is maximum value of $|E_n|$. In this paper, the results are in the range of $|E_n| < 0.2\ (\sigma-1)$.

APPENDIX A

The first order solutions for flow variables of n = 1 case are given by

$$U_1 \equiv \frac{u_1}{V_\infty \delta} = F_1 \{-1 + \frac{\sigma}{4r} + \frac{3(r^2-1)^{1/2}}{4(\sigma^2-1)^{1/2}} + \frac{2r^2+1}{4r(\sigma^2-1)^{1/2}} \ln \left(\frac{\sigma+(\sigma^2-1)^{1/2}}{r + (r^2-1)^{1/2}}\right)\} + \frac{A_1}{r} + B_1 r$$

$$V_1 \equiv \frac{v_1}{V_\infty} = F_1\{- \frac{\sigma}{4r^2} + \frac{(r^2-1)^{1/2}}{4r(\sigma^2-1)^{1/2}} + \frac{2r^2-1}{4r^2(\sigma^2-1)^{1/2}} \ln \left(\frac{\sigma+(\sigma^2-1)^{1/2}}{r + (r^2-1)^{1/2}}\right)\} - \frac{A_1}{r^2} + B_1$$

$$W_1 \equiv \frac{w_1}{V_\infty} = - (F_1 H + U_1)/r$$

$$P_1 \equiv \frac{p_1}{\delta \rho_\infty V_\infty^2} = - \frac{\rho_0}{\rho_\infty} \{\left(\frac{u_0}{V_\infty}\right) U_1 + \left(\frac{v_0}{\delta V_\infty}\right) V_1 + F_1\}$$

where

$$r = \theta/\delta$$

$$A_1 = - \frac{g_1}{2}\left(1 + \frac{4\sigma^2}{\gamma+1}\right)$$

$$B_1 = - \frac{g_1}{2\sigma^2} \left(1- \frac{4\sigma^2}{\gamma+1}\right)$$

$$F_1 = \sigma g_1 (1-\xi_0)^2$$

$$\xi_0 = \frac{\rho_\infty}{\rho_0(\beta)}$$

$$H = 1 - \frac{(r^2-1)^{1/2}}{(\sigma^2-1)^{1/2}}$$

$$g_1 = 1 - \frac{3 + 2\sigma^2(3-4(\sigma^2+1)/(\gamma+1)) - \dfrac{\ln(\sigma+(\sigma^2-1)^{1/2})}{\sigma(\sigma^2-1)^{1/2}}}{5 - 2(\sigma^2+1)(1+4\sigma^2/(\gamma+1)) - \dfrac{\ln(\sigma+(\sigma^2-1)^{1/2})}{\sigma(\sigma^2-1)^{1/2}}}$$

The first order solutions for flow variables of $n = 2$ case are given by

$$U_2 \equiv \frac{u_2}{\delta V_\infty} = F_2 \{-1 + \frac{\sigma^2}{6r^2} + \frac{1}{3r^2} + (\frac{5}{6} - \frac{1}{3r^2}) \frac{(r^2-1)^{1/2}}{(\sigma^2-1)^{1/2}}$$

$$+ \frac{r^2}{2(\sigma^2-1)^{1/2}} (\cos^{-1}(1/\sigma) - \cos^{-1}(1/r))\} + \frac{A_2}{r^2} + B_2 r^2$$

$$V_2 \equiv \frac{v_2}{V_\infty} = F_2 \{-1 + \frac{\sigma^2}{3r^3} - \frac{2}{3r^3} + \frac{(r^2+2)(r^2-1)^{1/2}}{3r^3(\sigma^2-1)^{1/2}}$$

$$+ \frac{r}{(\sigma^2-1)^{1/2}} (\cos^{-1}(1/\sigma) - \cos^{-1}(1/r)) - \frac{2A_2}{r^3} + 2B_2 r$$

$$W_2 \equiv \frac{w_2}{V_\infty} = - 2(F_2 H + U_2)/r$$

$$P_1 \equiv \frac{p_2}{\delta \rho_\infty V_\infty^2} = - \frac{\rho_0}{\rho_\infty} \{(\frac{u_0}{V_\infty}) U_2 + (\frac{v_0}{\delta V_\infty}) V_2 + F_2\}$$

where

$$r = \theta/\delta$$

$$A_2 = - \frac{g_2 \sigma}{2} (1 + \frac{2\sigma^2}{\gamma+1})$$

$$B_2 = - \frac{g_2}{2\sigma^3} (1 - \frac{2\sigma^2}{\gamma+1})$$

$$F_2 = \sigma g_2 (1-\xi_0)^2$$

$$H = 1 - \frac{(r^2-1)^{1/2}}{(\sigma^2-1)^{1/2}}$$

$$\frac{1}{g_2} = \frac{1}{6\sigma^3} [\frac{3\cos^{-1}(1/\sigma)}{(\sigma^2-1)^{1/2}} + \frac{6}{\gamma+1} (\sigma^6+\sigma^2) + 3\sigma^4-\sigma^2-5]$$

REFERENCES

[1] Küchemann, D., The Aerodynamic Design of Aircraft, Pergamon Press, London, 1978, pp. 448-514.

[2] Nonweiler, T. R. F., "Delta Wings of Shape Amenable to Exact Shock-Wave Theory," Journal of Royal Aeronautical Society, Vol. 67, 1963, p. 39.

[3] Townend, L. H., "Research and Design for Lifting Reentry," Progress in Aerospace Sciences, Vol. 19, No. 1, 1979, pp. 1-80.

[4] Sims, J. L., "Tables for Supersonic Flow Around Right Circular Cones at Zero Angle of Attack," NASA SP-3004, 1964.

[5] Jones, J. G. and Woods, B. A., "The Design of Compression Surfaces for High Supersonic Speeds Using Conical Flow Fields," Aero. Res. Council R&M No. 3539, 1963.

[6] Maikapar, G. I., "Bodies Formed by the Stream Surfaces of Conical Flows," Fluid Dynamics, Vol. 1, No. 1, pp. 89-90, 1966.

[7] Baron, J. R., "Configuration Definition Based on Intersecting Shock Surfaces," Tech. Report 81-1, Dept. of Aeronautics and Astronautics, M.I.T., May, 1981.

[8] Doty, R. T. and Rasmussen, M. L., "Approximation for Hypersonic Flow Past an Inclined Cone," AIAA Journal, Vol. 11, No. 9, Sept. 1973, pp. 1310-1315.

[9] Rasmussen, M. L. and Lee, H. M., "Approximation for Hypersonic Flow Past a Slender Elliptic Cone," AIAA Paper 79-0364, AIAA 17th Aerospace Science Meeting, New Orleans, LA, January 1979.

[10] Jischke, M. C., "Supersonic Flow Past Conical Bodies with Nearly Circular Cross Sections," AIAA Journal, Vol. 19, No. 2, Feb. 1981, pp. 242-245.

[11] Rasmussen, M. L., "Waverider Configurations Derived from Inclined Circular and Elliptic Cones," J. of Spacecraft and Rockets, Vol. 17, No. 6, Nov.-Dec. 1980, pp. 537-545.

[12] Lusty, A. H. and Miele, A., "Bodies of Maximum Lift-to-Drag Ratio in Hypersonic Flow," AIAA Journal, Vol. 4, No. 12, Dec. 1966, pp. 2130-2135.

[13] Huang, H-Y., "Variational Approach to Conical Bodies Having Maximum Lift-to-Drag Ratio at Hypersonic Speeds," Journal of Optimization Theory and Applications, Vol. 2, No. 5, 1968, pp. 348-362.

[14] Van Dyke, M. D., "A Study of Hypersonic Small-Disturbance Theory," NACA 1194 (supersedes TN 3173), 1954.

[15] Cole, J. D. and Zien, T. F., "A Class of Three-Dimensional Optimum Hypersonic Wings," AIAA Journal, Vol. 7, No. 2, pp. 264-271, 1969.

[16] Kim, B. S., Rasmussen, M. L. and Jischke, M. C., "Optimization of Waverider Configurations Generated from Axisymmetric Conical Flows," AIAA Paper No. 82-1299, AIAA Atmospheric Flight Mechanics Conference, San Diego, CA, August 1982. (To appear in Journal of Spacecraft and Rockets.)

[17] Hildebrand, F. B., Methods of Applied Mathematics, Second Edition, Prentice-Hall, Inc., Englewood Cliffs, NJ, 1965, pp. 141-143.

[18] Rasmussen, M. L., Jischke, M. C. and Daniel, D. C., "Experimental Forces and Moments on Cone-Derived Waveriders for M = 3 to 5," J. of Spacecraft and Rockets, Vol. 19, No. 6, Nov.-Dec. 1982, pp. 592-598.

[19] Schindel, L. H., "Design of High Performance Hypersonic Missiles," AIAA Paper 82-0391, AIAA 20th Aerospace Sciences Meeting, Orlando, FL, Jan. 1982.

[20] Krieger, R. J., "Summary of Design and Performance Characteristics of Aerodynamic Configured Missiles," AIAA Paper 81-0286, AIAA 19th Aerospace Sciences Meeting, St. Louis, MO, Jan. 1981.

[21] Broadaway, R., "Aerodynamics of a Simple Cone-Derived Waverider," M.S. Thesis, Aerospace, Mechanical and Nuclear Engineering, University of Oklahoma, Norman, OK, May 1983.